5-2020

Structure and Hydrogen Dynamics of Alkaline Earth Metal Hydrides Investigated with Neutron Scattering

Eric Christopher Novak
University of Tennessee, enovak1@vols.utk.edu

Recommended Citation

Novak, Eric Christopher, "Structure and Hydrogen Dynamics of Alkaline Earth Metal Hydrides Investigated with Neutron Scattering. " PhD diss., University of Tennessee, 2020.
https://trace.tennessee.edu/utk_graddiss/5842

To the Graduate Council:

I am submitting herewith a dissertation written by Eric Christopher Novak entitled "Structure and Hydrogen Dynamics of Alkaline Earth Metal Hydrides Investigated with Neutron Scattering." I have examined the final electronic copy of this dissertation for form and content and recommend that it be accepted in partial fulfillment of the requirements for the degree of Doctor of Philosophy, with a major in Materials Science and Engineering.

Takeshi Egami, Major Professor

We have read this dissertation and recommend its acceptance:

Niina Jalarvo, David Keffer, Katharine Page

Accepted for the Council:

Dixie L. Thompson

Vice Provost and Dean of the Graduate School

(Original signatures are on file with official student records.)

Structure and Hydrogen Dynamics of Alkaline Earth Metal Hydrides Investigated with Neutron Scattering

A Dissertation Presented for the
Doctor of Philosophy
Degree
The University of Tennessee, Knoxville

Eric Christopher Novak
May 2020

ACKNOWLEDGEMENTS

The amount of people that have been involved in this investigation is truly impressive and it is just not possible to acknowledge everyone here. I thank you all for your support, as this would not be possible without your help. First and foremost, I would like to thank my family: my parents Chris and Candy, my sisters Justine and Mel, and my dog Nova. The love and support from my family and friends has motivated me to keep pushing the limits of my education to unimaginable levels. I would also like to thank my research advisors, Dr. Niina Jalarvo and Dr. Takeshi Egami, for their excellent guidance and assistance with my research. I worked in two different research groups during my time here. I thank my first research advisor, Dr. Michael Ohl, for his initial guidance and for accepting me to this research position. In addition, I am thankful to Niina for giving me the opportunity to join her group and for making the transition between groups smooth. I would also like to acknowledge the rest of my Ph.D. committee members, Dr. David Keffer and Dr. Katharine Page, for their guidance, insights, and intriguing scientific discussions. This research simply would not have been possible without the countless contributions of Dr. Luke Daemen. Thank you for spending so much of your time teaching me everything from sample synthesis, design and fabrication of sample environments, experimental techniques, and data analysis methods. To the University of Tennessee, Forschungszentrum Jülich, and Oak Ridge National Laboratory, I owe much gratitude to these facilities for accepting me into the Materials Science and Engineering Ph.D. program, for the graduate research assistantship position, and for the research funding. This research was conducted at three different neutron scattering facilities (SNS, NCNR, MLZ) and on six different instruments (SNAP, VISION, NOMAD, BASIS, HFBS, and SPHERES). I would like to thank all the instrument teams and support staff at these facilities for enabling me to conduct successful experiments. Specifically from these facilities, I would like to acknowledge Timmy Ramirez-Cuesta, Y.Q. Cheng, Michelle Everett, Jörg Neuefeind, Bianca Haberl, Jamie Molaison, Bekki Mills, Robert

Marrs, Matt Rucker, Mark Loguillo, Robert Smith, Peter Metz, and Tim Prisk. Lastly, I would like to acknowledge all the faculty that have taught me over the years at the University of Tennessee, Shippensburg University, Pennsylvania State University, University of Arkansas, and Southern Lehigh School District.

ABSTRACT

Metal hydrides are of interest for solid-state hydrogen storage and energy applications. Binary alkaline earth hydrides present prototypical systems for understanding the relationship between structure and hydrogen dynamics. Hydrogen transport is a key property that directly relates to the efficiency of devices. We have chosen three different alkaline earth metal hydrides with vastly different hydrogen kinetics: BaH_2 [barium hydride], CaH_2 [calcium hydride], and MgH_2 [magnesium hydride]. Hydrogen transport in MgH_2 is notoriously poor while BaH_2 exhibits fast hydride ion conduction. We employ neutron scattering techniques to understand the role that the crystal structure plays in influencing the hydrogen dynamics in these materials. A structural phase transition (orthorhombic to hexagonal) was observed in BaH_2 occurring around T = 775 K. Quasielastic neutron scattering measurements showed that the hydrogen diffusion coefficients increase by an order of magnitude following the phase transition. Hydrogen jumps among the shortest hydrogen-hydrogen distances were found to be restricted in the orthorhombic phase but become the preferred jumps in the hexagonal phase. Total neutron scattering measurements show evidence of dynamic structural fluctuations and a splitting of the deuterium sites in the hexagonal phase. High pressure (1.3 GPa) induces the same phase transition and increases the hydrogen dynamics. The orthorhombic structure of CaH_2 is isomorphic to BaH_2, but the transition to the hexagonal structure is absent. Instead, evidence of a second-order phase transition was found, which influences the hydrogen dynamics. Inelastic neutron scattering indicates that the ionic bonds in CaH_2 are stronger than in BaH_2, which hampers diffusion. The behavior of MgH_2 is different due to the stronger, covalent-like bonds. Hydrogen diffusion was not observed preceding the sudden thermal decomposition around 600 K as the hydrogen remains tightly bound. This study served to elucidate the role that a structural phase transition plays in transforming a solid-state material with modest hydrogen kinetics into a fast-ionic conductor. Even small modifications of the structure influence the hydrogen

dynamics. The knowledge gained here sheds light on the intricate relationship between the structure and hydrogen diffusion, which can be applied to understand and advance the transport properties in other metal hydride systems.

TABLE OF CONTENTS

LIST OF TABLES

LIST OF FIGURES

1 INTRODUCTION

1.1 Background and Motivation

With the growing concerns of the negative environmental impact of greenhouse gas emissions on our climate, it is becoming increasingly important to reduce the dependence on fossil fuels by transitioning to cleaner renewable energy sources. Despite recent progress, 79% of our energy needs are still being fulfilled by fossil fuels in 2018.[1] A promising clean energy source to harness is hydrogen. Hydrogen has more than 3 times the amount of chemical energy per mass than fossil fuels.[2] When combusted with dilute mixtures of air, it is a clean burning fuel that generates water as the only byproduct. Currently, a true hydrogen economy has yet to come to fruition because the infrastructure is lacking due to technical barriers involving the production and storage of hydrogen. Before hydrogen can emerge to provide energy on a large scale, there are key issues that need to be solved. This research investigates the structure and hydrogen dynamics of alkaline earth metal hydride systems, which are potential candidates for use as solid-state electrolytes and hydrogen storage materials.

Conventional methods for hydrogen storage are in the liquid and gas state. For many applications, and especially in the case of onboard mobile storage, there are strict volumetric requirements that the storage device must adhere to. For example, high pressure gas storage tanks would need an internal volume of about 60 gallons for 4 kg of hydrogen storage at 200 bar.[2] The relative volumes needed to store 4 kg of hydrogen in comparison to the size of a car is displayed in Figure 1. Higher volumetric storage densities can be achieved using liquid storage, but hydrogen condenses at a temperature of 20 K at 1 bar of pressure, requiring a significant amount of energy. Clearly, the volumetric capacities needed for gaseous and liquid hydrogen storage presents a significant problem, especially considering the U.S. Department of Energy (DOE) goal of onboard storage of 5 –

13 kg H_2.[3] In order to compete with electric and hydrocarbon powered vehicles, this is the amount of hydrogen needed to achieve ranges greater than 300 miles. Recently, high-pressure gas storage tanks have been greatly improved with carbon fiber reinforcements, allowing for higher pressures of 700 bar to be routinely achieved. This type of storage system is currently used in hydrogen fuel cell vehicles, such as the Toyota Mirai.[4] However, higher pressure fuel tanks present increased safety concerns. Beyond fuel cell vehicles, other mobile applications with less stringent volumetric/gravimetric restraints, such as cargo ships and ferries, can benefit from hydrogen power.[5] In the field of hydrogen storage, improving high pressure gas storage tanks is viewed as the short-term solution to meet the U.S. DOE goals, while the long-term solution likely lies in materials-based hydrogen storage technologies.

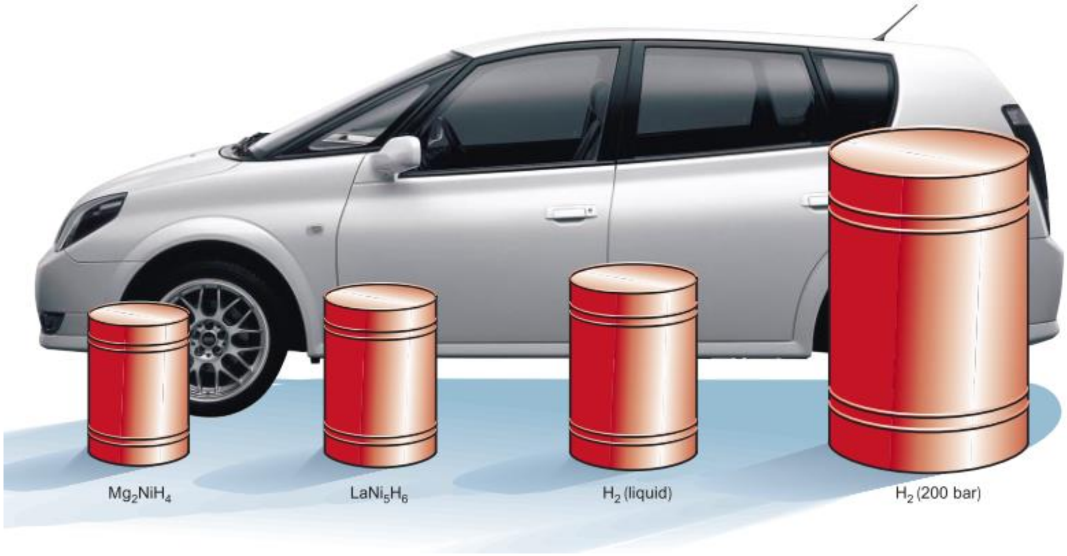

Figure 1: Volume requirements for 4 kg of hydrogen stored by different methods relative to the size of a car. Reprinted with permission from Schlapbach and Zuttel.[2]

The alternative to gas and liquid storage methods is solid-state storage. Many metals and alloys can store large quantities of hydrogen, which are collectively known as metal hydrides. Solid-state hydrogen storage is promising because many of the metal hydrides have high volumetric and gravimetric storage densities. This allows large amounts of hydrogen to be stored at low pressures in a compact manner. For example, Figure 1 shows the volumetric reduction achieved using the metal hydride Mg_2NiH_4 when compared to both the liquid and gas storage methods.[2] This compound was chosen as the storage medium for a hydrogen-powered bus built by Daimler-Benz, along with an additional two tanks containing iron-titanium hydride.[6] A significant amount of research has been conducted in the decades following this early prototype, which is summarized in the comprehensive review on the use of metal hydrides for fuel cell applications reported by Lototskyy et al.[7] Based on the storage densities alone, metal hydrides may seem like the ideal storage material, but major drawbacks have so far prevented their widespread use. For most applications, the metal hydride should possess excellent dehydrogenation/rehydrogenation kinetics, large volumetric and gravimetric storage densities, fast refueling rates, resistance to degradation during thermal cycling, and a reasonably low decomposition temperature, amongst other criteria. The ability to transport hydrogen quickly and efficiently through the material is a crucial factor that directly influences the ease of hydrogen storage and retrieval in functional devices. While hydrides consisting of light-weight metals (Li, Na, Mg, etc.) have high storage densities, the hydrogen is often stored irreversibly and/or with poor kinetics. On the other hand, the heavier elements have the immediate drawback of low gravimetric storage densities and tend to have high decomposition temperatures, but they can offer excellent kinetics and reversibility. Immense efforts have been devoted to tailoring metal hydrides for onboard applications, with most of this research focused on lowering the decomposition temperatures, increasing the storage densities, and improving the kinetics. Common techniques to alter these properties are nanostructuring (ball milling), catalyst addition, aliovalent doping, and/or alloying the material.[8, 9] In practice, a combination of these techniques is typically used. While combining multiple methods often leads to the most significant improvement in the properties, it can be difficult to separate the underlying mechanism causing the improvement. Despite these efforts, the ideal metal hydride system that satisfies all the DOE goals has remained elusive. In addition to the mobile applications, metal hydrides may prove useful for high temperature, stationary applications where high thermal stability is desired, such as neutron moderators in nuclear reactors,[10, 11] tritium sequestration systems (getterers) in next generation nuclear plants,[11] or chemical heat storage materials for solar applications.[12] Better yet, some of the metal hydrides have been found to exhibit fast ionic conduction of hydride ions, making them intriguing candidates for solid-state electrolytes in a wide range of energy-related applications.[13]

Our research is focused on the metal hydrides from the alkaline earth metal group. This group forms binary hydrides with the general formula AeH_2 with Ae = Be, Mg, Ca, Sr, Ba, and Ra. These compounds are known as saline hydrides because of the ionic nature of the bonding, except for Mg and Be. The chemical bonding in BeH_2 is covalent while MgH_2 bridges the gap between covalent and ionic, which is why it is sometimes referred to as an intermediate hydride. Our investigation will focus on three of the alkaline earth hydrides: MgH_2, BaH_2, and CaH_2. MgH_2 has been studied extensively for mobile applications due to the high hydrogen storage density (7.6 wt%) and the intermediate decomposition temperature, $T_{dec} \approx 600$ K.[14, 15] Additionally, the high abundance of Mg in the Earth's crust makes this a very appealing element for manufacturing. Unfortunately, poor hydrogen kinetics and reversibility has largely hampered the potential use for this material in mobile applications. BaH_2 and CaH_2 both have high decomposition temperatures ($T_{dec} \approx 940$ K) and modest storage densities (1.44 wt% for BaH_2, 4.75 wt% for CaH_2), which resulted in these materials being largely ignored by the scientific community so far.[15] Nonetheless, BaH_2 is an intriguing material because it exhibits fast ionic conduction of hydride ions at elevated temperatures (0.2 $S\cdot cm^{-1}$ at $T = 903$ K), which is faster than the typical oxide and proton conductors in use today.[13] In addition, the crystal structure of CaH_2 (and SrH_2) is isomorphic with that of BaH_2, but these materials experience slower hydrogen dynamics. Therefore, information gained about one of these materials can be largely applied to understand the other compounds. In summary, MgH_2 is a light-weight metal hydride with slow hydrogen kinetics, CaH_2 is middle-weight with intermediate hydrogen kinetics, and BaH_2 is heavy-weight with fast hydrogen kinetics. This study seeks to understand what causes such drastic differences in the hydrogen transport properties in these materials. Most kinetics studies have focused on measuring the macroscopic dehydrogenation and rehydrogenation rates due to its direct relation to refueling times and the ease of hydrogen retrieval for device operations. To our knowledge, no experimental investigations have been devoted to determining the microscopic nature of the diffusion mechanism in any of these three materials. A few studies have reported the ionic conductivity extracted from electrochemical impedance spectroscopy (EIS) measurements.[13, 16, 17] However, this technique yields bulk diffusion rates and does not provide information about the microscopic nature of the diffusion process, such as diffusion pathways and hydrogen jump lengths. In addition, there have been some computational investigations focused on the hydrogen dynamics.[16, 18]

In addition to the binary hydrides, we planned to study two different ternary hydrides: dibarium magnesium hexahydride (Ba_2MgH_6) and tetracalcium trimagnesium tetradecahydride ($Ca_4Mg_3H_{14}$). However, difficulties in the sample synthesis process prevented a proper investigation of these two materials. As mentioned previously, alloying a material is a common technique to alter and improve the properties of materials. Currently, investigations of Ba_2MgH_6 and $Ca_4Mg_3H_{14}$ have only been focused on sample synthesis methods and structural characterization.[19, 20] Therefore, the hydrogen transport properties are unknown. Alloying a HAEH with the lighter weight Mg atoms could be a unique method to increase the storage densities while maintaining adequate hydrogen transport properties.

We will use neutron scattering to understand the nature of the hydrogen diffusion mechanism in alkaline earth hydrides and how the bonding and structure influences this process. Fast ionic conduction of hydride ions has immense commercial appeal and fundamental knowledge of this process can lead to a better understanding of how to improve the transport of hydrogen in other metal hydride systems.

1.2 Overview of Investigation

Neutron scattering is the main technique used in this investigation to study these metal hydride systems. Many experimental techniques have difficulty measuring signals from hydrogen. However, the large incoherent neutron scattering cross section of hydrogen allows neutron scattering to successfully probe hydrogen, making it the ideal technique for our investigation. In Chapter 2, a general introduction to the theory of neutron scattering will be presented. In Chapter 3, an overview of the experimental methods and sample environments will be discussed. This includes incoherent quasielastic neutron scattering (QENS), powder inelastic neutron scattering (INS), neutron powder diffraction (NPD) and total neutron scattering. QENS measures the diffusion of hydrogen through the crystal structure, giving insight into the diffusion mechanism and energy landscape. INS, also known as neutron vibrational spectroscopy, measures the vibrational density of states. This provides information about chemical bonding, local atomic structure, and the hydrogen release mechanism. NPD and total neutron scattering are employed to characterize the local vs. global crystal structure and to examine its role in processes such as hydrogen release and diffusion. To safely measure pyrophoric samples at high temperatures, custom sample environments were designed and fabricated. In addition to high temperature experiments, the effect of pressure on the material properties was also explored. Details of the various sample environments will be presented in detail. Additional experimental details will be given in the Appendix. Chapter 4 will cover the data analysis methods used in the investigation. This includes everything from data reduction and analysis, calculations, and methods for pressure determinations. Next, Chapter 5 will give a thorough account of the synthesis methods used to produce the protonated and deuterated metal hydride samples. Most of the metal hydrides studied in this investigation are not commercially available. Lastly, a complete summary and detailed analysis of the results for BaH_2, CaH_2, and MgH_2 will be presented and discussed in Chapters 6 – 8 followed by a conclusion and future outlook discussion in Chapter 9. The main focus of this research was to obtain a complete description about the structure and dynamics of BaH_2 due to its unique behavior and interesting hydrogen transport properties. Second to this, the hydrides of CaH_2 and MgH_2 were investigated with the same techniques for comparison to BaH_2.

2 THEORY OF NEUTRON SCATTERING

A rigorous derivation of neutron scattering theory is beyond the scope of this chapter and can be found elsewhere.[21, 22] The focus here is to highlight and introduce the main features of neutron scattering theory that are needed to understand the results in this investigation.

2.1 Momentum and Energy Transfer

Consider the case of a monochromatic neutron beam of wavelength λ incident on a single atom whose position is fixed in space. The incident neutron is unable to transfer energy to the atom, resulting in an elastic scattering event. Later, this constraint will be removed, and a finite amount of energy will be transferred to the sample, known as inelastic scattering. During the elastic scattering process, the incident and final wavevectors, k and k', remain unchanged:

$$k = k' = \frac{2\pi}{\lambda} \tag{2.1}$$

We can then define the difference in wavevectors as the scattering vector Q.

$$Q = k' - k \tag{2.2}$$

As displayed in Figure 2, the scattering angle dependence of the scattering vector is given by:

$$Q = \sqrt{k^2 + k'^2 - 2kk'\cos(2\theta)} = \frac{4\pi}{\lambda}\sin(\theta) \tag{2.3}$$

The momentum transfer, $\hbar Q$, along with the energy transfer, $\hbar\omega$, are two concepts that are central to neutron scattering theory. The energy transfer and momentum transfer are related through:

$$\hbar\omega = E = \frac{\hbar^2 Q^2}{2m} \tag{2.4}$$

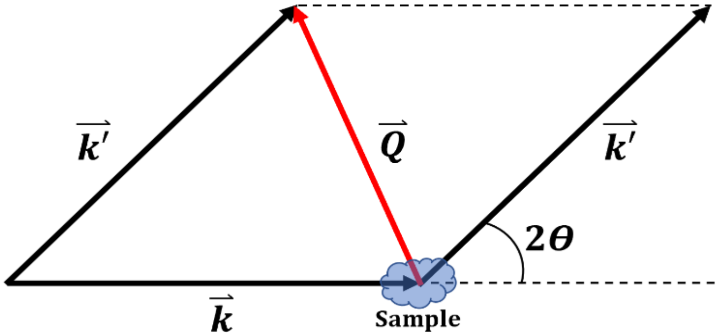

Figure 2: Wave vector and scattering vector relationship in reciprocal space.

2.2 Neutron Scattering Cross Sections

The geometry of a typical scattering experiment is displayed in Figure 3. The incident beam with wave vector k is scattered by the sample and is measured by a detector with a final wave vector of k'. The quantity that is measured in a neutron scattering experiment is the fraction of neutrons with incident energy E scattered into a solid angle $d\Omega$ in the direction of 2θ and ϕ (as seen by the detector) with a final energy between E' and $E' + dE'$.[21, 22] The partial differential cross section is thus given by:

$$\frac{d^2\sigma}{d\Omega dE'} = \frac{n' d^2\sigma}{j d\Omega dE'} \tag{2.5}$$

where n' is the number of neutrons scattered into the detector, j is the incident neutron flux, and σ is the total cross section. For the case of elastic scattering (or if energy transfer is not determined during the measurement), we can use the following notation:[21]

$$\langle k' | \hat{V} | k \rangle = \left(\frac{m}{2\pi\hbar^2}\right) \int e^{-ik'\cdot r} \hat{V} e^{-ik\cdot r} dr \tag{2.6}$$

to express the differential cross section as:

$$\frac{d\sigma}{d\Omega} = |f(Q)|^2 = \left| \langle k' | \hat{V} | k \rangle \right|^2 \tag{2.7}$$

where $f(Q)$ is the scattering amplitude, and $\hat{V}$ is the interaction potential between the incident neutron and the sample. The differential cross section is the quantity that is measured during an experiment that counts all the neutrons scattered into the solid angle *dΩ, i.e.* no energy determination*.*

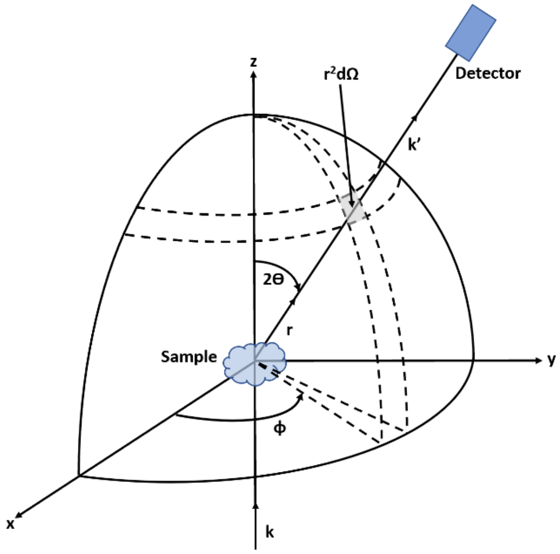

Figure 3: Geometry of a neutron scattering experiment.

Now we can expand this to the case of inelastic scattering where both the initial and final neutron energies are determined. This type of measurement yields information known as the partial differential cross section, which is sometimes referred to as the double differential cross section. The initial state of the sample is described by an eigenvector, $|\lambda\rangle$. Upon interaction with the sample, the incident neutron energy changes by $\hbar\omega$ through the rearrangement of the target states. During the transition from initial state λ to final state λ′, the target energy changes by the amount:

$$\hbar\omega = E_{\lambda'} - E_{\lambda} \tag{2.8}$$

The differential cross section can then be expressed as:

$$\frac{d\sigma}{d\Omega} = \frac{k'}{k}\left|\langle k'\lambda'|\hat{V}|k\lambda\rangle\right|^{2} \tag{2.9}$$

Including energy conservation through the use of a delta function, the partial differential cross section can be written as:

$$\frac{d^2\sigma}{d\Omega dE'} = \frac{k'}{k}\overline{\sum_{\lambda\lambda'} p_\lambda \left|\langle k'\lambda'|\hat{V}|k\lambda\rangle\right|^2 \delta(\hbar\omega + E_\lambda - E_{\lambda'})} \tag{2.10}$$

where p_λ is a weighting parameter used to normalize the range of accessible states. In practice, instrumental effects cause the delta function to broaden. Therefore, the resolution of the instrument needs to be measured and accounted for carefully during the data reduction and analysis of neutron scattering data.

2.3 Scattering Lengths

Again, assume the case of a neutron interacting with a single, bound nucleus. Due to the nature of the neutron-nucleon interaction, the scattering is isotropic and can be described by a single parameter, *b*, known as the scattering length. The scattering length is a complex parameter, with real values representing the neutron-nucleon scattering and imaginary values for absorption. A suitable form of $\hat{V}(r)$ can be achieved using Fermi's golden rule, which also satisfies the Born approximation since both are based on first-order perturbation theories.[22] The resulting Fermi pseudopotential takes the form of a delta function:

$$\hat{V}(r) = \frac{2\pi\hbar^2}{m} b\delta(r - R) \tag{2.11}$$

and is used to describe the interaction potential for an incident neutron scattering from a nucleus at position *R*.[23] Substituting Eq. (2.11) into Eq. (2.6) and setting *R* = 0 gives the expression:

$$\langle k'|\hat{V}|k\rangle = b \tag{2.12}$$

Therefore, Eq. (2.7) takes the form:

$$\frac{d\sigma}{d\Omega} = |b|^2 \tag{2.13}$$

The total cross section is then:

$$\sigma = 4\pi|b|^2 \tag{2.14}$$

Cross sections are conventionally reported in the units of barns, where 1 barn = 10^{-24} cm^2. One can observe that the cross section has a unit of area. Therefore, the cross section can be viewed as an impenetrable sphere that presents a cross sectional area with radius *b* to the incoming neutron. A larger positive scattering length provides a larger target for the neutron to interact with, hence increasing the probability of a scattering event occurring. An atom with a large cross section will scatter neutrons more efficiently than an atom with a smaller cross section.

Expanding this from the case of a single nucleus to a rigid array of *N* nuclei, we can investigate interference effects that arise from the scattering process. Defining the scattering length of the j^{th} nucleus as b_j, Eq. (2.11) can be written as:

$$\hat{V}(r) = \frac{2\pi\hbar^2}{m}\sum_j b_j\,\delta\left(r - R_j\right) \tag{2.15}$$

From this, it can be shown that the differential cross section takes the form:

$$\frac{d\sigma}{d\Omega} = \sum_{jj'} e^{iQ\cdot\left(R_j - R_{j'}\right)}\overline{b_{j'}^{*}b_j} \tag{2.16}$$

The relationship between the scattering lengths is:

$$\overline{b_{j'}^{*}b_j} = \left|\bar{b}\right|^2 \quad if \quad j \neq j' \tag{2.17a}$$

$$\overline{b_{j'}^{*}b_j} = \overline{|b|^2} \quad if \quad j = j' \tag{2.17b}$$

Combining Eq. (2.17a) and Eq. (2.17b) gives:

$$\overline{b_{j'}^{*}b_j} = \left|\bar{b}\right|^2 + \delta_{jj'}\left(\overline{|b|^2} - \left|\bar{b}\right|^2\right) \tag{2.18}$$

Substitution of (2.18) into Eq. (2.16) yields the final expression:

$$\frac{d\sigma}{d\Omega} = \left(\frac{d\sigma}{d\Omega}\right)_{coh} + \left(\frac{d\sigma}{d\Omega}\right)_{inc} \tag{2.19}$$

The coherent cross section is then:

$$\left(\frac{d\sigma}{d\Omega}\right)_{coh} = \left|\bar{b}\right|^2\left|\sum_j e^{iQ\cdot R_j}\right|^2 \tag{2.20}$$

and the incoherent cross section:

$$\left(\frac{d\sigma}{d\Omega}\right)_{inc} = N\overline{\left|b-\bar{b}\right|^2} \tag{2.21}$$

From this, a simple relationship between the total, incoherent, and coherent cross sections is observed:

$$\sigma_{total} = \sigma_{coh} + \sigma_{inc} \tag{2.22}$$

Coherent scattering involves strong interference of the scattered wave as the particle interacts with multiple nuclei in the sample. As will be discussed in Section 2.5, coherent scattering only occurs in a crystal when strict geometrical requirements are satisfied, i.e. Q corresponds to a reciprocal lattice vector. Hence, coherent scattering yields information about the structural arrangement of atoms in the crystal. While the coherent cross section (Eq. (2.20)) contains a phase factor describing the interference, the incoherent cross section (Eq. (2.21)) contains no such phase relationship. Therefore, incoherent scattering contains information about single particle dynamics. In other words, it measures a correlation between the position of a particle *R(0)* at *t = 0* compared to the position of the particle at a later time *R(t)*. Incoherent scattering provides information about both the temporal and spatial (geometrical) motion of the atoms in the sample.

The cross section can be different for isotopes of the same element. The scattering lengths and cross sections of the two most abundant isotopes of hydrogen (protium and deuterium) are listed in Table 1.[23] It can be observed that protium scatters primarily incoherently with a very large cross section of σ_{inc} = 80.27(6). Due to this feature, neutron spectroscopy (or more specifically quasielastic neutron scattering) is an extremely powerful technique to probe the diffusive motion of hydrogen. On the other hand, σ_{coh} for deuterium is almost three times bigger than σ_{inc}, meaning deuterium primarily scatters coherently. Therefore, protonated samples are used for hydrogen dynamics investigations while deuterated samples are used for structural measurements. In addition, both σ_{coh} and σ_{inc} are notably larger for hydrogen when compared to the cross sections of Mg, Ca, and Ba (the only other elements studied in this investigation). Therefore, the signal measured using neutron scattering on the metal hydride samples studied here is strongly weighted to show only the contributions from hydrogen. This means that the contributions from the metal atoms can largely be ignored. Note, this statement mostly applies to the spectroscopy techniques, as the diffraction methods still use the scattered signal from the metal atoms to determine their respective positions.

Table 1**:** Scattering lengths and cross sections for two of the isotopes of hydrogen (protium and deuterium) and an isotopic average for Mg, Ca, and Ba.[23] The units for scattering lengths and cross sections are fm and barns, respectively.

Element	Isotope	b_{coh}	b_{inc}	σ_{total}	σ_{coh}	σ_{inc}	σ_{abs}
H	H^1 (protium)	-3.7406(11)	25.274(9)	82.03(6)	1.7583(10)	80.27(6)	0.3326(7)
	H^2 (deuterium)	6.671(4)	4.04(3)	7.64(3)	5.592(7)	2.05(3)	0.000519(7)
Mg		5.375(4)		3.71(4)	3.631(5)	0.08(6)	0.063(3)
Ca		4.70(2)		2.83(2)	2.78(2)	0.05(3)	0.43(2)
Ba		5.07(3)		3.38(10)	3.23(4)	0.15(11)	1.1(1)

2.4 Correlation and Response Functions

From the previous section, the differential cross takes the form:[22, 24]

$$\frac{d^2\sigma}{d\Omega dE'} = \frac{k'}{k}\frac{1}{2\pi\hbar}\left[\left|\bar{b}\right|^2 \sum_{jj'} \int_{-\infty}^{\infty} e^{-i\omega t} dt\, \overline{e^{-\iota Q R_j(0)} e^{-\iota Q R_{j'}(t)}} + \overline{\left|b-\bar{b}\right|^2} \int_{-\infty}^{\infty} e^{-i\omega t} dt \sum_{j} \overline{e^{-\iota Q R_j(0)} e^{-\iota Q R_j(t)}}\right] \tag{2.23}$$

We can simplify the expression by defining the (coherent) intermediate scattering function *I(Q,t)* and (incoherent) self-intermediate scattering function $I_s(Q,t)$.

$$\frac{d^2\sigma}{d\Omega dE'} = \frac{k'}{k}\frac{1}{2\pi\hbar}\left[\left|\bar{b}\right|^2 \int_{-\infty}^{\infty} I(Q,t)e^{-i\omega t}dt + \overline{\left|b-\bar{b}\right|^2} \int_{-\infty}^{\infty} I_s(Q,t)e^{-i\omega t}dt\right] \tag{2.24}$$

The intermediate scattering functions are often referred to as correlation functions. We can then define the coherent scattering function *S(Q,ω)* and the incoherent scattering function S_i(Q,ω):

$$S(Q,\omega) = \frac{1}{2\pi\hbar}\int_{-\infty}^{\infty} I(Q,t)e^{-i\omega t}dt \tag{2.25a}$$

$$S_i(Q,\omega) = \frac{1}{2\pi\hbar}\int_{-\infty}^{\infty} I_s(Q,t)e^{-i\omega t}dt \tag{2.25b}$$

The scattering functions are known as response functions. *S(Q,ω)* is simply just a Fourier transform *I(Q,t)* with respect to time. We expand the relation of *S(Q,ω)* with space in Section 2.6. The scattering function is directly related to the differential cross sections through:

$$\left(\frac{d^2\sigma}{d\Omega dE'}\right)_{coh} = \frac{k'}{k}\frac{\sigma_{coh}}{4\pi}NS(Q,\omega) \tag{2.26a}$$

$$\left(\frac{d^2\sigma}{d\Omega dE'}\right)_{inc} = \frac{k'}{k}\frac{\sigma_{inc}}{4\pi}NS_i(Q,\omega) \tag{2.26b}$$

These expressions have two main components: a cross section, σ, and the scattering function *S(Q,ω).* The cross section only describes the interaction potential between the neutron and atoms in the system. The scattering function does not depend on the interaction properties of the neutron-nucleon interaction. Instead, *S(Q,ω)* depends only on the relative atomic positions and respective motions of the atoms in the scattering system. Hence, by measuring *S(Q,ω)* in a neutron scattering experiment, we probe information about both the spatial and temporal arrangement of atoms simultaneously. Neutron scattering provides the unique ability to access both the structure and dynamics of a material with a single measurement.

2.5 Diffraction

Consider a monochromatic beam that is incident on a crystal at an angle *Θ* with respect to a crystal plane. The beam is scattered elastically at an angle *Θ*, as illustrated in Figure 4. As the incident radiation is scattered from the crystal, a phase shift will occur between waves that are scattered from atoms on different crystal planes. Comparing a wave scattered from an atom on plane 1 to an atom located on plane 2, the second wave will have a longer path length. The path length difference is:

$$L = AB + BC = 2d\ sin\theta \tag{2.27}$$

where *d* is the distance between the planes. For complete constructive interference to occur between these two waves, the wavelength needs to be an integer value *n* of this path length difference. Therefore, we arrive at the well-known Bragg's law.

$$n\lambda = 2d\ sin\theta \tag{2.28}$$

Bragg scattering only occurs when *Q* corresponds to a reciprocal lattice vector. Even small deviations from the reciprocal lattice vector will cause the scattered waves to destructively interfere, resulting in rapid decay in the Bragg peak. A diffraction experiment measures the amount of scattered radiation (for example neutrons or X-rays) as a function of scattering angle. A diffraction experiment is a technique can be used to determine the spatial arrangement of atoms in reciprocal space, which can then be transformed to obtain the real space crystal structure. The long-range, time-averaged crystal structures are obtained by performing a Rietveld refinement to model the experimental diffraction pattern. This allows for the determination of many parameters, such as the atomic positions, atomic lattice parameters, displacement parameters, and site occupancy factors. The long-range structure is determined by fitting the Bragg peaks while the diffuse scattering located in between the Bragg peaks is removed using a background subtraction. A further discussion of Rietveld refinements is given in Section 4.2.1.

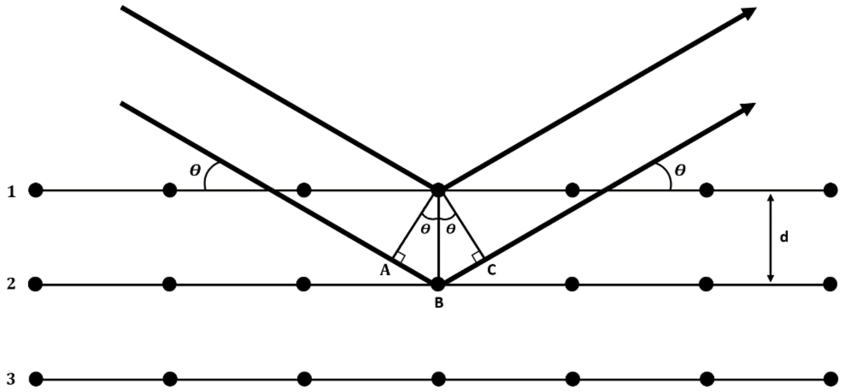

Figure 4**:** Diffraction of neutrons or X-rays by a crystal.

2.6 Pair Distribution Functions

In addition to Bragg scattering, there is a vast amount of information in the diffuse scattering signal that is often ignored while performing Rietveld refinements on diffraction data. The diffuse scattering is observed in the diffraction pattern as a weak signal in between the Bragg peaks. Unfortunately, the information contained in the diffuse scattering signal is typically lost during a Rietveld refinement because it is subtracted out by fitting a background to the diffraction pattern. Total neutron scattering experiments aim to collect and analyze all the coherent scattering signal, which is produced by Bragg peaks (global structure), elastic diffuse scattering (static local structure), and inelastic diffuse scattering (atomic motion). By performing a Fourier transform of the total scattering structure factor, *S(Q)*, the reduced pair distribution function (PDF) *G(r)* is obtained.[25, 26]

$$G(r) = \frac{2}{\pi}\int_0^{\infty} ((S(Q) - 1)\sin(Qr)\, QdQ \qquad (2.29)$$

An example of a PDF is shown in Figure 18 in Chapter 6. The atomic structure is represented by *G(r)* through the relation:[26]

$$G(r) = 4\pi r(\rho(r) - \rho_0(r)) \tag{2.30}$$

where $\rho_0(r)$ is the atomic number density. The atomic pair density, $\rho(r)$, takes the form:

$$\rho(r) = \frac{1}{4\pi r^2 N} \sum_{i,j \neq i} \frac{b_i b_j}{\langle b^2 \rangle} \delta(r - r_{ij}) \tag{2.31}$$

where summation over indices *i* and *j* is carried out across all the atoms in the material and r_{ij} is the distance between atom *i* and atom *j*. Using this expression for $\rho(r)$, one can observe that the PDF (*G(r)*) represents a weighted density of the distribution of atoms in real space. In other words, *G(r)* is a representation of how many atoms are located at a distance *r* from an atom at the origin. Note, the expression for *G(r)* is not dependent on time. For the diffraction scenario described in Section 2.5, the static approximation can be applied when the two incoming waves are moving so fast that the atoms in the sample do not move during the time of the scattering event. In reality, the energy of thermal neutrons is on the order of the relaxation times in materials, which does not make the static approximation completely valid (but it is still a very useful property for dynamics measurements). By including the diffuse scattering signal with the Bragg peaks in *S(Q), G(r)* therefore provides the ability to take a 'snapshot' in time of the local atomic structure. Information about the global structure is extracted from the Bragg peaks to determine the time-averaged, long range structure. *G(r)* therefore contains structural information on both the local and global length scales, giving you a complete description of the crystal structure. While the time averaged structure can appear to be highly ordered, the local structure may be disordered, which can have profound effects on the material properties. The most interesting material properties are often governed by the defects or local structure. The method to model total neutron scattering data is known as PDF analysis, which will be described in Section 4.2.2. PDF analysis and total neutron scattering was originally developed to model highly disordered systems, such as liquids and glasses, but can also be expanded to examine the local structure of crystalline materials.

As a closing remark, a connection between the various correlation functions should be given. Ignoring small differences in constants, $S(Q,\omega)$ is the Fourier transform of $I(Q,t)$ with respect to time while $I(Q,t)$ is the Fourier transform of $G(r,t)$ in space. Therefore, $S(Q,\omega)$ is the Fourier transform of $G(r,t)$ with respect to both space and time. These functions are central to the understanding of neutron scattering and will be referred to heavily throughout this manuscript.

3 EXPERIMENTAL METHODS

The energy and wavelength of cold/thermal neutrons makes them an ideal probe for studying the structure and dynamics of materials. The energies, typically on the order of a few meV, coincide perfectly with the energy levels of various dynamic processes in condensed matter, such as diffusion, rotational motion, phonons, etc. Likewise, the neutron wavelengths are on the order of interatomic distances, which allows diffraction to occur. Neutron scattering experiments simultaneously reveal information about the spatial arrangement of atoms as well as how the atoms are behaving. Neutron diffraction and total neutron scattering techniques use elastic scattering to investigate the local vs. global crystal structure. On the other hand, neutron spectroscopy uses quasielastic and inelastic scattering to understand the dynamic motion of atoms. In addition, the weak interaction of neutrons with the target atoms allows for deep sample penetration to measure the bulk properties. This feature also allows for the neutron beam to penetrate through bulky sample environments.

The neutron scattering experiments were conducted at BASIS,[27] VISION,[28] SNAP,[29] and NOMAD[30] at the Spallation Neutron Source (SNS) at Oak Ridge National Laboratory (ORNL) in Oak Ridge, TN, and HFBS[31] at the National Institute of Standards and Technology (NIST) in Gaithersburg, MD.

The following is a general overview of the instruments, experimental techniques, and sample environments used in this investigation. For a more detailed account of the experimental details of each experiment, such as sample masses, temperature and pressure measurement details, etc., the reader is referred to the Appendix for a complete description.

3.1 Sample Environments

The neutron scattering experiments conducted in this investigation required both standard and specialized sample environments due to the reactive nature of the samples and the extreme conditions (low and high temperature, high pressure). For many of the experiments, the required sample environments did not previously exist at the facilities and had to be designed and fabricated. For example, the samples are pyrophoric and must be handled in an inert gas environment (or vacuum) at all times. Many furnaces use unsealed sample containers at high temperature, which is insufficient for pyrophoric samples. In addition to a sealed sample can, the can needs to be vented to an expansion volume to prevent over-pressurization during heating and thermal decomposition. The expansion volume also stores the evolved hydrogen and deuterium gas for safe disposal. For measurements at less extreme conditions, standard sample environments were used. Due to the standard practice of using closed-cycle refrigerators (CCRs) and vacuum furnaces in neutron facilities, these sample environments will not be explained here. Instead, only the less common and customized sample environments that were modified for these experiments will explained in this section.

3.1.1 High Temperature

Two furnaces were used for high temperature experiments: a stick furnace and a *MICAS* furnace. The stick furnace, shown in Figure 5, was built specifically for high temperature experiments at the VISION beamline. The highest temperature reached with this sample environment was approximately T = 920 K. This consisted of a stick with gas ventilation that ran from the sample can through the stick and exited at the top. This was connected to a gas cabinet to allow for gas exchange, vacuum capabilities, and to vent the sample to an expansion volume. A cylindrical steel sample container was used. Annular heating blocks fit over the top and the bottom of the cell to heat the sample. Heating cartridges were embedded inside the heating blocks to produce the heat. A variety of cartridge heaters (diameter, length, resistance, etc.) were used in the experiments. Connecting the sample to a large expansion volume allowed the sample pressure to remain at atmospheric pressure for the entirety of the experiment, despite heating and sample decomposition. The system also allowed for evacuation of the sample and backfilling with helium gas.

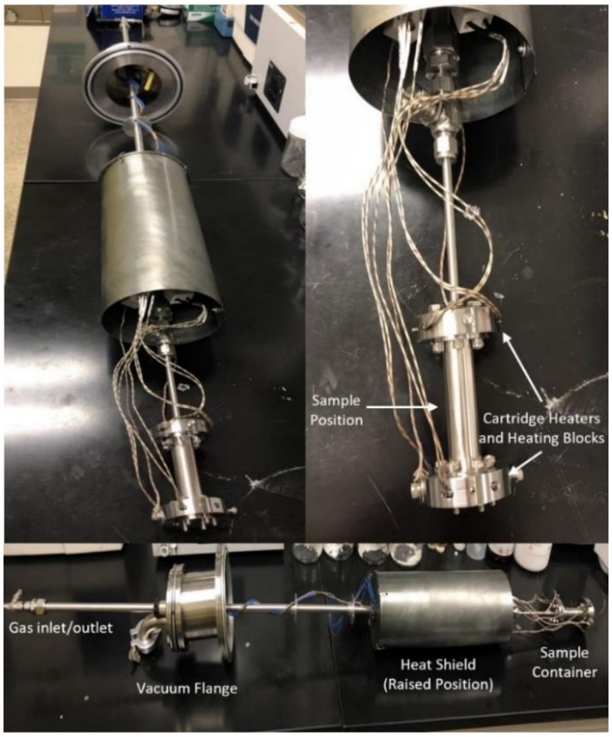

Figure 5: Custom stick furnace for VISION experiments. The vanadium heat shield is in the raised position, which is lowered for during measurements.

A *MICAS* furnace and stick was modified to measure pyrophoric samples at high temperatures for the experiments at BASIS and NOMAD. This type of furnace is common at SNS and can be installed at other beamlines around the facility. The stick assembly with sample holder (5 mm diameter quartz NMR tubes) are shown in Figure 6. The sample was vented to a gas cart with a 5L expansion tank. The NMR tubes were then connected to the stick using a *Swagelok* fitting. Due to the lower melting temperature of the quartz-metal interface, the NMR tubes were specially designed with extended lengths to keep the quartz-metal interface away from the heating elements.

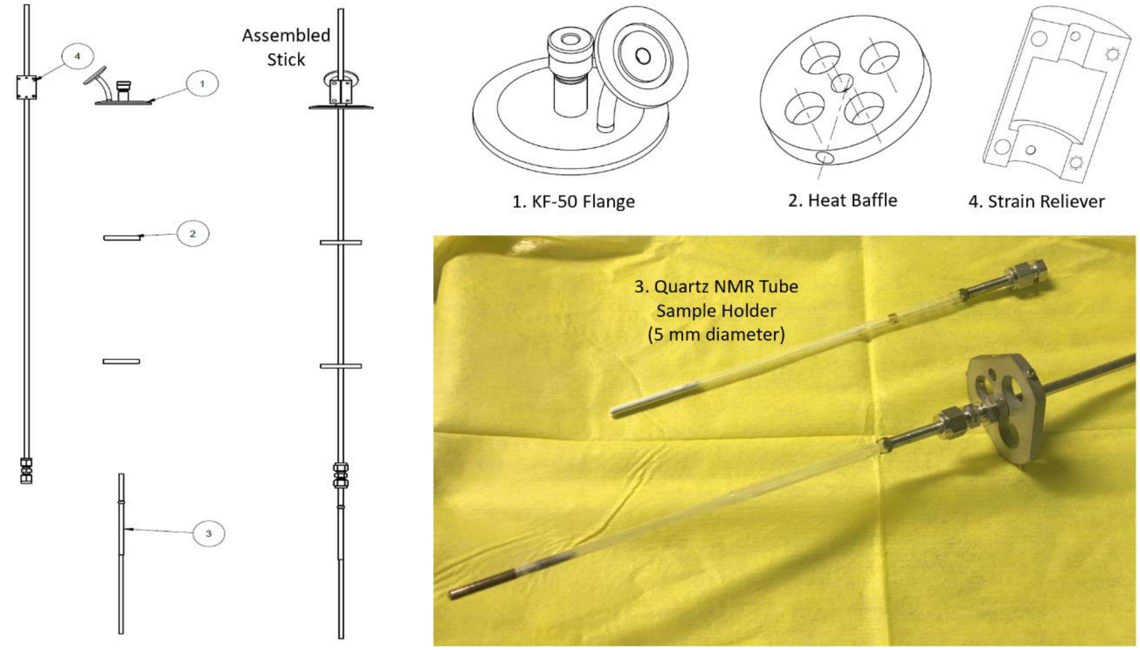

Figure 6: Stick assembly and parts for the experiments conducted in the *MICAS* furnace at BASIS and NOMAD.

3.1.2 High Pressure

High pressure experiments were performed at SNAP and BASIS. Paris-Edinburgh (PE) cells were used to apply the pressure for experiments at both beamlines. PE cells are a device that compresses a sample between two anvils at high pressures. Standard single toroidal cubic boron nitride anvils were used. For experiments at SNAP, the larger VX3-PE press was used while the smaller VX5 PE press was used at BASIS. The experiments can be divided into two main categories depending on the type of gasket used: (1) a standard encapsulated TiZr gasket and (2) a special split gasket made from CuBe in which the sample is loaded into a toroidal sample chamber. More details about the gaskets are given in Section 3.3.2.2. Since sample loading needs to be performed in an inert environment, loading was performed in a helium glovebox using a specially designed PE clamp system that surrounds the gasket-anvil assembly, as shown in

Figure 7. A load of approximately 5 tons was applied to the assembly using a hydraulic press and sealed under pressure in the glovebox. The entire clamp system was then removed and inserted into the PE press at the beamline.

For the QENS experiments at BASIS, an adapter was designed to lower the PE cell to the correct height in the neutron beam. This adapter can be observed in Figure 7, where the PE cell is connected to a modified vacuum flange with four long rods that supports the weight of the PE cell. An aluminum blast shield surrounds the PE cell to protect the instrument in the case of a gasket blowout. Cadmium foil was applied to the outside of the anvils to reduce background.

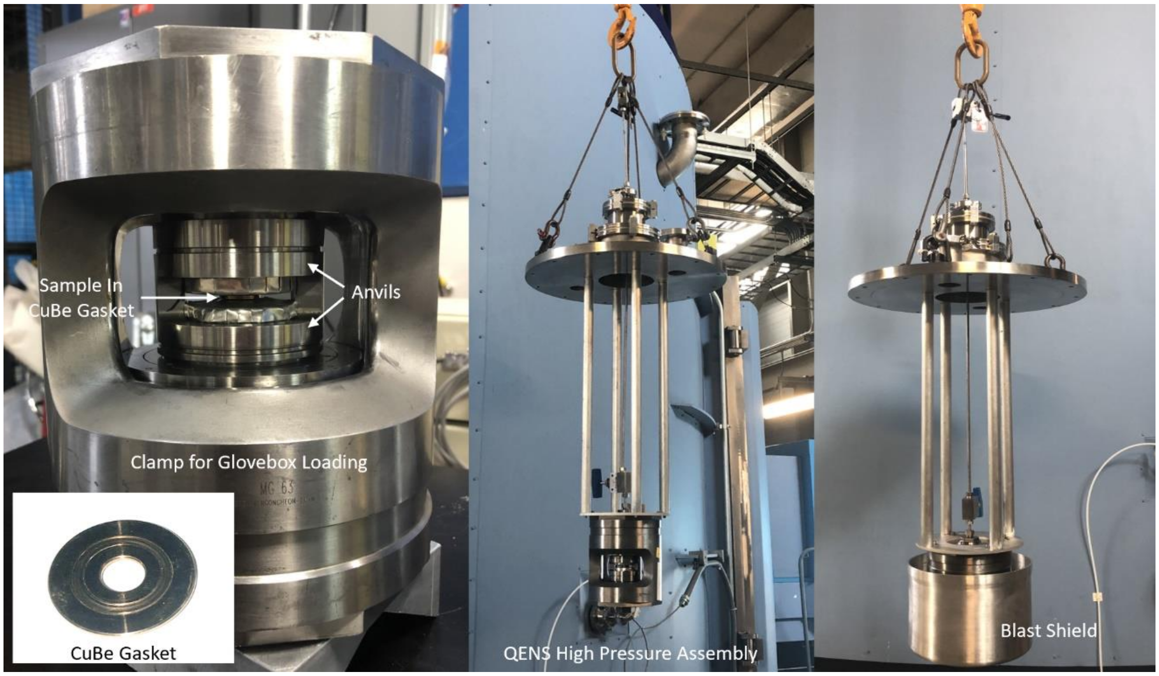

Figure 7: Paris-Edinburgh cell with a stand assembly for QENS experiments at BASIS. One of the CuBe gasket halves is shown.

3.2 Neutron Spectroscopy

Two different neutron spectroscopy techniques are used in this investigation to observe dynamic processes: quasielastic neutron scattering

(QENS) and inelastic neutron scattering (INS). INS in this case refers to powder-averaged measurements at a vibrational spectrometer. This should not to be confused with single crystal INS, i.e. triple axis spectroscopy. In this investigation, QENS is used to measure the diffusion of hydrogen while INS is used to probe the vibrational density of states (DOS).

3.2.1 Quasielastic Neutron Scattering

QENS instruments are specifically designed to measure very small energy transfers, on the order of µeV to a few meV. The energies associated with solid state diffusion are usually on the smaller end of this range. This corresponds to timescales of approximately the nanosecond (ns) to picosecond (ps) range, which is on the order of jump rates for solid state diffusion. In order to resolve energy transfers in this range, high resolution spectrometers are required. The most common quasielastic spectrometer for high resolution measurements are backscattering spectrometers. The QENS measurements were performed at BASIS and HFBS. These spectrometers are designed to be highly sensitive to low energy, incoherent processes, making it the ideal tool to probe the motion of hydrogen.

As the name suggests, quasielastic scattering is scattering that is almost elastic. A typical QENS spectra is shown in Figure 8. The spectra are centered around an energy transfer of zero, representing the elastic peak. The elastic peak is due to elastic scattering arising from the sample, instrument, and sample environment. To approximate the instrument resolution function, a low temperature measurement can be used. Low temperature measurements are preferred to model the elastic peak because the dynamics are ‘frozen’ on the time scale of the instrument. Vanadium standards can serve as alternatives for the resolution function if low temperature measurements were not possible. When a diffusive motion becomes observable on the time scale of the instrument, the elastic peak will lose intensity and begin to broaden. This broadening is the quasielastic signal that is measured and analyzed by a QENS experiment. The elastic intensity and the quasielastic intensity are therefore coupled. The broadening is directly proportional to the energy of the motion, and hence a time scale. As the diffusive motion speeds up, the broadening of the elastic peak will increase. Details about QENS data analysis can be found in Chapter 4.

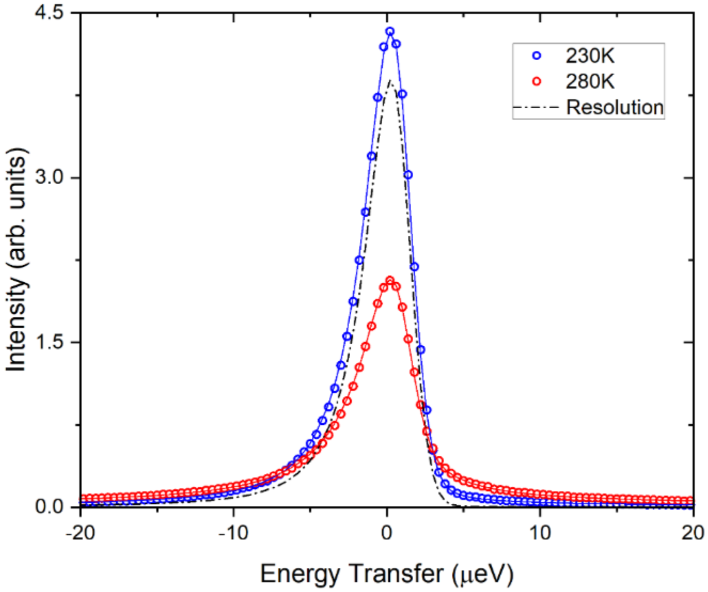

Figure 8: QENS spectra for plastic crystalline cyclooctanol measured at BASIS at Q = 1.0 Å^{-1} for the temperatures of 230 K and 280 K. The resolution function was measured at T = 20 K.[32]

Two different measurement configurations were used at BASIS by using the Si(111) and Si(311) analyzers to access different energy and Q ranges. Due to the higher resolution and narrower energy range, the Si(111) analyzers were used to observe slower diffusive motions on the ns timescale. However, if the motion became too fast for the Si(111) analyzers, a broader energy range was used which required use of the Si(311) analyzers. Instrument parameters including dynamic energy range, Q-range, and energy resolution (FWHM) are displayed in Table 2 for BASIS and HFBS. At BASIS, the instrumental resolution function was measured at T = 30 K for the CCR and 300 K for the furnace. For even slower motions, HFBS provides a finer energy resolution compared to BASIS with a FWHM = 0.8 µeV. At HFBS, the measurements were conducted using the standard instrument configuration with an accessible Q-range from 0.25 to 1.75 $Å^{-1}$ and an energy range of ± 16 µeV. Resolution function measurements were performed on empty vanadium cans. For QENS experiments, vanadium is also typically measured for detector normalization. Data reduction was performed using *Mantid.*[33]

Table 2: Instrument parameters for QENS measurements. Values for energy resolution, dynamic energy range, and Q-range are given.

Instrument	Energy Resolution (µeV)	Energy Range (µeV)	Q Range
HFBS	0.8	± 16	0.25 - 1.75
BASIS Si(111) Analyzers	3.5	± 100	0.2 - 2.0
BASIS Si(111) Analyzers	15	± 740	0.4 - 3.8

Many QENS experiments begin by performing an elastic energy window scan, commonly referred to as just an elastic scan. During an elastic scan, shorter QENS measurements (on the order of minutes) are taken as the temperature is slowly increased. For example, the elastic scan at BASIS consisted of short measurements taken in 10 K steps between 300 K and 880 K. In addition to temperature, elastic scans can also be conducted with increasing pressure. The elastic intensity can be fit by integrating a narrow area under the elastic peak at each individual temperature. An example of an elastic scan is shown in Figure 24 in Section 6.2. Plotting the elastic intensity vs. T will indicate changes in the observable dynamics. For example, a change in the slope of the elastic intensity may indicate the onset of observable hydrogen dynamics. In addition, a drastic discontinuity in the elastic intensity is an indication of a phase transition. Note, the exact method that elastic scans are measured is different at the various instruments. For example, doppler driven backscattering spectrometers at nuclear reactor sources (HFBS) are better suited than a time-of-flight backscattering spectrometer at a spallation source (BASIS) for measuring elastic scans. During the QENS experiments, various sample environments were used: CCR, furnace, and high-pressure PE cell.

3.2.1.1 Temperature Dependent QENS

For the CCR experiment at BASIS, samples were loaded into aluminum foil and formed into a thin packet of annular geometry to reduce multiple scattering effects. Annular aluminum foil packets are a common practice in neutron scattering measurements of hydrogenated materials. These samples were then loaded into cylindrical aluminum cans with aluminum foil seals. Resolution functions were measured at 30 K. All measurements were performed using the Si(111) analyzers. Elastic scans were performed between 30 K to 690 K. Longer QENS measurements (approx. 3 hours) were conducted at various temperatures between 300 K – 690 K.

The second BASIS experiment was performed in a *MICAS* furnace that was modified for measurements of pyrophoric samples. Samples were loaded into 5 mm diameter quartz NRM tubes. Resolution functions were measured at 300 K. Elastic scans and longer QENS measurements (approximately 3 hours long) were taken between 300 K and 920 K. All sample cans were evacuated in the furnace and backfilled to atmospheric pressure using helium. A large expansion volume hooked up to the sample stick allowed the pressure to remain constant throughout the entire experiment, i.e. during heating and gas evolution.

An additional QENS experiment was conducted at HFBS for higher resolution measurements. A bottom-loading CCR was used for BaH_2 and CaH_2 while a top-loading CCR was used for MgH_2. Titanium sample cans were used with gold O-ring seals (lead seal for MgH_2). Samples were loaded into aluminum foil packets in annular geometry. Elastic scans were performed for each sample. Longer QENS measurements were taken from up to a maximum temperature of 800 K. This experiment used the ± 15 μeV energy range configuration for all measurements.

3.2.1.2 High Pressure QENS

Two high pressure BASIS experiments were conducted on BaH_2. Both experiments used the same measurement configurations and sample environment. The experiments were conducted in a single-toroidal VX5 Paris-Edinburgh (PE) press. The sample environment is described in detail in Section 3.1.2. Samples were loaded into CuBe gaskets and sealed in the PE cell at a pressure of approximately 5 tons. Due to the reactive nature of the sample, a pressure transmitting medium was not used. All measurements were conducted at room temperature. An elastic scan was performed during the first experiment up to a maximum pressure of approximately 5 GPa. Measurements were approximately 50 minutes for each pressure and pressure increases were conducted in 5 ton steps. The second experiment consisted of longer QENS measurements of approximately 22 hours at each pressure up to a maximum pressure of 7.1 GPa. The resolution function was measured at ambient conditions. Pressures were estimated from previous diffraction experiments at SNAP, as described in Section 4.3.

3.2.2 Inelastic Neutron Scattering

Powder inelastic neutron scattering is a type of vibrational spectroscopy that probes the vibrational DOS of a material. This provides information about lattice dynamics, such as phonon mode energies, chemical bonding, molecular structure, etc. INS spectra can be used to determine the contributions of the lattice vibrations to the heat capacity, which in turn can be used to calculate thermodynamic potentials. INS is complimentary to the light scattering techniques of Raman and infrared (IR) spectroscopy. However, unlike their phonon counterparts, INS is not governed by selection rules. This makes analysis and modeling of INS spectra a relatively straightforward process. As was also the case for incoherent QENS, INS instruments are incredibly sensitive to hydrogen. This allows the spectra to be heavily weighted in favor of hydrogen vibrations, which are difficult to measure using other techniques.

The INS experiments conducted in this investigation were performed at VISION at SNS, ORNL.[28] VISION has an accessible energy range from the elastic limit up to 500 meV with an energy resolution of $\Delta E/E \approx$ 1-2% across the entire energy range. The energy region of interest for the metal hydrides in this investigation is located between approximately 50 – 250 meV. Sample environments included a CCR for low temperature measurements and a custom stick furnace for high temperature measurements. The stick furnace is described in more detail below in Section 3.1.1. Data reduction was performed using *Mantid.*[33]

3.3 Diffraction

X-ray and neutron diffraction are traditional techniques to determine the crystal structure of materials. Three different diffraction techniques were used in this investigation: X-ray diffraction (XRD), neutron powder diffraction (NPD), and total neutron scattering. XRD and NPD probe the long range (global) crystal structure while total neutron scattering examines both the short (local) and long (global) range crystal structures.

3.3.1 X-Ray Diffraction

XRD was primarily used in this investigation for sample characterization and quality determination during sample synthesis. Rietveld refinements were rarely performed on the XRD data sets. Diffraction patterns were compared to previously reported results to guide and verify our synthesis methods. XRD measurements were performed on a *PANalytical X'Pert PRO* diffractometer with Cu K_α radiation. Due to the pyrophoric nature of the sample, the powder was covered with parafilm on a glass slide to reduce exposure to air. Measurements were conducted in the standard Bragg-Brentano geometry, typically with a scan range of $2\Theta = 25^\circ – 70^\circ$ and average measurement times of approximately 45 minutes.

3.3.2 Neutron Diffraction

NPD measurements were conducted at NOMAD and SNAP. NOMAD is an instrument that specializes in providing high resolution neutron PDF measurements. In addition to the PDF measurements, NOMAD also provides neutron diffraction data. SNAP is an instrument designed specifically for high pressure NPD experiments. The experiments can be divided into two main groups: a temperature dependent study at *NOMAD* and a pressure dependent study at *SNAP*.

3.3.2.1 Temperature Dependent NPD

A series of temperature dependent experiments were conducted at NOMAD to obtain high quality PDF and NPD data. Two different sample environments were used: a cryostream sample shifter between 100 K – 500 K and a *MICAS* furnace with a specially designed sample stick for measurements of pyrophoric samples up to 920 K. The cryostream sample shifter measures higher quality (lower instrument background) data. Samples were measured in vanadium PAC cans (6 mm diameter) with a copper seal. For the MICAS furnace measurements at NOMAD, samples were loaded into 5mm diameter quartz NMR tubes. Empty sample holders, silicon, diamond, and vanadium were used for data normalization and generating instrument parameter files for all the experiments. Measurements were approximately 1.5 hours at each temperature. Add more information about Q-range, etc. once data analysis is complete.

3.3.2.2 High Pressure NPD

Two high pressure neutron diffraction experiments were performed at SNAP. The experiments can be divided into two main categories depending on the type of gasket used: (1) a standard encapsulated TiZr gasket and (2) a special split gasket made from CuBe that allows for sample loading into the toroidal chamber.

No pressure transmitting medium was used in these experiments. Sample loading was performed in a helium glove box using a specifically designed PE clamp system that surrounds the gasket-anvil assembly, as shown in Figure 7. A load of approximately 5 tons is applied to the assembly using a hydraulic press and sealed under pressure in the glovebox. The entire clamp system can then be removed and inserted into the PE press at the beamline.

A detailed description with illustrations of the TiZr encapsulated gasket design for single toroidal anvils and the PE cell assembly is presented in the reports by Marshall and Francis[34] and by Klotz et al.[35] As for the vast majority of gaskets, the sample sits in the center opening of the gasket. Encapsulation is ensured through two cups of TiZr that cover the sample at bottom and top. The powder samples are first pressed into a pellet before being transferred inside the TiZr gaskets and sealed.

The other type of gasket is made from CuBe. For these experiments, we again adapted a specialized setup that was designed for QENS experiments by Klotz and Bove et al.[36, 37] Here we use a split gasket where the sample space is located inside the toroid to form a fully encapsulated annulus. One of the CuBe gasket halves is shown in Figure 7. However, the sample space in our experiment was increased compared to the original design by Klotz and Bove et al.[36, 37] The dimensions of our CuBe gasket are 13.2 mm outer diameter, 10.4 mm inner diameter, and a groove of 0.79 mm depth, which forms a toroidal pressure chamber volume of 81.6 mm^3 once the two parts are put together. This CuBe gasket was used in the high pressure QENS measurements to reduce multiple scattering. The purpose of measuring this gasket at SNAP was to obtain a pressure-load curve to determine the pressures measured in the QENS experiments. While the TiZr gaskets are zero (null) scattering, CuBe scatters strongly and produces a large signal in the data.

All measurements were conducted at room temperature. Instrument specific parameters for the refinements were determined by measuring a nickel sample in the same position and sample configuration as the sample. Empty sample containers and vanadium samples were also measured for data reduction and normalization. Measurements times ranged from 2 – 6 hours at each pressure for the TiZr gasket measurements and approximately 1 – 2 hours for the CuBe gasket measurements. Details about pressure determination methods can be found in Section 4.3. Data reduction was performed using *Mantid*[33] and Rietveld refinements were conducted using *GSAS-II*.[38]

4 DATA ANALYSIS METHODS

The methods of data analysis used in this investigation range from qualitative observations to complex, novel approaches. The general approach will be outlined in this chapter with more specific details given in the results and discussion of Chapters 6 – 8.

4.1 Quasielastic Neutron Scattering

The QENS fitting procedure performed in this investigation was conducted using the *QCLIMAX* package within *ICE-MAN*, the Integrated Computational Environment-Modeling & Analysis for Neutrons.[39] *ICE-MAN* has been recently developed at ORNL for analysis of neutron scattering data. Many other facilities use other software packages, of which the most common is arguably *DAVE*.[40] This investigation is one of the earliest studies to report results using *QCLIMAX*. Here, we employ a novel approach to extend the traditional fitting procedure by applying constraints to the fitting model.

The following sections will introduce the general approach to QENS data fitting for solid state diffusion. This will include a discussion of the various jump diffusion models and how to apply to extract useful information. The general fitting procedure will then be expanded to include model constraints using *QCLIMAX*.

4.1.1 QENS Data Analysis

The following is the typical data fitting procedure used for QENS data. The measured signal at a QENS experiment, $S(Q,E)$, can be fit using the following equation:

$$S(Q,E) = f\left[X(Q)\delta(E) + \big(1 - X(Q)\big)S_{qe}(Q,E)\right] \otimes R(Q,E) + B(Q,E) \tag{4.1}$$

where, $X(Q)$ is the fraction of elastic scattering, known as the elastic incoherent structure factor (EISF), $\delta(E)$ is the elastic signal, and $S_{qe}(Q,E)$ is the model representing the quasielastic scattering. These terms are numerically convoluted with the resolution function *R(Q,E)* and *B(Q,E)* is the linear background term. Each distinct dynamic process observed in the spectra is modeled by a Lorentzian function. For a data set consisting of two distinct dynamic processes, a two Lorentzian expression is used:

$$S_{qe}(Q,E) = \left(1 - P(Q)\right)\frac{1}{\pi}\frac{\Gamma_1(Q)}{E^2 + \Gamma_1^2(Q)} + P(Q)\frac{1}{\pi}\frac{\Gamma_2(Q)}{E^2 + \Gamma_2^2(Q)} \qquad (4.2)$$

where (1–*P(Q)*) and *P(Q)* represent the spectral weights of the broad and narrow Lorentzian terms of half-width at half maxima (HWHM) Γ_1 and Γ_2, respectively. The HWHM is inversely proportional to the characteristic time-scale of the measured dynamic process. Note, only the first term is used for the one Lorentzian model.

After fitting the data using Eq. (4.1) and Eq. (4.2), the Lorentzian widths can be plotted as a function of momentum transfer, i.e. Γ(Q) vs. Q or Q^2, as displayed in Figure 9. By examining the HWHM as a function of momentum transfer, the nature of the observed dynamic process can be determined, i.e. translational diffusion, diffusion in confinement, rotational motion, etc. Solid state diffusion typically occurs in distinct jumps. Therefore, the concept of jump diffusion models will be explained in detail below.

4.1.2 Jump Diffusion Models

A discussion on solid state diffusion is incomplete without a description of jump diffusion models. Early diffusion models sought to describe the diffusive motions observed in some liquids and gasses. This resembled an unrestricted, continuous diffusion process (Brownian motion) that is described by Fick’s Law. However, solid state hydrogen diffusion diverges from this description and instead involves jump diffusion amongst well defined lattice sites. Multiple jump diffusion models have been developed over the years, of which the most common are the Chudley-Elliott,[41, 42] Singwi-Sjölander,[43] and the Hall-Ross[44] models.

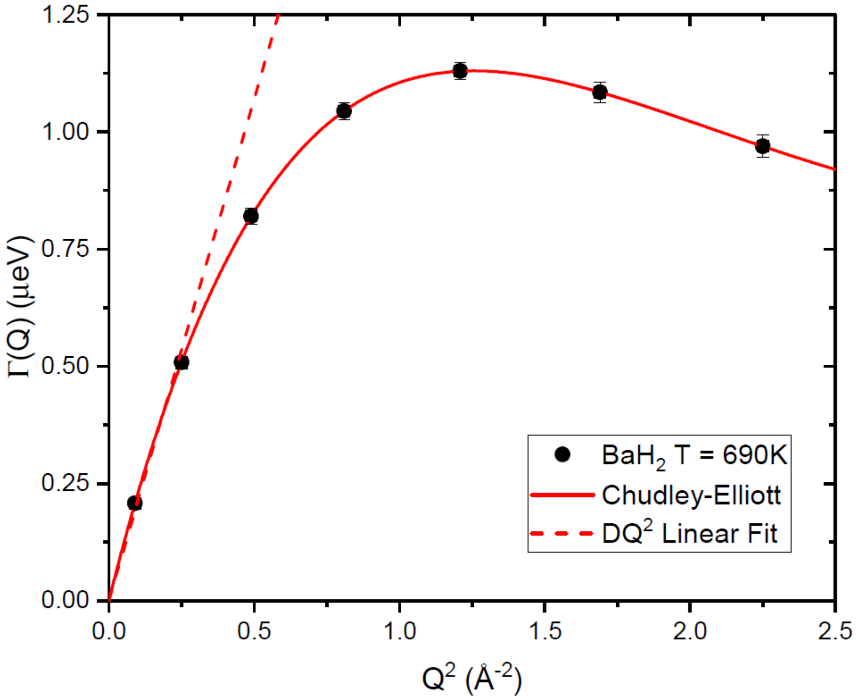

Figure 9: Q^2 dependence of the HWHM of the Lorentzian broadening. A DQ^2 behavior is observed for unrestricted diffusion. The Chudley-Elliott jump diffusion model diverges from the DQ^2 behavior with increasing Q.

For a diffusive motion observed with QENS, the broadening of the Lorentzian function at low momentum transfers follows the characteristic DQ^2 dependence associated with long-range translational diffusion, as seen in Figure 9. At high Q (shorter distances), the broadening deviates from the DQ^2 dependence, which yields information about the nature of the elementary diffusion process. The *Q*-dependence of the intermediate and high *Q* regions is where the distinction can be made between the different jump diffusion models. The QENS broadening for the Chudley-Elliott (Eq. (4.3a)), Singwi-Sjölander (Eq. (4.3b)), and Hall-Ross (Eq. (4.3c)) models are described by, [41-44]

$$\Delta E(Q) = \Gamma(Q) = \frac{\hbar}{\tau}\left[1 - \frac{\sin QL}{QL}\right] \tag{4.3a}$$

$$\Delta E(Q) = \Gamma(Q) = \frac{\hbar D Q^2}{1 + DQ^2\tau} \tag{4.3b}$$

$$\Delta E(Q) = \Gamma(Q) = \frac{\hbar}{\tau}\left[1 - e^{-DQ^2\tau}\right] \tag{4.3c}$$

where L is the jump length, τ is the residence time, and D is the diffusion coefficient. Two of the three parameters are extracted from the fitting procedure and can be used to calculate the third through the following relation.

$$D = \frac{L^2}{6\tau} \tag{4.4}$$

The Singwi-Sjölander jump diffusion model describes a combination of oscillatory motion with directed jumps, while the Hall-Ross model uses a distribution of jump lengths. As will be demonstrated later, the solid-state diffusion process in the metal hydrides studied in this investigation are best described by the Chudley-Elliott model. This model describes discrete jumps on a lattice. It is assumed that the particle resides in the same average position for a characteristic residence time (τ), only undergoing small amplitude thermal oscillations. After remaining in that position for the residence time, the particle rapidly jumps over a discrete distance to another available site. A comparison of the Q-dependence of the quasielastic broadening for the Chudley-Elliott, Singwi-Sjölander[43] and Hall-Ross[44] models for a metal hydride (BaH_2) is shown in Figure 10. The Q-dependence is clearly different between the models across the Q-range and the best fit is provided by the Chudley-Elliott model. The microscopic origin of each model needs to be considered carefully to determine if it is applicable to the system being investigated. In our case, the choice of the Chudley-Elliott jump diffusion model is justified because this model is designed to describe diffusive jumps among lattice sites in a crystal.

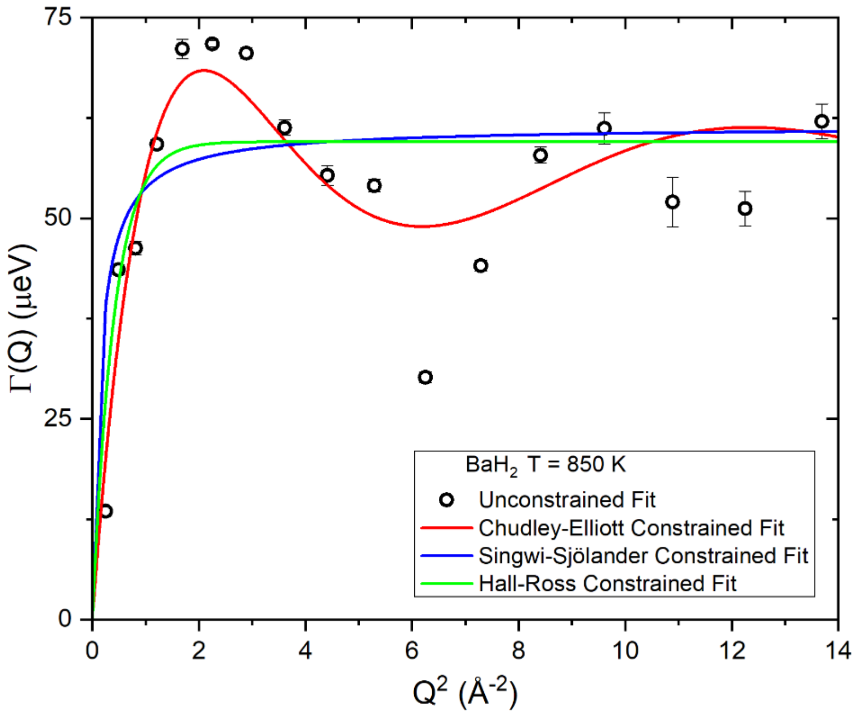

Figure 10: Comparison of three different jump diffusion models: Chudley-Elliott, Singwi-Sjölander, and Hall-Ross.[41, 43-45]

4.1.3 Data Analysis Using QClimax

As mentioned previously, the QENS data fits in this investigation were performed using the *QCLIMAX* package within *ICE-MAN*, the Integrated Computational Environment-Modeling & Analysis for Neutrons.[39] The purpose of the following sections is to introduce the *QCLIMAX* data fitting process used in this investigation. Since *QCLIMAX* is a relatively new program that is still being developed, we have included a section that compares the results from *QCLIMAX* to the tried-and-true software package *DAVE* in order to justify our data analysis methods and validate our results.

4.1.3.1 Applying Model Constraints

The fitting procedure begins with a so-called unconstrained fit, where the Lorentzian widths can assume any value. In other words, the data is fit using Eq. (4.1) with the quasielastic scattering term described by Eq. (4.2). It is necessary to perform an unconstrained fit first (before adding constraints) to understand what type of dynamics are occurring in the material. An example of the HWHM for BaH_2 at T = 850 K is shown in Figure 11. The unconstrained model is shown in the black circles and the resulting fit of the Chudley-Elliott model is shown as the solid black line. The initial unconstrained fit clearly shows a diffusive motion that is described by the Chudley-Elliott model. Now that the underlying behavior is understood, we can further improve the fitting procedure by introducing constraints to the model.

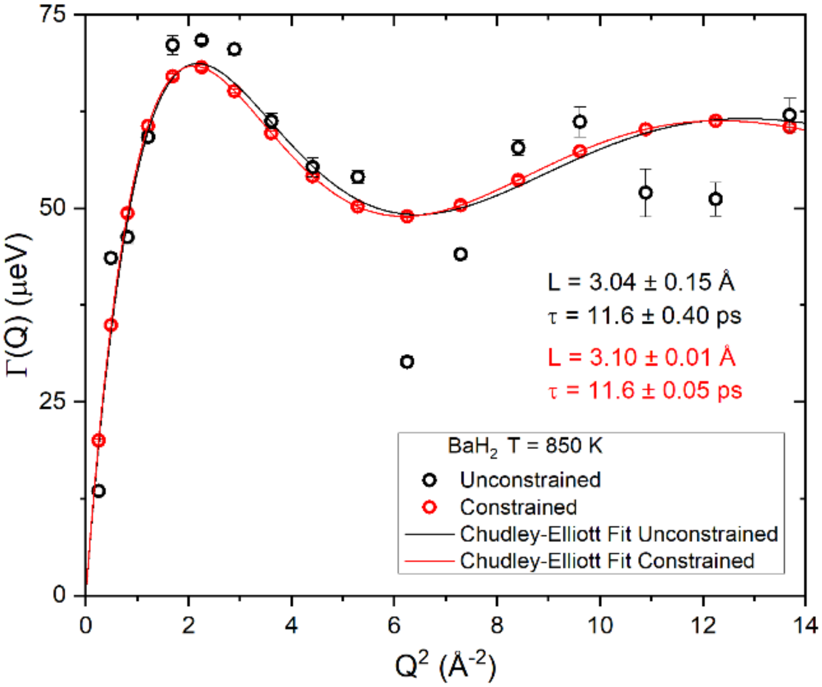

Figure 11: Comparison of unconstrained vs. constrained fits using *QCLIMAX* for BaH_2 at T = 850 K.[45]

As seen with the unconstrained data (black circles) in Figure 11, the widths have some noticeable deviations from the ideal Chudley-Elliott relationship. These deviations occur for many reasons, such as coherent scattering effects (Bragg peaks) and statistical uncertainty. As will be discussed later in this section, these deviations can greatly complicate data analysis using only unconstrained fitting models. A method to improve the accuracy and to reduce the errors is to apply constraints to the fitting procedure.

Since the motion is clearly explained by the Chudley-Elliott jump diffusion model, the Lorentzian widths should follow a well-described relationship with Q. Therefore, we can use *QCLIMAX* to constrain the Lorentzian widths to follow the Chudley-Elliott model. The software simultaneously fits the data to the equations as a function of Q, effectively fitting $S_{qe}(Q,E)$ to the following quasielastic model:

$$S_{qe}(Q,E) = \frac{1}{\pi}\frac{\frac{\hbar}{\tau}\left[1-\frac{\sin QL}{QL}\right]}{E^2+\left(\frac{\hbar}{\tau}\left[1-\frac{\sin QL}{QL}\right]\ \right)^2} \tag{4.5}$$

and determining by minimization the parameters L and τ. Eq. (4.5) is just a modification of Eq. (4.2) (first term only) by plugging in Eq. (4.3a) for the half-widths, Γ(Q). By systematically fitting all the Q values simultaneously, the weight on the outlier data points is reduced and the fitting procedure converges on a more accurate value for the parameters. The constrained fit is shown in red (circles and solid line) in Figure 11. It can be observed that the overall fit is very similar to the unconstrained fit, but the errors for L and τ have been reduced by introducing the constraints.

The power of having the ability to add constraints to a model using *QCLIMAX* is fully appreciated for lower quality data or for very weak, narrow QENS signals. Figure 12 shows a comparison of unconstrained fits that were performed with *DAVE* to the constrained fits performed with *QCLIMAX* for BaH_2 at 670 K and 750 K. The higher temperature data in Figure 12b is easier to fit because of the larger QE intensity and broader Lorentzian widths at the higher temperature when compared to the 670 K data. Therefore, both the unconstrained and constrained models yield the same results. However, the lower temperature data is very difficult to fit accurately using the unconstrained model because of the low intensity and narrow broadening. The fit of the Chudley-Elliott model (black solid line) does not adequately describe the widths, which will yield vastly different jump lengths, residence times, and diffusion coefficients. On the other hand, the constrained fit is a better description of the unconstrained widths. Therefore, adding model constraints is a great method to increase the accuracy of QENS results, especially for poorer quality data.

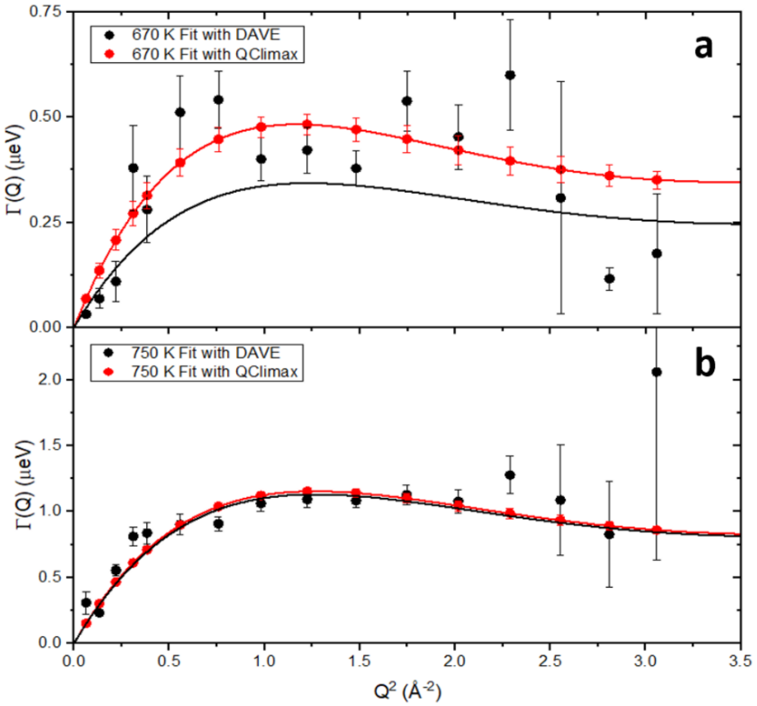

Figure 12: Unconstrained fits (red circles and solid lines) that were performed with *DAVE* compared with fits constrained to follow the Chudley-Elliott jump diffusion model (black circles and solid lines) for BaH_2 at (a) 670 K and (b) 750 K.[45]

4.2 Diffraction and Total Neutron Scattering

X-ray diffraction was primarily used in this study for sample characterization after synthesis to verify sample purity. As a result, the diffraction patterns were compared to previously reported results. Full Rietveld refinements were rarely carried out for the XRD data but were performed for the neutron powder diffraction experiments at NOMAD and SNAP. For the total scattering experiments at NOMAD, PDF analysis was performed.

4.2.1 Rietveld Refinements

The crystallographic calculations performed in this study for neutron diffraction data were carried out using Rietveld refinements in the software program *GSAS-II*.[38] Rietveld refinements are the traditional method for structural analysis and complete details of this technique can be found elsewhere.[46] In a basic summary, a Rietveld refinement is a method that uses a least squares approach to refine parameters in a theoretical structural model until the theoretical diffraction pattern matches an experimentally measured diffraction pattern.

The refinements performed in this investigation were relatively basic structural determinations. Refined parameters for the phases consisted of lattice parameters, phase fractions, histogram scale factors, atomic coordinates, anisotropic atomic displacement factors (U), and pseudo-Voigt profile parameters. In all of the refinements, effort was made to minimize the amount of refinable (free) parameters in the calculations. Introducing too many free parameters into a model often provides an excellent fit to the data, but the result can be meaningless. For example, preferred orientation corrections were not applied even though it could improve the data. In addition, full refinements were not carried out on impurity phases and signals arising from sample environments (i.e. anvils at SNAP) to reduce the number of free parameters. Typically, only lattice parameters and phase fractions were refined for these phases.

To conduct a successful refinement on diffraction data, instrument specific parameters need to be determined with accuracy. If the instrument is not properly aligned and calibrated, this error will be reflected in the data, i.e. wrong peak widths, peak intensities, scattering angles, and the results will be meaningless. Therefore, a refinement of a standard reference sample (Si, LaB_6, etc.) is used to determine the instrument dependent parameters. At a high throughput neutron diffraction instrument, an instrument parameter file will often be provided by the instrument team. However, due to the unique sample environments used at NOMAD and SNAP for our experiments, we had to make our own instrument parameter files. A detailed description of how to produce the instrument parameter files for a calibration sample is explained in the tutorials for *GSAS-II* (https:// subversion.xray.aps.anl.gov/pyGSAS/Tutorials). Calibration samples were nickel at SNAP and silicon (SRM Si640e) at NOMAD.

4.2.2 PDF Analysis

PDF analysis on the NOMAD data was performed using the software package *PDFGUI.*[26] Complete details about the software program and the PDF method can be found in the previous reference. The PDF analysis method is in many ways similar to the Rietveld refinements. For example, various parameters in a theoretical model structure are refined to generate a theoretical PDF pattern that matches an experimentally measured PDF. Refined parameters included lattice constants, scale factors, atomic coordinates, anisotropic atomic displacement parameters (U), site occupancies, and parameters accounting for correlated atomic motion (*delta1* or *delta2* depending on temperature). In some cases, the deuterium site occupancies were fixed if they varied unreliably with temperature. A main difference is that PDF analysis calculates a model in real space while Rietveld refinements are calculated in reciprocal space.

As was the same for the traditional neutron diffraction experiments, a calibration sample needs to be measured to account for the instrument specific parameters at NOMAD. This was conducted by measuring a silicon (SRM Si640e) calibration sample or diamond and modeling the PDF data in *PDFGUI*. Values for *Qdamp* and *Qbroad* were determined from this calculation, which accounts for instrument resolution effects. *Qdamp* is a term that accounts for damping of the PDF pattern due to limited Q resolution. *Qbroad* is a term that corrects for peak broadening effects due to increased noise at higher Q values.

4.3 Pressure Determination Methods

The following sections will give a detailed overview of the methods used to determine the sample pressures for the high pressure experiments. Different methods were used to estimate the pressures depending on what type of gasket was used. Therefore, this section is divided into two partss: (1) SNAP experiment with the TiZr gasket and (2) SNAP and BASIS experiments with CuBe gasket.

4.3.1 SNAP Experiment with TiZr Gasket

The first experiment was performed at SNAP by measuring BaD_2 in a TiZr gasket. Pressure was estimated using a third order Birch-Murnaghan equation of state of the form,[47]

$$P(V) = \frac{3B_0}{2}\left[\left(\frac{V_0}{V}\right)^{\frac{7}{3}} - \left(\frac{V_0}{V}\right)^{\frac{5}{3}}\right]\left[1 + \frac{3}{4}(B' - 4)\left[\left(\frac{V_0}{V}\right)^{\frac{2}{3}} - 1\right]\right] \qquad (4.6)$$

where B_0 is the bulk modulus, $B' = \left(\frac{\partial B}{\partial P}\right)_{P=0}$, and V_0 is the reference volume. This calculation was carried out using calculated parameters determined for BaH_2.[48] Actual values for BaD_2 are not expected to differ significantly from those of BaH_2. For the orthorhombic phase, B_0 = 31.2 GPa, B'= 3.2, and V_0 = 221.5 Å^3. For the hexagonal phase, B_0 = 34.7 GPa, B'= 3.6, and V_0 = 103.24 Å^3. In addition, calculated and experimental values reported from Smith et al. were also tested and yielded similar results.[49] A comparison of the load applied to the PE press and the corresponding sample pressure is shown in Figure 13. The structural phase transition to a higher density phase causes a sharp increase in the sample pressure despite a small difference in the applied pressure range. The highest pressure achieved in this experiment with the TiZr gasket is approximately 11.3 GPa.

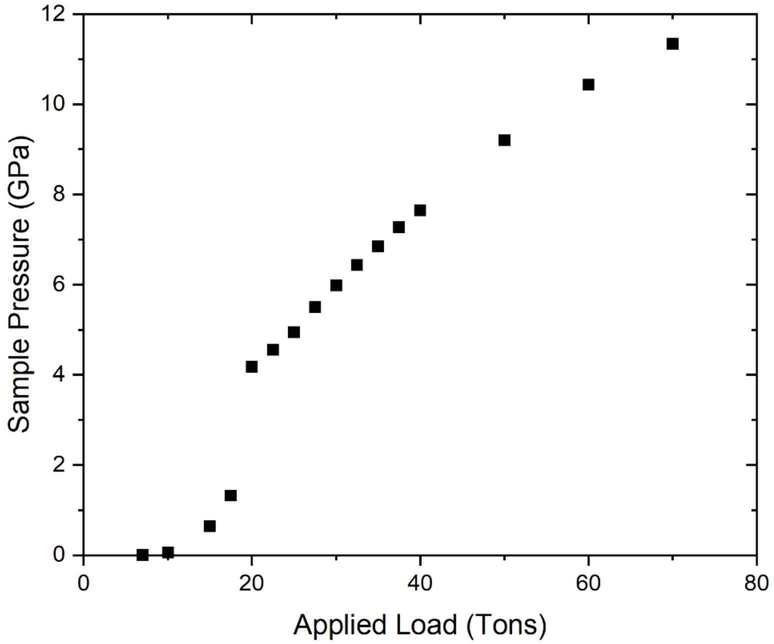

Figure 13: Pressure-load curve for BaD_2 in a TiZr gasket.

4.3.2 SNAP and BASIS Experiments with CuBe Gasket

Two different experiments were conducted using the CuBe gasket: a diffraction experiment at SNAP and a QENS experiment at BASIS. The diffraction experiment was necessary to obtain a pressure-load curve for the CuBe gasket so that the pressures measured at BASIS could be estimated. For experiments at SNAP, the larger VX3-PE press was used while the smaller VX5 PE press was used at BASIS.

For the SNAP experiment using the CuBe gasket, diffraction patterns were measured at a series of 22 pressures ranging from 7.5 tons to 75 tons to obtain a pressure load curve. By observing the pressure dependence of the CuBe Bragg peaks, the gasket began deforming under an applied load of roughly 24 tons, as shown with the (311) CuBe peak in Figure 14a. Likewise, the BaD_2 peaks started to shift at the same pressure (24 tons), as evidenced by the (211), (112), and (210) peaks displayed in Figure 14b. Therefore, 24 tons is the load that was needed to start deforming the gasket and begin applying pressure to the sample. CuBe is a stiffer gasket compared to TiZr, which explains in the large difference in applied loads needed to begin gasket deformation. In addition, Figure 14a shows how strong the scattering signal is from the CuBe gasket compared to the BaD_2 sample.

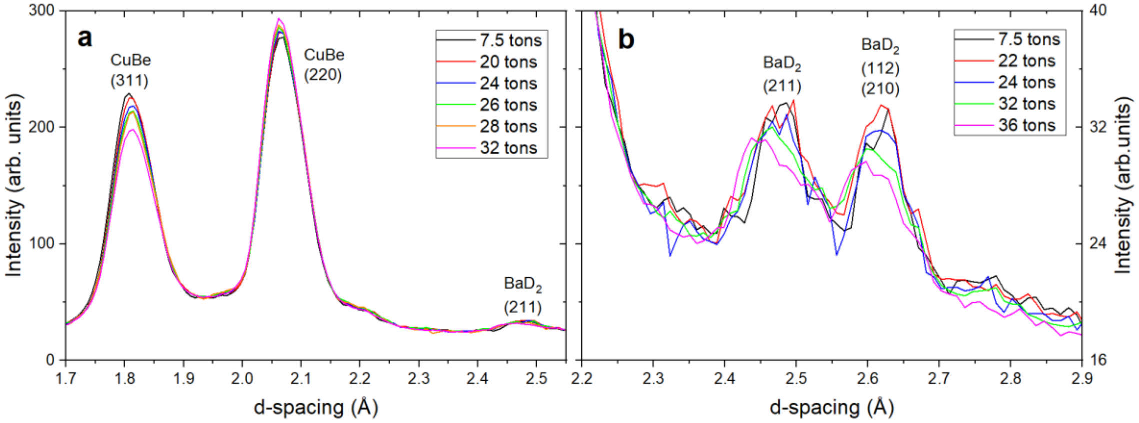

Figure 14: SNAP diffraction pattern summed over the high-angle column of the low angle detector bank (~ 59º – 74º) for BaD_2 in a CuBe gasket.

Diffraction patterns corresponding to loads between the range of 40 – 75 tons is displayed in Figure 15. When comparing the 40 ton and 50 ton patterns, the emergence of a series of Bragg peaks can be observed. These Bragg peaks correspond to the hexagonal phase of BaD_2. Therefore, the structural phase transition occurs between these two pressures. We therefore assign this 50 ton data set as the point where the hexagonal phase is completely formed. This allows us to determine the correlation between the pressure-load curve for this CuBe gasket with the pressure-load curve for the TiZr gasket shown in Figure 13. Namely, for the TiZr gasket at a load of 25 tons (or 5 GPa), most of the sample was transformed into the hexagonal phase as only 11 mol% of the orthorhombic phase remained. Thus, while using a conservative estimation, the pressure at a load of 50 ton for the CuBe gasket is equivalent to the pressure at the load of 25 ton for the TiZr gasket. We therefore set this pressure as the V_0 point for the hexagonal phase. Next, V/V_0 was calculated for the TiZr gasket data as a function of pressure and a polynomial was fit to this data. Likewise, the (202) and (110) peaks for BaD_2 were used to calculate the cell volumes for the CuBe gasket, which was again converted into V/V_0. The values determined from the polynomial were applied to the CuBe cell volumes to determine the corresponding sample pressures, as displayed in Table 3. However, the SNAP experiment only reached an applied load of 75 tons while the BASIS experiment reached a maximum load of 90 tons. Therefore, a second polynomial was fit to the V/V_0 values for the CuBe gasket as a function of pressure in order to extrapolate our pressure-load curve. Using the second polynomial values, the corresponding cell volume could be determined by extrapolating the pressure up to 90 tons. Comparing this cell volume to the TiZr experiment yielded a maximum sample pressure of approximately 7.1 GPa.

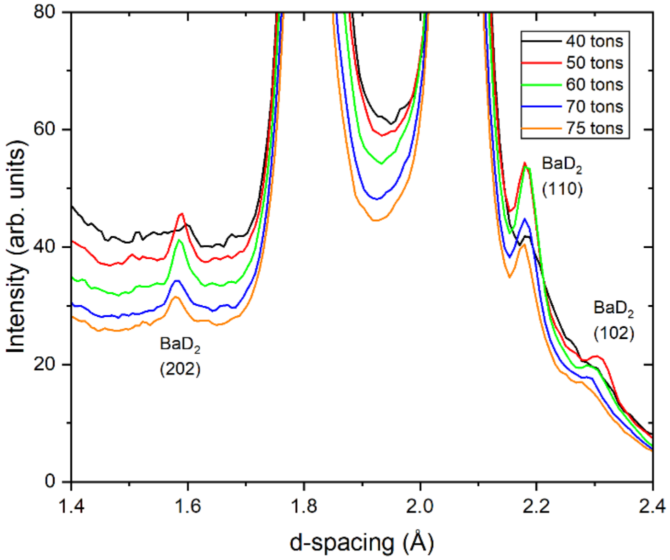

Figure 15: SNAP diffraction pattern summed over the center column of the high angle detector bank (~ 97º – 113º) for BaD_2 in a CuBe gasket.

Table 3: Hydraulic load applied to PE press and corresponding sample pressures for the QENS experiment at BASIS.

Applied Load (tons)	Sample Pressure (GPa)
10	0
50	4.9
75	6.2
90	7.1

4.4 Inelastic Neutron Scattering

The data analysis methods for the INS measurements in this investigation are mostly qualitative (visual). The traditional way to model INS data is to compute the vibrational DOS by computational methods, such as density functional theory (DFT) and molecular dynamics (MD). However, these calculations are typically carried out only at low temperatures (a few Kelvin) and not at the high temperatures investigated in this work. Nonetheless, the lattice dynamics of the systems in this investigation (BaH_2, CaH_2, and MgH_2) have been studied previously through theoretical and experimental methods.[50-57]

Temperature dependent INS is an excellent technique to investigate how structure plays a role in hydrogen dynamics. Diffusion is inherently a phonon driven process. Therefore, it is important to understand the temperature evolution of these modes. The measurements at neutron powder vibrational spectrometers, such as VISION at ORNL, are averaged over a wide Q-range. To study specific modes in great detail to observe effects such as dispersion, a higher Q-resolution instrument would be needed, such as triple axis spectrometers. Nonetheless, powder averaged INS can provide plenty of information about the temperature evolution of the vibrational modes. The coherent coupling of phonons and hydrogen has been known to aid in the diffusion process in metal hydride systems through phonon-assisted tunneling.[58] The theory of acoustic and optical phonon-assisted tunneling/diffusion of light interstitials in metals and metal hydrides has been discussed previously.[59-62] Particles that lack the thermal energy to overcome a barrier can gain the extra energy by coupling with a phonon and subsequently jump over the barrier. With the ability for phonons to reduce the energy barrier heights, it is important to understand how the lattice dynamics change with temperature.

It is a common feature for the hydrogen atoms to be positioned on multiple, crystallographically distinct sites in metal hydride systems. Different hydrogen sites produce distinct vibrational modes, which allows INS to distinguish between the various hydrogen sites. By tracking the temperature dependence of the vibrational DOS, insight into the hydrogen release mechanism can be obtained. For example, a softening of the vibrational modes associated with that hydrogen site will begin as the hydrogen-metal bond weakens. Subsequently, the mode will decrease in intensity and merge with the background as the hydrogen is released from that site and begins diffusing. An example of this type of behavior in complex hydrides is discussed in the report by Sato et al.[63] Complex hydrides often have multi-step decomposition reactions, and temperature dependent INS is a helpful technique to uncover the decomposition reaction route. INS and total neutron scattering are often complimentary techniques since they both probe the local structure and can observe contributions from specific atomic sites.

5 SAMPLE SYNTHESIS METHODS

Metal hydrides are pyrophoric and emit hydrogen gas when exposed to water or air. Therefore, caution should be taken when handling these materials. Due to the highly reactive nature, sample handling was performed in a glove box under an inert gas atmosphere. This prevents possible contamination of the sample where hydroxide and oxide phases form upon reaction with air/water. The only commercially available material used for some of the experiments was BaH_2. The other materials were either not commercially available or were found to be of poor quality once purchased. The following is a thorough explanation of the methods used to synthesize the metal hydride materials. It should be noted that the methods used were not fully optimized for efficiency. In other words, some samples were reacted for five days, when two days may have been sufficient to complete the reaction. The goal was simply to synthesize a high-quality sample to be used in the neutron scattering experiments. As will be discussed in the following sections, all binary samples synthesized successfully, but the ternary samples were only partially successful. The ternary hydrides often had multiple phases present in the final product, which is not ideal for experiments since the hydrogen dynamics are unable to be assigned to a specific phase. Therefore, we will briefly report the synthesis methods used to produce the ternary hydrides but will not discuss them any further in the experimental results sections.

5.1 Hydrogen Storage and Thermodynamics

Hydrogen can be reversibly stored in a metal M by forming metal hydrides according to the general reaction,

$$M + \frac{x}{2} H_2 \leftrightarrow MH_x + Q \qquad (5.1)$$

where x is the hydrogen to metal ratio, MH_x is the hydride that is formed, and Q is the heat of formation. This shows that a relatively large amount of heat is generated as the hydride is formed in the exothermic reaction. On the other hand, as the hydrogen is withdrawn from the system, the reaction is endothermic and the temperature decreases.

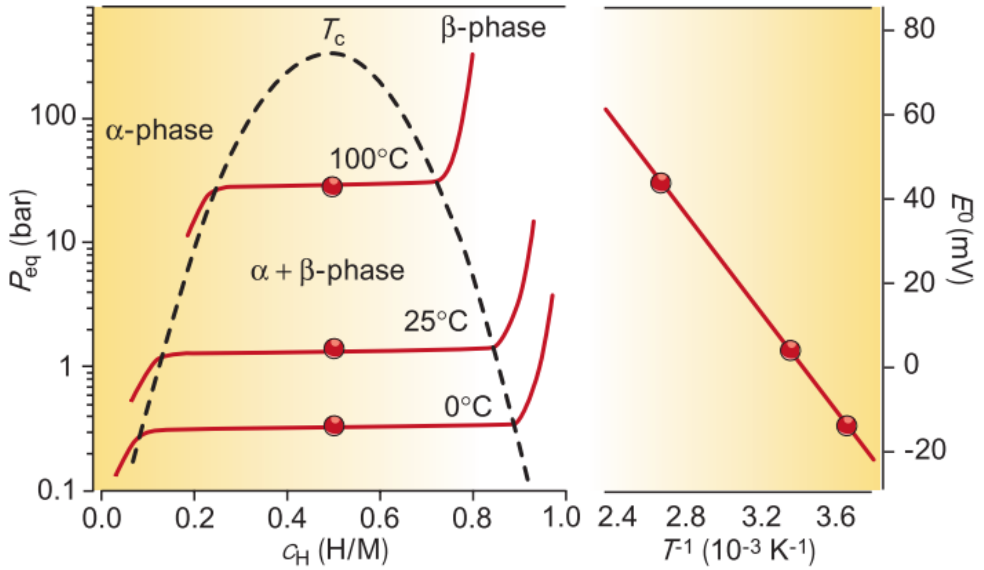

Figure 16: Van ‘t Hoff plot. The equilibrium hydrogen pressure is plotted vs. the hydrogen concentration. Likewise, the equivalent electrochemical potential is plotted vs. inverse temperature. Reprinted with permission from Schlapbach and Zuttel.[2]

The enthalpies (ΔH) and entropies (ΔS) for absorption/desorption of hydrogen are typically determined using pressure – composition – temperature (PCT) measurements using a Sievert’s apparatus.[64] When the hydrogen pressure is plotted against the concentration for various temperatures, three distinct regions emerge, as seen in Figure 16. The first region is at low hydrogen pressures where a small amount of hydrogen is absorbed and forms a solid solution, denoted as the *α*-phase. The hydrogen in the *α*-phase occupies the interstitial octahedral and tetrahedral sites in the metal host lattice. In the second region, the nucleation of the hydride phase begins, denoted as the *β*-phase, and both the *α*- and *β*-phases coexist simultaneously. In this region, the pressure plateaus as the concentration of hydrogen increases. Given enough time, the solid solution will be completely transformed into the β-hydride phase, but at a sub-stochiometric concentration. In the third region, the pressure needs to be increased once again to produce the fully hydrogenated state. A van ‘t Hoff plot can be created by plotting the equilibrium pressure in the plateau region vs. inverse temperature, as seen in Figure 16. The enthalpy of hydride formation can be determined using the slope while the entropy is yielded by the y-intercept, as given by the van ‘t Hoff equation.[2]

$$\ln\left(\frac{p_{eq}}{p_{eq}^{0}}\right) = \left(-\frac{\Delta H}{RT}\right) + \frac{\Delta S}{R} \qquad (5.2)$$

5.2 Binary Hydrides and Deuterides

This investigation focuses on binary hydrides of the form AeH_2 where Ae is a metal from the alkaline earth metal group. The chemical bonding in the alkaline earth metal group has a wide range of behaviors. The heavy alkaline earth hydrides (HAEHs) consisting of CaH_2, SrH_2, and BaH_2 form ionic compounds. However, BeH_2 forms a covalent compound and MgH_2 forms an intermediate compound that bridges the gap between ionic and covalent. These differences in bonding have immense effects on the material properties. As a result, the synthesis methods are very different between the ionic compounds of CaH_2 and BaH_2, and the covalent-like compound of MgH_2.

5.2.1 Magnesium Hydride (MgH_2 and MgD_2)

MgH_2 can be directly synthesized by reacting elemental Mg with hydrogen gas. However, the kinetics of this process are extremely slow, requiring long reaction times even when subjected extreme temperatures and hydrogen pressures. This is attributed to both the low dissociation rate of hydrogen on the Mg surface and the slow diffusion of H atoms into the bulk. Alternatively, MgH_2 can be synthesized under mild conditions using Grignard reagents or by catalytic activation.[65-67] Both methods were tested, with the catalytic method producing the best results. For this reason, only the catalytic method will be explained below.

Transition metals are highly effective catalysts for use in the synthesis of MgH_2. We followed the general procedure previously reported by Bogdanović et al.[67] This method uses the organic compound, anthracene, in combination with transition metal halides in a tetrahydrofuran (THF) solution. Chromium, titanium, or iron halides were recommended for the transition metal catalyst. For our synthesis, we tried both molybdenum pentachloride ($MoCl_5$) and chromium trichloride ($CrCl_3$), with $MoCl_5$ yielding the best result. Bogdanović also reports that polycyclic arenes or amines may be added to enhance the activation. We found that 1-bromopropane works better than their recommendation of ethyl bromide. The best result was a product of the following procedure:

Under an argon atmosphere, 6.1 g Mg (Alfa Aesar, -325 mesh powder, 99.8%) was added to a boiling flask containing 30 mL anhydrous THF and 90 µL 1-bromopropane, along with a magnetic stirring rod. This was stirred for 30 minutes at room temperature followed by the addition of 0.45 g anthracene, which was then stirred for 2 hours at 60°C and then cooled. Next, 0.7 g anhydrous $MoCl_5$ was added and stirred at room temperatures for 30 min. The solution was left stirring overnight at this step, which is not necessary since the slightly exothermic reaction is completed after approximately 15-30 min. The solution is then transferred to an autoclave containing a magnetic stirring rod. The solution is hydrogenated at a temperature of 80°C and a hydrogen pressure of 80 bar. Bogdanović reports that the Mg is fully converted to MgH_2 after approximately 14 hours. We used longer reaction times of 24 hours or longer (over the weekend) to ensure that the sample has been completely converted to MgH_2. Upon completion, the solution was filtered using a 150 mL coarse filter (C, pore size 25-50 µm). The light grey powder was rinsed with THF three times followed by a thorough rinse with n-pentane to remove the THF. The powder was then dried with a vacuum at room temperature. This produced high purity MgH_2 with a yield of 5.8 grams. Some additional MgH_2 could potentially be recovered by filtering an additional time with a finer filter.

The deuterated samples were synthesized following the same procedure with deuterium gas. Following an experiment at NOMAD, protium (not deuterium) was observed in the MgD_2 sample. This was observed as a large incoherent background in the diffraction pattern. Fourier-transform infrared spectroscopy (FTIR), INS, and XRD measurements were performed to determine the source of the protium. These results suggested that protonated solvents and/or anthracene remained in the sample, even after filtering with THF and pentane under vacuum. The sample was heated up to 145ºC for a day in a quartz tube to extract the remaining solvent from the sample. A yellowish-green film was evaporated and deposited on the wall of the quartz tube. FTIR of this film suggested that it was anthracene and another unknown compound. A subsequent NOMAD experiment on this heat-treated sample still showed signs of protium. The sample was subsequently heated at 120ºC for 9 days under vacuum. FTIR measurements showed that most of the protium was removed from the sample. However, additional PDF measurements on this sample still showed the presence of protium. It also appeared that the extreme heating treatment had altered the sample, which is described more in Section 8.1.1.

5.2.2 Barium Hydride (BaH_2 and BaD_2)

Commercially available barium hydride powder was purchased from American Elements with a reported purity of 99.7% metals basis, which was verified using XRD. In contrast to MgH_2, BaH_2 can be easily formed by a direct reaction between elemental Ba and H_2 gas. However, Ba powder is difficult to make and is generally not available commercially.

For the BaD_2 synthesis, a large chunk of Ba metal was cut into smaller pieces and ball milled to create a powder. A combination of 2 mm and 5 mm stainless steel balls were added to an air-tight stainless steel vessel. Ba metal of approximately 1/5 the weight of the steel balls was added to the vessel. This was cooled using liquid nitrogen and ball milled for 15 minutes. Subsequently, it was cooled for another 15 minutes in liquid nitrogen before a 30-minute balling procedure. After warming to room temperature, the material was ball milled for an additional 30 minutes. This entire ball milling procedure was repeated a second time. Due to the rather ductile nature of Ba, the ball milling efforts were only partially successful. A small amount of powder was produced, but most of the Ba formed balls of a few millimeters in diameter. Approximately 6 grams of ball-milled Ba were placed inside an autoclave and sealed in a glovebox. The autoclave was heated to 180ºC and subjected to a pressure of 27 bar D_2 gas. The reaction was performed for 24 hours. The product was light grey in color and reactive to water. Approximately 1.4 g of powder was generated along with 4.7 g of reacted BaD_2 chunks. The chunks were then crushed into a powder using a mortar and pestle to yield 5.5 g of powder. The remaining mass was unreacted Ba metal, which was removed. This produced high purity BaD_2.

Additional batches of BaH_2 and BaD_2 were synthesized using custom ordered Ba beads of particle size 0.5 – 2.0 mm from Sigma Aldrich with a purity of 99% (trace metals basis). Ba was reacted in an autoclave for 24 hours at $P = 50$ bar of H_2 (D_2). Following the reaction, the beads were changed from silver in color to a series of colors ranging from purple to gray to white. The beads were easily crushed into a powder using a mortar and pestle. The range in colors are likely due to defects in the material. XRD measurements showed only BaH_2 (BaD_2) peaks. Ba has a strong affinity for oxygen and will slowly convert to BaO over time if the helium glovebox has small concentrations of oxygen present.

5.2.3 Calcium Hydride (CaH_2 and CaD_2)

Commercially available calcium hydride powder was purchased from Sigma-Aldrich with a reported purity of 99.99% metals basis. However, XRD measurements showed that the sample had significant levels of contamination present, as indicated by the observation of multiple unknown phases. Therefore, we proceeded with synthesizing a purer sample of calcium hydride and deuteride.

5 g of calcium powder (Alfa Aesar, -16 mesh granules, 99.5%) was reacted directly with H_2 gas in a Parr autoclave. This was heated to 350ºC where it was reacted with 7 bars of H_2. The pressure immediately dropped to about 0 bar and this cycle was repeated approximately five times before the pressure stabilized.

Calcium hydride is known to “cake up” and form a solid ball if reacted with hydrogen too quickly. Therefore, we attempted to avoid this by reacting the surface of the powder slowly at the lower temperature of 350ºC. After this, the sample was heated to 450ºC and reacted with 10 bar of H_2 overnight (approx. 15 hours). The pressure did not drop overnight which suggests that the reaction had been completed during the hydrogenation step at 350 ºC. The sample produced was still “caked up” and formed a large ball. This was crushed up with a mortar and pestle and x-rayed. This revealed that some additional Ca metal remained unreacted but that CaH_2 was produced. The powder was reacted a second time in the autoclave at 480ºC and 150 psi for 1.5 days. During this time, the pressure decreased to 115 psi indicating that a reaction occurred. The product was a fine white powder. XRD suggests that a very small amount of Ca metal is still present.

5.3 Ternary Hydrides and Deuterides

In addition to the binary hydrides, two different ternary hydrides consisting of alkaline earth metals were synthesized: dibarium magnesium hexahydride and tetracalcium trimagnesium tetradecahydride. These materials have largely not been studied, except for a limited amount of investigations reporting the synthesis methods and structural characterization.[19, 20] Alloying the HAEHs with lighter weight cations, such as Mg, could be an interesting method to increase the gravimetric storage densities while maintaining the desirable hydrogen transport properties provided by the HAEHs.

5.3.1 Dibarium Magnesium Hexahydride (Ba_2MgH_6 and Ba_2MgD_6)

Ba_2MgH_6 and Ba_2MgD_6 were first synthesized and reported by Kadir and Noréus.[19] The synthesis was performed by pressing a 0.15 g pellet of a 2:1 stoichiometric mixture of BaH_2 and MgH_2 and reacted in an H_2 (D_2) atmosphere at P = 70 bar and T = 480ºC for 6 days. Following this procedure but scaling it up to a 1.094 g pellet and reacting at a pressure of 50 bar, we observed only a small amount of Ba_2MgH_6 that was formed. The remaining phases consisted of BaH_2 and MgH_2. The pellet was grinded, repressed, and reacted again under the same conditions. However, the Ba_2MgH_6 phase completely disappeared. It is possible that a higher pressure of 70 bar and smaller sample masses are needed to produce Ba_2MgH_6 through this method. However, there were no diffraction patterns included in the report by Kadir et al. so it is impossible to determine if a pure Ba_2MgH_6 sample was synthesized using their method. As with many of the ternary alkaline earth hydrides, pure samples are difficult to synthesis and typically they exist in equilibrium with multiple phases.[20, 68-72]

Instead of pressing a pellet of the respective hydrides, an alloy of Ba_2Mg was formed by melting a 2:1 ratio of Ba beads (0.5 mm to 2 mm diameter) and Mg powder (-325 mesh) in an alumina crucible under an argon atmosphere. The sample was heated to 630ºC for one hour and then cooled below the eutectic point (358ºC) reported in the Ba-Mg phase diagram.[73] The sample was then cycled up to 400ºC and then cooled below the eutectic point three times to ensure mixing. The alumina crucible containing the alloy was transferred to an autoclave and reacted at 400ºC and 95 bar for 18 hours. A two phase mixture of Ba_2MgH_6 and BaH_2 was confirmed using XRD. The powder was yellowish-green and white in color. Various reaction times were tested, with the general trend of creating less of the Ba_2MgH_6 phase and more of BaH_2, MgH_2, and $BaMgH_4$ with longer reaction times.

5.3.2 Tetracalcium Trimagnesium Tetradecahydride ($Ca_4Mg_3H_{14}$ and $Ca_4Mg_3D_{14}$)

$Ca_4Mg_3H_{14}$ and $Ca_4Mg_3D_{14}$ were first synthesized by Gingl et al.[20] As in the case of Ba_2MgH_6, attempts were made to synthesize the ternary compound from mixtures of their hydride counterparts (CaH_2 and MgH_2). However, this method produced many impurity phases. Hence, an alloy was formed instead by melting a 1:1 mixture of Ca and Mg to form a two-phase mixture of $CaMg_2$ and Ca. The alloy was reacted under H_2 at P = 55 bar and T = 420ºC for 6 days. XRD showed that a significant amount of $Ca_4Mg_3H_{14}$ was formed, but MgH_2, CaH_2, and Mg are also present in small amounts.

The difficulty in synthesizing $Ca_4Mg_3H_{14}$ from an alloy of Ca and Mg is that Ca_4Mg_3 is not a phase that exists on the Ca-Mg phase diagram.[74] Gingl et al. attempted to synthesis the sample using a 1:1 mixture of Ca and Mg which will inherently produce a multi-phase sample. We melted a 4:3 stoichiometric ratio of Ca and Mg (5 g total mass) was melted at 680ºC in a helium atmosphere for approximately 12 hours and cooled to room temperature. This process was cycled three times to ensure adequate mixing. XRD of the alloy showed mostly Mg_2Ca, with Ca and CaO present in small amounts. The alloy was reacted in an autoclave for 10 days at 420ºC and 55 bar H_2. XRD showed $Ca_4Mg_3H_{14}$ present in large amounts with small amounts of MgH_2 and Mg present.

6 BARIUM HYDRIDE

The main focus of this work is to investigate the structure and dynamics of BaH_2. This material is important to study because it exhibits unique hydrogen transport properties, i.e. fast ionic conduction of hydride ions. Both temperature and pressure are known to cause a phase transition which influences the hydrogen transport properties. First, the temperature dependence of the local and global crystal structure and hydrogen dynamics will be discussed, followed by the pressure dependence.

6.1 Temperature Dependence

6.1.1 Crystal Structure

The crystal structure of barium hydride has been well studied.[13, 49, 75-77] Two distinct phases are observed upon heating from room temperature: (1) low-temperature orthorhombic phase and (2) a high-temperature hexagonal phase. The cell parameters and special fractional coordinates for both phases are listed in Table 4.[13] The hydrogen (specifically deuterium for our structural studies) in both phases reside on two crystallographically distinct sites, referred to as D(1) and D(2). In addition, the HAEH group has been reported to have significant hydrogen substoichiometries, with x~1.8 for BaD_x.[13, 17] A large concentration of vacancies can be beneficial for hydrogen diffusion.

At ambient conditions, BaD_2 crystallizes in the cotunnite structure with orthorhombic symmetry (space group Pnma (62)). Lattice parameters for BaD_2 are a = 6.7824 Å, b = 4.1605 Å, and c = 7.8432 Å at T = 298 K.[13] For the orthorhombic phase, Ba, D(1) and D(2) are all positioned on 4c sites (x. ¼, z). A structural phase transition occurring around 775 K transforms the orthorhombic phase into a high symmetry hexagonal phase (Ni_2In-type, space group $P6_3/mmc$ (194)).[13, 75] The hexagonal unit cell has lattice parameters of a = 4.457 Å and c = 6.723 Å at T = 883 K.[13] Previous NPD measurements have suggested that the D(1) site is split.

Rather than residing on the high symmetry 2d sites, the deuterium is slightly shifted to the lower symmetry 4f sites.

Table 4. Refined lattice parameters and atomic coordinates for both phases of BaD_2 from NPD measurements, as reported by Verbraeken et al.[13]

Phase Parameters	T = 298K	Phase Parameters	T = 883 K D1 on 4f	Phase Parameters	T = 883 K D1 on 2d
a (Å)	6.7824(1)		4.4571(2)		4.4566(2)
b (Å)	4.1605(1)		4.4571(2)		4.4566(2)
c (Å)	7.8432(1)		6.7230(4)		6.7219(5)
Ba, 4c	(x, 1/4, z)	Ba, 2b	(1/3, 2/3, 1/4)	Ba, 2b	(1/3, 2/3, 1/4)
x	0.2393(3)				
z	0.1112(2)				
D1, 4c	(x, 1/4, z)	D1, 4f	(1/3, 2/3, z)	D1, 2d	(1/3, 2/3, 3/4)
x	0.3514(2)				
z	0.4282(2)		0.8288(5)		
D2, 4c	(x, 1/4, z)	D2, 2a	(0, 0, 0)	D2, 2a	(0, 0, 0)
x	0.9733(2)				
z	0.6828(2)				

The cotunnite to Ni_2In-type phase transition has been known to occur in many types of materials, such as the fluorite-type compounds and Na_2S.[78, 79] The cotunnite and Ni_2In-type phases are similar structurally. Comparisons between these two structures have been described in detail previously.[49, 78, 79] Briefly, the cations in the cotunnite phase are positioned on a slightly distorted hexagonal close packed (hcp) lattice. Despite the hexagonal arrangement, the unit cell is properly described using an orthorhombic symmetry. In both phases, six anions surround the cation forming a trigonal prism. In the cotunnite structure, three additional anions surround the cation (coordination number (CN) = 9) while five additional anions are surround the cations (CN = 11) in the Ni_2In-type structure. The disorder in the cation positions in the cotunnite structure causes the adjacent anionic prisms to be tilted 25° with respect to each other. Following the phase transition, the cations become properly aligned on the hcp sites and the tilt is removed, resulting in a higher symmetry hexagonal phase. This structure consists of alternating layers of Ba with D(1) and layers of D(2) alone. Both crystal structures are displayed in Figure 17.

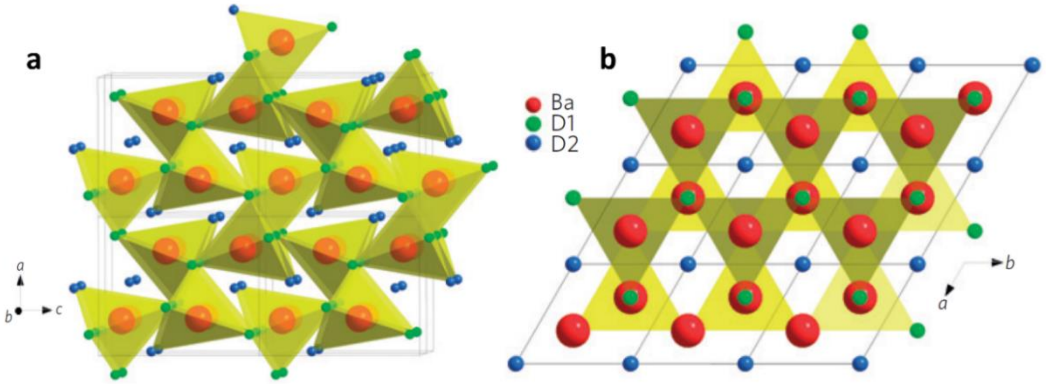

Figure 17: Crystal structures of BaD_2. (a) Orthorhombic (cotunnite) structure at *T* = 298 K and (b) hexagonal (Ni_2In-type) structure at *T* = 883 K. Reprinted with permission from Verbraeken et al.[13]

6.1.2 Total Neutron Scattering and Diffraction

Total neutron scattering measurements were performed at NOMAD on BaD_2 from *T* = 300 K – 900 K, with the PDFs displayed in Figure 18. The experimental data is well described by the cotunnite structure across the local and global regions (*r* = 1.5 – 35 Å in this case) up to the phase transition. Minor deviations can be observed, mostly in the local structure. The pattern begins with a broad peak located between *r* = 2.6 Å – 3.3 Å, which is a superposition of many different atomic distances of type Ba-D and D-D. The shortest Ba-Ba distances begin around 4.03 Å. As expected with increasing temperature, the sharp peaks at 300 K gradually become more smeared out and weaken in intensity due to the Debye-Waller effect. A more detailed look at the temperature dependence of the local vs. global regions is shown in Figure 19. The pattern can be divided into three distinct regions: (1) the local structure up to roughly 6 Å, (2) a transition region between 6 Å – 13 Å, and (3) the global structure above 13 Å. As the temperature is increased, the local structure remains largely unchanged. The length scales for this region roughly corresponds to the size of one unit cell of BaD_2. On the other hand, drastic changes can be observed beginning around 775 K in the intermediate transition region between 6 Å – 13 Å, which is due to the orthorhombic to hexagonal phase transition. The sharp peaks become significantly smeared out by the 825 K measurement, indicating that this region is rather disordered. Further explanation of the transition region will follow shortly. The global structure is located above r = 13 Å, which is observed as a series of sharp peaks at 300 K. As temperature increases, the numerous peaks merge into a lesser series of broad peaks with considerable intensity, i.e. four main peaks located between 13 Å – 22 Å. The reduction in peaks can be viewed as a transition to a higher symmetry phase, which is indeed what happens in the cotunnite to Ni_2In-type transition.

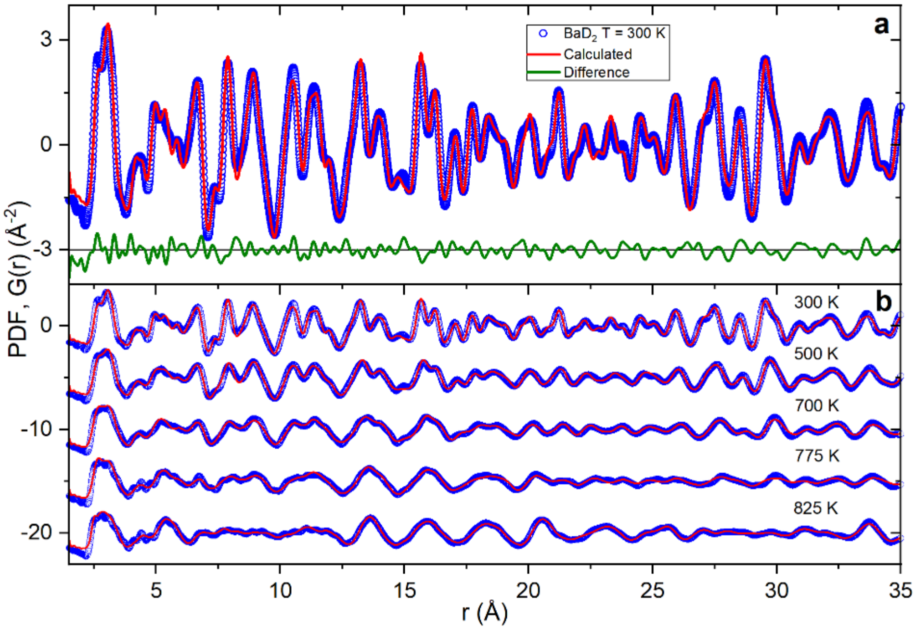

Figure 18: PDF $G(r)$ vs. r showing the local and global structure for BaD_2 at (a) 300 K and (b) 300K – 900 K ($G(r)$ are translated). The calculated model uses the orthorhombic cotunnite structure.

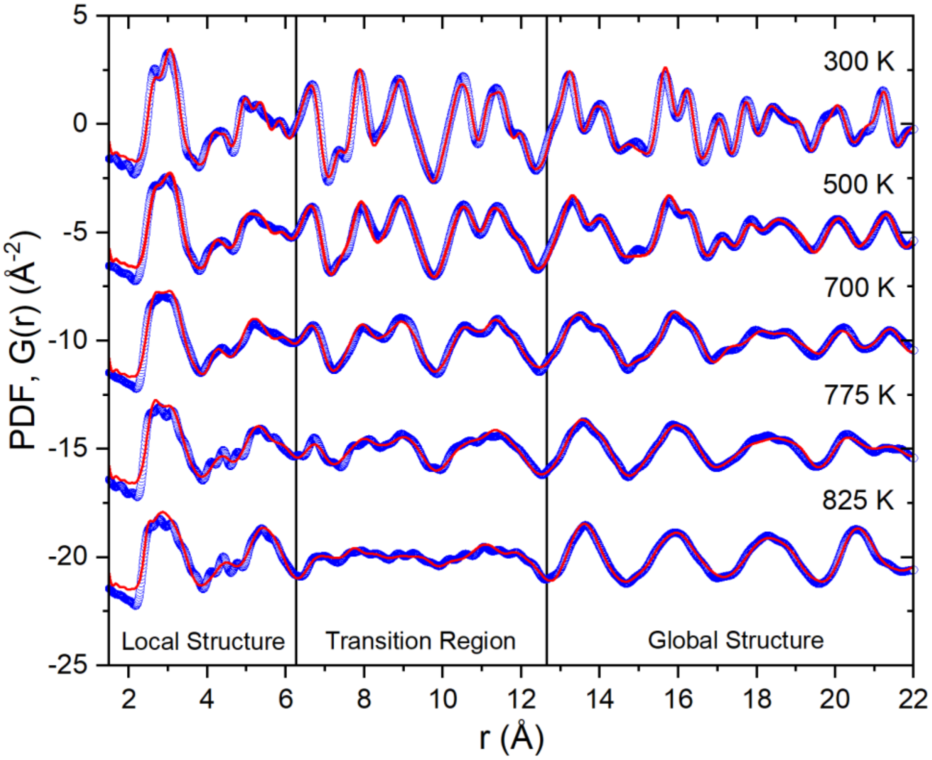

Figure 19: PDF *G(r)* vs. *r* for BaD_2 at *T* = 300K – 900 K (*G(r)* are translated). The calculated model uses the orthorhombic cotunnite structure.

The structural phase transition has been reported to be of first order in nature, but arguments can be made for it to be of second-order.[13] For one, the structural change only involves minor changes in the unit cell parameters and atomic coordinates. It is basically a slight rearrangement of the atomic positions to produce the proper hcp structure. However, Verbraeken et al. argues that the volume contraction at the transition temperature causes a large enough discontinuity in the cell volume vs. temperature to be considered first-order. Our NPD measurements show that the phase transition occurs slowly, with both phases coexisting simultaneously over a large temperature range. This can be observed in the temperature evolution of the orthorhombic (112) and (210) peaks from our NPD measurements in Figure 20. The phase transition begins around 775 K and is not completed until somewhere between 850 K – 900 K.

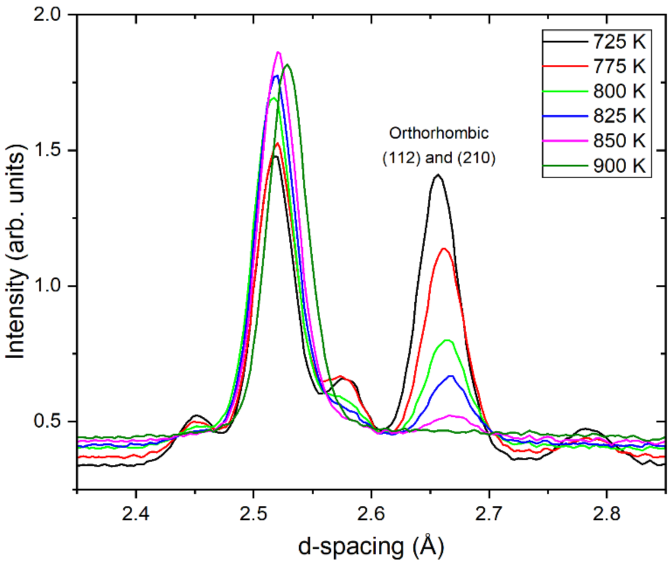

Figure 20: NPD pattern for BaD_2 measured at NOMAD for temperatures between 725 K – 900 K. The orthorhombic to hexagonal phase transition can be observed by the extinction of the orthorhombic (112) and (210) peaks around d = 2.66 Å.

Lattice parameters and anisotropic atomic displacement parameters (U) extracted from PDF analysis are displayed in Figure 20. The lattice parameters show a clear change around 775 K that indicates the onset of the structural phase transition. This type of transition should have the following relation: $a_{ortho} = c_{hex}$ *and* $b_{ortho} = a_{hex}$.[13] Previous NPD results report the hexagonal lattice parameters at T = 883 K to be a = 4.4571(2) Å and c = 6.7230(4) Å.[13] Using the orthorhombic cotunnite structure at 825 K, the lattice parameters (converted into the corresponding hexagonal lattice parameters) were determined to be a = 4.42(1) Å and c = 6.68(1) Å. Therefore, the relation is satisfied since the orthorhombic lattice parameters have deviated from the orthorhombic values and are approaching the expected hexagonal values. Initially, it is surprising to observe how well the cotunnite structure describes the data at 825 K (Figure 19), especially considering that this measurement is 50 K over the reported transition temperature. For one, this may be due to some of the orthorhombic phase remaining in the sample. The more likely reason is that the theoretical orthorhombic structural model has been modified during the PDF analysis process as it begins to converge on the proper hexagonal structure. Again, both structures are very similar and only involves minor changes in the lattice parameters and atomic positions. The atomic displacement parameters in Figure 21 show that both D(1) and D(2) are behaving in a similar manner in the orthorhombic phase. Note, the deuterium site fractional occupancies were fixed in the cotunnite structure at 0.877843 and 0.857965 for D(1) and D(2), respectively. These values were determined in the 300 K measurement and fixed for the subsequent measurements. Refining these values with temperature was attempted but led to unreliable results. Figure 22 shows the temperature dependence of the special atomic coordinates for the 4c sites of Ba, D(1), and D(2). Changes can be seen in all the atomic positions at temperatures well below the phase transition, with the most significant changes occurring in Ba and D(2). The D(1) sites appear to be more stable until a drastic change occurs at 775 K.

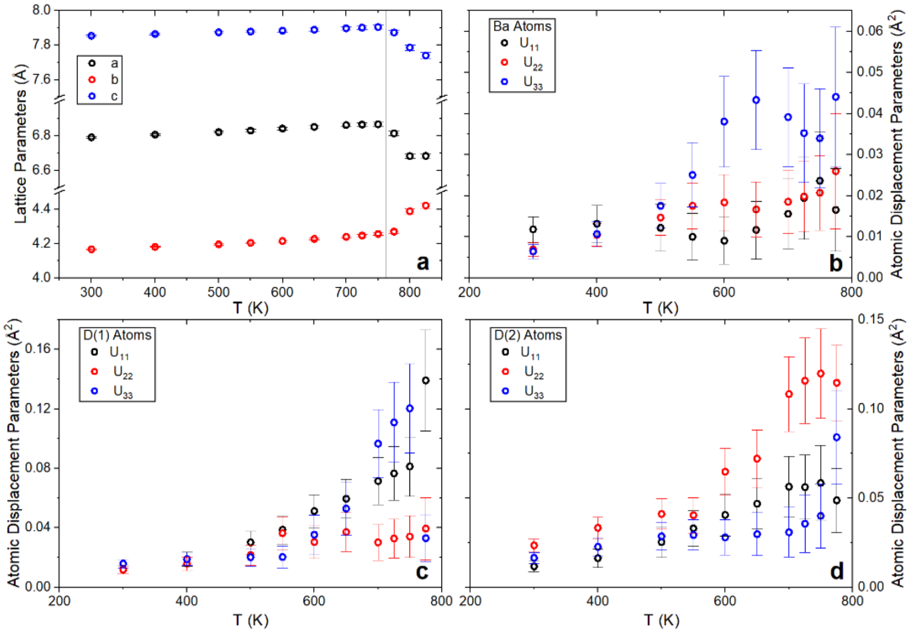

Figure 21: Refined parameters from PDF analysis for BaD$_2$ with the cotunnite structure. (a) Lattice parameters and atomic displacement parameters (*U*) for (b) Ba, (c) D(1), and (d) D(2) atomic sites.

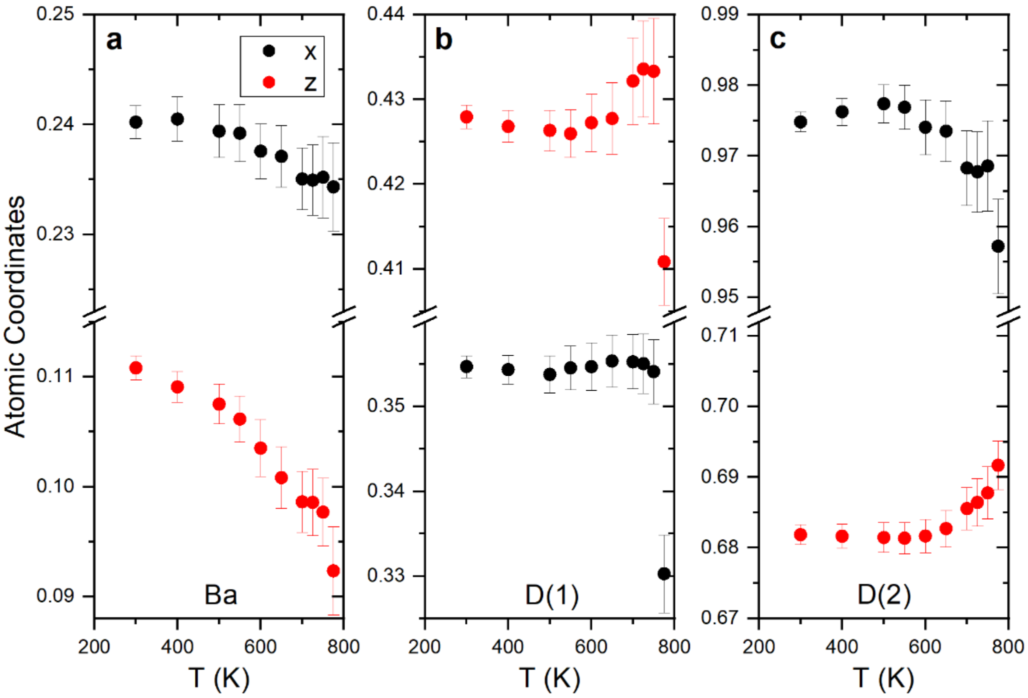

Figure 22: Refined special atomic coordinates *x* and *z* for the (a) Ba, (b) D(1), and (c) D(2).

Accurate modeling of PDF patterns in the two-phase region between 775 K and 850 K was difficult due to the similarity of the two crystal structures and many refinable parameters. Therefore, the 900 K measurement was used for accurate modeling of the hexagonal Ni_2In-type structure since the orthorhombic phase no longer exists. As mentioned previously, the D(1) site has been reported to be split in this structure for BaD_2.[13] Rather than residing on the high-symmetry 2d site, D(1) is instead positioned on the lower symmetry 4f site. Figure 23 shows a comparison of *G(r)* at 900 K fit with calculated models for D(1) positioned on the 2d and 4f sites. Both models are clearly very similar, but the split-site model does provide a slightly better fit to the observed data. The R_w values are 0.2717 and 0.2495 for D(1) positioned on the 2d (non-split) sites and the 4f (split) sites, respectively. The site splitting occurs along the *c*-axis in the structure. Justification for the split site can be observed in the atomic displacement along this axis, where U_{33} = 0.445 Å^2

for the non-split site model. This is a very large atomic displacement parameter, which suggests that the D(1) atoms are highly mobile along the z-axis. It is a common practice in crystallography to model an atomic site with large displacements as a split site. Using the 4f (split) site model, U_{33} assumes a more reasonable value of 0.125 Å^2. The distance between the split D(1) sites was determined to be 1.014 Å at 900 K.

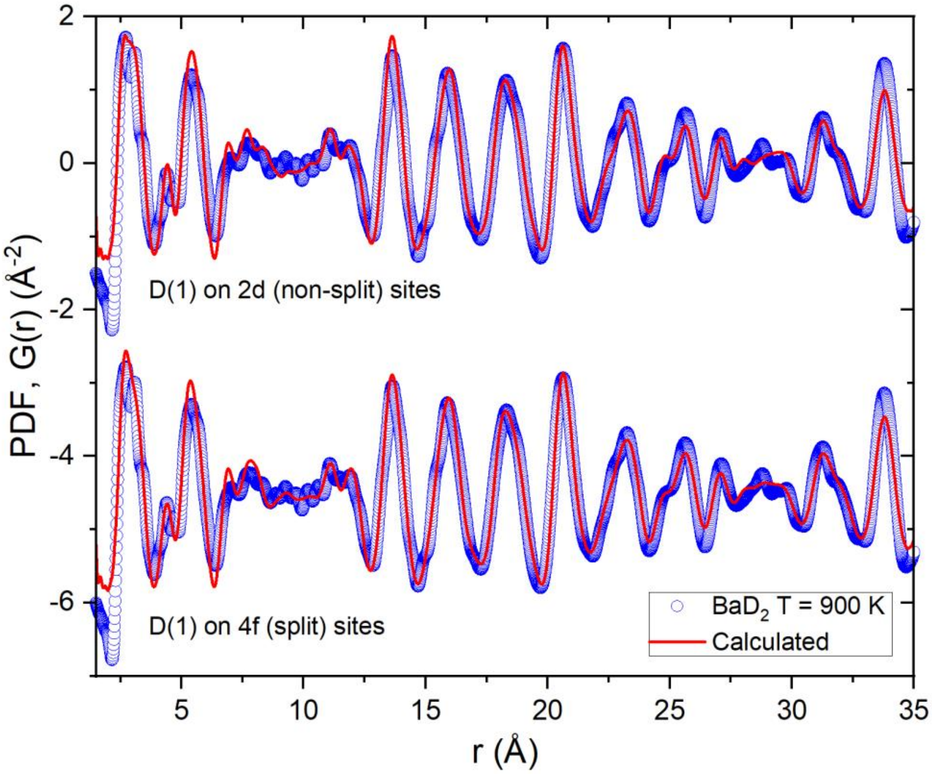

Figure 23: Comparison of *G(r)* for BaD_2 at 900 K fit with models containing D(1) positioned on 2d (non-split) sites and 4f (split) sites. *G(r)* are translated for clarity.

We are now ready to elaborate on the origin of the intermediate transition region observed in Figure 19. As mentioned in previously, the slight disorder in the Ba positions causes the anionic polyhedra in the cotunnite phase to be slightly tilted with respect to each other. This tilt is largely frozen in place in the orthorhombic structure but is removed in the hexagonal structure. While the long range, time-averaged structure determined from Rietveld refinements would suggest the tilt no longer remains, the PDF results suggest that the anionic polyhedra in the hexagonal phase have some degree of reorientational freedom. The local structure (< 6 Å) resembles the unit cell of BaD_2, which has largely maintained the same local structure through the phase transition. But rather than the neighboring anionic polyhedral being tilted at 25º with respect to each other, it can be argued they can now assume various tilted configurations. This type of dynamic fluctuation would allow the local structure to remain the same but produces a disordered region that bridges the gap between the local and global structure (Figure 19). Over the distance of roughly 2 to 3 unit cells, these correlated motions are averaged-out to yield the high symmetry hexagonal structure. In other words, the PDF measurements have shown that the hexagonal structure can be considered a short-range dynamic mosaic of the orthorhombic phase.

These dynamic structural fluctuations also provide further explanation for the existence of the split H(1) site and would be beneficial to the diffusion process by shortening the hydrogen jump length. In addition, cooperative rearrangements of the lattice can help aid in diffusion by increasing the free volume for the hydrogen to diffuse through. This motion can modify the energy landscape and reduce the energy barriers for diffusion. Anionic reorientational motion has been reported in complex hydrides, which serves to unlock fast ionic diffusion of cations in these materials.[80-82] These results have interesting ramifications for the lighter weight HAEHs of CaH_2 and SrH_2 because they possess the same cotunnite structure as BaH_2. However, neither CaH_2 or SrH_2 exhibit a temperature induced cotunnite to Ni_2In-type phase transition (an unidentified phase transition occurs in SrH_2 around 850°C)[83], but a pressure induced transition of this type has been previously observed.[84-86] Therefore, it could be possible to induce this type of phase transition through doping or other techniques. This could potentially unlock fast hydrogen diffusion in the lighter weight hydrides that would have more suitable hydrogen storage densities for applications.

6.2 Hydrogen Diffusion: Quasielastic Neutron Scattering

As mentioned previously, BaH_2 exhibits fast ionic conduction of hydride ions at elevated temperatures. The ionic conduction is modest in the orthorhombic phase, but the diffusion increases by over an order of magnitude following the phase transition. The best available technique to study this diffusive motion on the atomic scale is quasielastic neutron scattering. We investigate the diffusion process in both phases of BaH_2 to understand what changes in the diffusion pathways to unlock the faster motion.

First, we conducted an elastic scan at BASIS to obtain a general understanding of what temperature range the observable hydrogen dynamics are expected to occur on the timescale of the instrument. The elastic san was performed up to a maximum temperature of 880 K, as shown in Figure 24. By examining the slope of the elastic intensity vs. temperature, three distinct regions were observed: (1) low-T region (from 300 K up to about 650 K), (2) intermediate-T region (from about 650 K up to about 775 K), (3) and the high-T region (T > 775 K). The low-T region has a gradual decrease and resembles a typical Debye-Waller type behavior. Beginning around 650 K, the elastic intensity begins to decrease more rapidly. A decrease in the elastic intensity is an indication of the onset of observable hydrogen dynamics. Therefore, a quasielastic signal should be observable beginning around 650 K. The third region begins with a sudden decrease in the elastic intensity around 775 K, corresponding to the phase transition. After the phase transition, the elastic intensity flattens out to a very small value, suggesting that the hydrogen in the structure has become highly mobile. The following sections will demonstrate that the hydride ions have very distinct dynamics in these three different temperature regions.

Following the results from the elastic scan, longer QENS measurements were performed to carry out enable a detailed QENS data analysis. The data analysis methods for these measurements has been outlined in Chapter 4. Quasielastic broadening is first observed in the QENS spectra at 600 K. However, the combination of a very weak intensity and narrow broadening makes the quasielastic signal unable to be fit reliably below 670K at both spectrometers (BASIS and HFBS). This temperature perfectly corresponds to the intermediate-T region in the elastic scan, where the elastic intensity indicated the onset of observable hydrogen dynamics. Upon the phase transition at 775 K, the quasielastic component increases drastically in both intensity and width. The QENS spectra measured at BASIS is shown in Figure 25a for 710 K (orthorhombic phase) and Figure 25b for 850 K (hexagonal phase). Measurements were conducted using the Si(111) analyzers (smaller energy range, ±100 µeV) for the orthorhombic phase while Si(311) analyzers (larger energy range, ±740 µeV) were used for the hexagonal phase in order to observe the full spectral broadening.

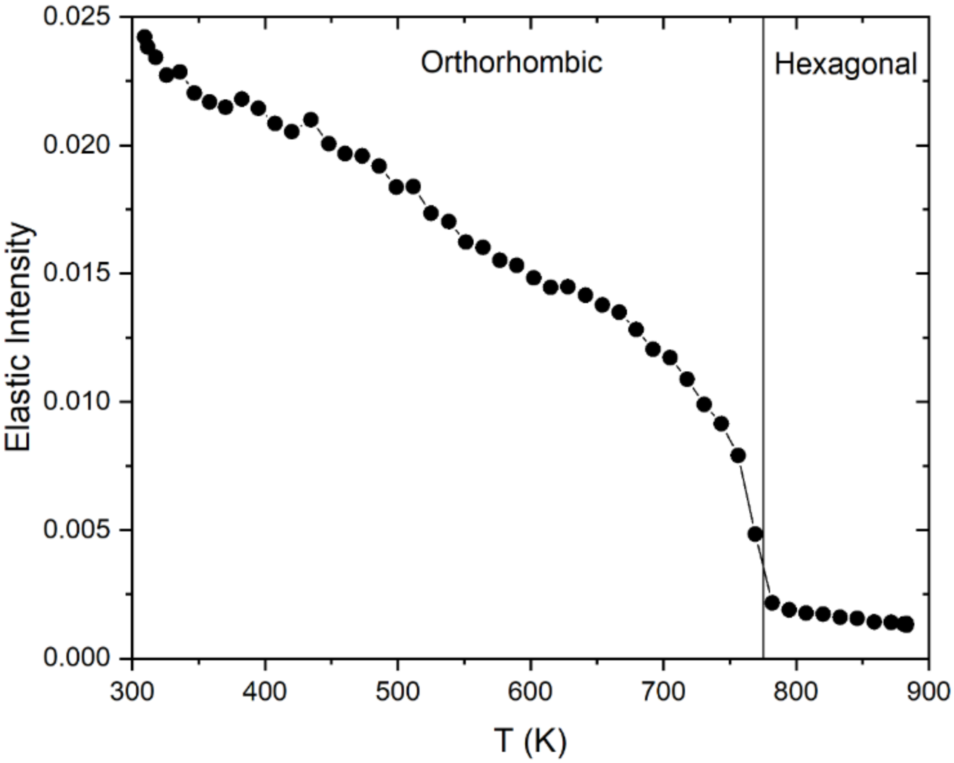

Figure 24: Elastic intensity scan measured at BASIS. The data is averaged over a Q-range of 0.5 – 1.5 Å^{-1}.

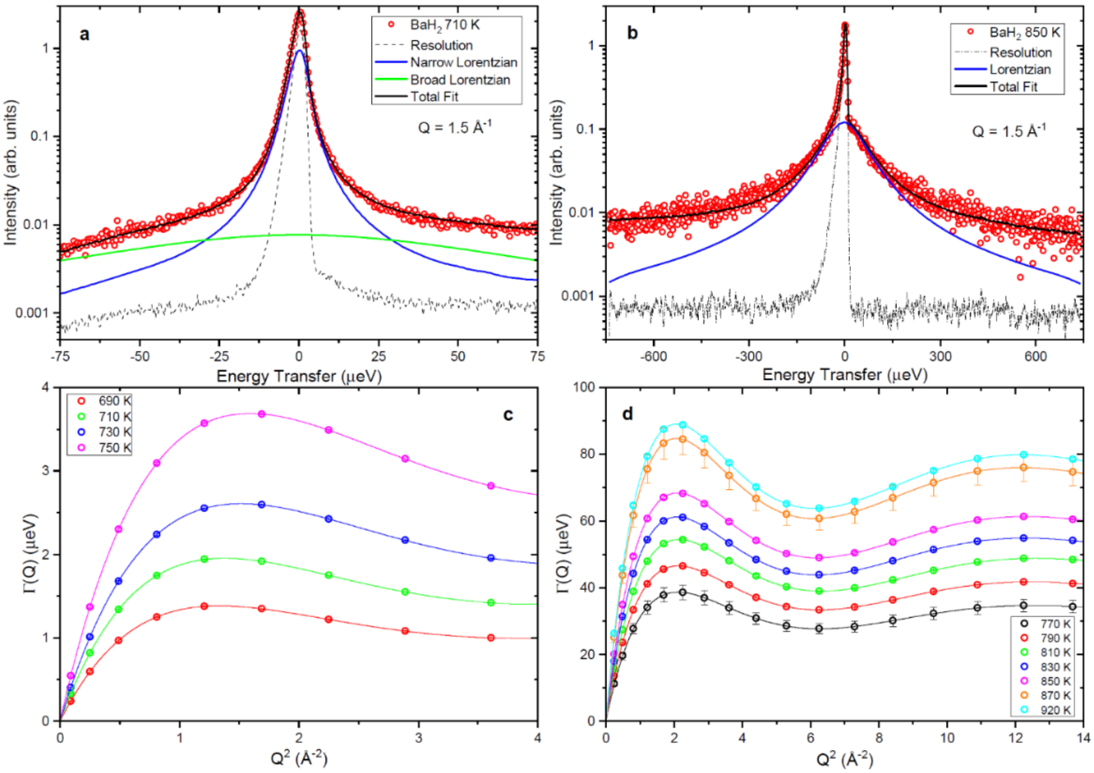

Figure 25: QENS spectra measured at BASIS at Q = 1.5 Å^{-1} at (a) T = 710 K and (b) T = 850 K with the fit components shown. HWHM Γ(Q) vs. Q^2 of the Lorentzian in the (c) low temperature orthorhombic phase and (d) the high temperature hexagonal phase measured at BASIS. The solid lines are fits of the Chudley-Elliott jump diffusion model.

The QENS spectra were first fit using an unconstrained model with Lorentzian functions representing the quasielastic signal (Eq. (4.1) with the quasielastic term given by Eq. (4.2)). The orthorhombic phase is reproduced with two Lorentzian functions while only one Lorentzian function was needed for the hexagonal phase. Despite the use of two Lorentzian functions for the orthorhombic phase, there is only one distinct dynamical process arising from the sample. The dynamic process is evident as a narrow Lorentzian with a HWHM on the order of a few µeV. The second Lorentzian is very broad, on the order of tens to hundreds of µeV, with no Q-dependence. This signal is likely an artifact of the instrumental background. Proof that this signal does not originate from the sample is that the broad component is only present in the data using the Si(111) analyzers and disappears after switching to the Si(311) analyzers. If this broad component truly was originating from the sample, it should be easily observable using the Si(311) analyzers.

Table 5: Jump lengths, residence times, and diffusion coefficients for the QENS fitting results of BaH_2.

Orthogonal Phase	**T (K)**	**L (Å)**	**τ (ns)**	**D (10^{-7} cm^2/s)**
HFBS CCR	670	4.2 ± 0.2	1.7 ± 0.08	1.7 ± 0.2
	720	4.1 ± 0.1	1.0 ± 0.03	2.7 ± 0.2
	750	4.0 ± 0.1	0.7 ± 0.02	3.8 ± 0.2
BASIS Si(111) CCR	670	3.7 ± 0.1	0.8 ± 0.02	2.9 ± 0.1
	690	4.1 ± 0.1	0.7 ± 0.01	3.9 ± 0.2
BASIS Si(111) Furnace	690	3.9 ± 0.02	0.6 ± 0.002	4.4 ± 0.04
	710	3.8 ± 0.01	0.4 ± 0.001	6.0 ± 0.03
	730	3.7 ± 0.01	0.3 ± 0.0008	7.2 ± 0.04
	750	3.6 ± 0.01	0.2 ± 0.0004	9.7 ± 0.05
Hexagonal Phase	**T (K)**	**L (Å)**	**τ (ps)**	**D (10^{-5} cm^2/s)**
BASIS Si(111) Furnace	770	3.0 ± 0.03	18.5 ± 0.2	0.8 ± 0.02
BASIS Si(311) Furnace	770	3.1 ± 0.02	20.7 ± 0.1	0.8 ± 0.009
	790	3.1 ± 0.01	17.2 ± 0.07	0.9 ± 0.006
	810	3.1 ± 0.01	14.7 ± 0.06	1.1 ± 0.008
	830	3.1 ± 0.01	13.1 ± 0.04	1.2 ± 0.006
	850	3.1 ± 0.01	11.7 ± 0.05	1.4 ± 0.01
	870	3.1 ± 0.03	9.5 ± 0.07	1.7 ± 0.03
	920	3.1 ± 0.01	9.0 ± 0.04	1.8 ± 0.01

The Lorentzian widths in the unconstrained fits showed a clear Chudley-Elliott diffusive behavior.[41, 42] Other models, such as Singwi-Sjölander[43] and Hall-Ross,[44] were tested as well but could not reproduce the experimental data with similar quality as the Chudley-Elliott model.[41, 42] An example of the three jump diffusion models for the data at T = 850 K was shown in Figure 10 in Chapter 4. Therefore, the Lorentzian widths (quasielastic broadening) was further constrained to follow the Chudley-Elliott model as a function of Q, as explained in Section 4.1.3.1. The resulting constrained HWHM ($\Gamma(Q)$) as a function of Q^2 for the orthorhombic and hexagonal phases are shown in Figure 25c and Figure 25d, respectively. *Γ(Q)* has values on the order of few μeV in the orthorhombic phase while values are more than order of magnitude larger in the hexagonal phase. Since the motion is well described by the Chudley-Elliott jump diffusion model, it can be attributed to the long-range translational diffusion of the hydride ions. Jump lengths and residence times were extracted from the data using the Chudley-Elliott model and used to calculate diffusion coefficients with Eq. (4.4). A summary of the fit parameters is displayed in Table 5. The diffusion coefficients are displayed in the Arrhenius plot in Figure 26 along with activation energies, E_a, and the temperature independent preexponential diffusion coefficient, D_0.

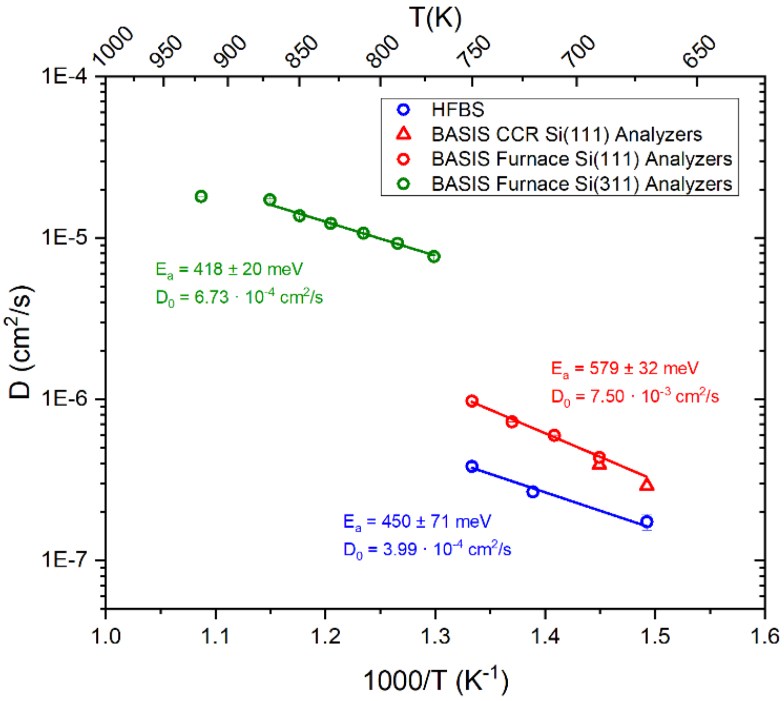

Figure 26: Arrhenius diagram for BaH_2 with diffusion coefficients calculated from QENS. Solid lines are a linear fit of the data. Activation energies and preexponential diffusion coefficients are reported.

First, the diffusive motion in the orthorhombic phase will be discussed. Again, this signal is first observed at $T = 600$ K but can only be reliably fit starting at 670 K. This motion can be measured using BASIS, but the narrow broadening is close to the resolution limit of $\Gamma = 1.75$ μeV. To better resolve this motion, HFBS with higher resolution ($\Gamma = 0.4$ μeV) was used. As seen in Table 5, the jump lengths at HFBS yield values around $L = 4.2$ Å while the jump lengths from BASIS reside over a range of $L = 3.6 - 4.2$ Å. To compare this with the structural data, deuterium-deuterium (D-D) distances in BaD_2 reported from neutron diffraction measurements for both phases are displayed in Figure 27.[13] The actual protium-protium (H-H) distances in BaH_2 are not expected to be significantly different than D-D distances in BaD_2.[13, 77] For clarity in this section, we will no longer dissociate between protium and deuterium, instead referring to both as hydrogen. Figure 27 shows that the shortest H-H distances in the orthorhombic structure can be separated into three main regions of approximately 3.1 Å, 3.6 Å, and 4.2 Å. The first region contains the shortest distances (3.1 Å), which corresponds to both H(1)-H(2) and H(1)-H(1) distances. The second region contains the next shortest distances (3.6 Å) due exclusively to H(2)-H(2) distances. The third region (4.2 Å) corresponds to both H(1)-H(1) and H(2)-H(2) distances. Therefore, the observed jump lengths from QENS ($L = 3.6 - 4.2$ Å) relate to the distances in the second and third regions. Thus, the possible jumps in the orthorhombic phase are from H(1) to H(1) or from H(2) to H(2) sites. Potential diffusion pathways corresponding to these types of jumps are illustrated in Figure 28. The fact that the BASIS measurements show jump distances ranging between 3.6 Å and 4.2 Å could be interpreted as a combination of jumps in the second and third regions on a similar time scale. In this case, the jump lengths would assume an averaged value between these two distances. Since the shorter distances of 3.6 Å only correspond to the H(2)-H(2) distances, H(2) may be the more important contributor to the ionic conductivity since it can undergo long range diffusion through a series of 3.6 Å and 4.2 Å jumps. However, the previous PDF measurements did not show a significant difference between the atomic displacement parameters for either site. The diffusion pathway had been previously assumed to be along the (102) plane, where the H-H distances are the shortest, i.e. 3.1 – 3.2 Å.[13] However, our QENS results suggest that the hydride ions are not diffusing along the shortest available paths. In addition, these results suggest that H(1)-H(2) jumps are not occurring readily in the orthorhombic phase, since these types of jumps correspond to the shortest distances of roughly 3.1 Å. As seen in the Arrhenius diagram (Figure 26), the activation energy measured at HFBS is lower than at BASIS, 453 meV and 572 meV, respectively. Due to the different energy resolution and energy transfer ranges at these spectrometers, it is possible that we observed a single jump process (4.2 Å jump length) at HFBS and a combination of two processes (3.6 Å and 4.2 Å jump lengths) at BASIS, which explains the difference in the obtained activation energies. The average of the two values from HFBS and BASIS is very close to the experimental activation energy of 520 meV reported by Verbraeken et al. using EIS.[13] While computational modelling could shed some light on the energy landscape, the significant hydrogen substoichiometry makes the modelling very difficult, if not impossible.

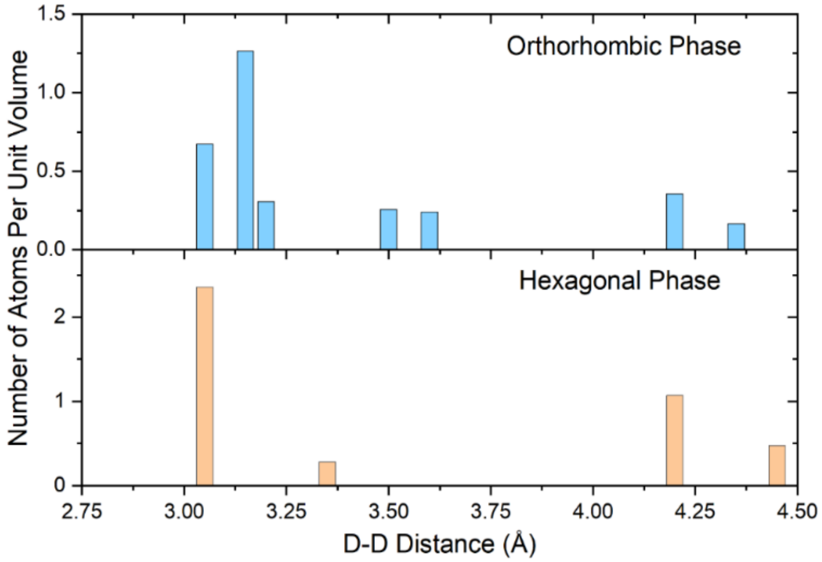

Figure 27: D-D distances reported from neutron diffraction data for BaD_2.[13] The orthorhombic and hexagonal (non-split D(1) sites) phases were measured at T = 670 K and 883 K, respectively.

Next, we will discuss the diffusive motion in the hexagonal phase. The phase transition is clearly observed in the Arrhenius plot (Figure 26) where the diffusion coefficients increase by approximately an order of magnitude around T = 775 K. The diffusion process in the hexagonal phase has an activation energy of 418 meV, which is lower than both values calculated for the orthorhombic phase. A reduction in the activation energy for ionic transport is common following a transition to a higher symmetry phase. However, both the orthorhombic and hexagonal phases were reported to have the same activation energy from previous EIS measurements (520 meV).[13] The QENS value is notably lower than that from EIS for the hexagonal phase. The activation energies calculated using these two techniques may be different because of the difference in time and length scales that each technique probes. For example, EIS probes bulk diffusion over macroscopic length scales while QENS reveals information about diffusive motions on the angstrom scale. The jump lengths extracted from QENS are all very close to 3.1 Å, which is in perfect agreement with the shortest H-H distance, as seen in Figure 27. This distance corresponds to the H(1)-H(2) sites which were previously restricted in the orthorhombic structure. The H(1) sites now act as a 'steppingstone' for the diffusion process, allowing the hydrogen to diffuse in virtually any direction through the crystal structure along 3.1 Å jumps. Hence, the phase transition reduces the energy barrier that restricted the H(1)-H(2) jumps in the orthorhombic phase. As a result, the hydrogen is now allowed to diffuse along using the shortest H-H distances in the structure. As expected, this produces residence times that are significantly shorter in the hexagonal phase, i.e. tens of picoseconds compared to nanoseconds. These results also agree with the PDF results, where the atomic displacement factors were very large along the c-axis for the D(1) sites, indicating transport along this direction. The site splitting would further reduce the jump length from 3.1 Å to 2.8 Å (or increase it to 3.4 Å). However, the QENS measurements consistently yield jump lengths of approximately 3.1 Å, which indicates that QENS just observes the average jump length from this site.

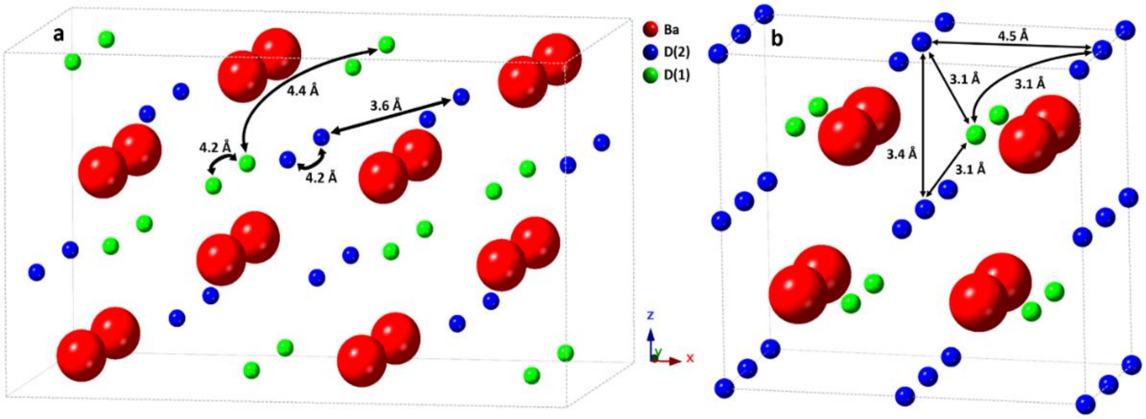

Figure 28: Crystal structures and potential diffusion pathways in BaD_2 for the (a) low temperature orthorhombic phase at 670 K and the (b) high temperature hexagonal phase at 883 K from neutron diffraction measurements.[13]

6.2.1 Vibrational Density of States: Inelastic Neutron Scattering

The vibrational density of states can be measured by INS to examine how bonding and local structure influences dynamic processes, such as the hydrogen release mechanism and diffusion. Since diffusion is a thermally activated process, it is highly dependent on the collective dynamics of the host lattice. With the hydrogen residing on two distinct crystallographic sites, their contributions to the INS spectra can be separated because they produce distinct vibrational modes at different energies. This can provide insight into which hydrogen site releases first and can begin participating in the diffusive motion. For example, if the H(1) vibrational modes disappear first upon increasing temperature while the H(2) modes remain intact, we could conclude that the H(1) site released first and began diffusing through the system. Therefore, we conducted a temperature dependent INS investigation of BaH_2 at VISION,[28] with the spectra shown in Figure 29. The neutron vibrational spectra of BaH_2 has been studied previously.[53, 54, 57] The spectra can be divided into four distinct regions: (1) the acoustic phonons below 50 meV, (2) the optical phonons of H(2) atoms from approximately 50 meV to 85 meV (3) the optical phonons of H(1) atoms from approximately 85 meV to 125 meV and (4) the multi-phonon modes at energies above 125 meV. The sharp distinct modes at 5 K begin to decrease in intensity and broaden as temperature increases, as expected with Debye-Waller behavior. There is a small excess contribution still present in the spectra at 450 K for both the H(1) and H(2) optical modes, but it is very broad. This suggests that the Ba-H bonds remain intact at 450 K, but that the hydrogen is weakly bound. By the next measurement at 600 K, the modes have completely disappeared, and the hydrogen is now undergoing long-range translational diffusion. This is the same temperature that a quasielastic signal is first observed using QENS. In agreement with the QENS and PDF results, both the H(1) and H(2) modes are equally decaying in the orthorhombic phase, suggesting that both hydrogen sites are mobile and behaving in a similar way.

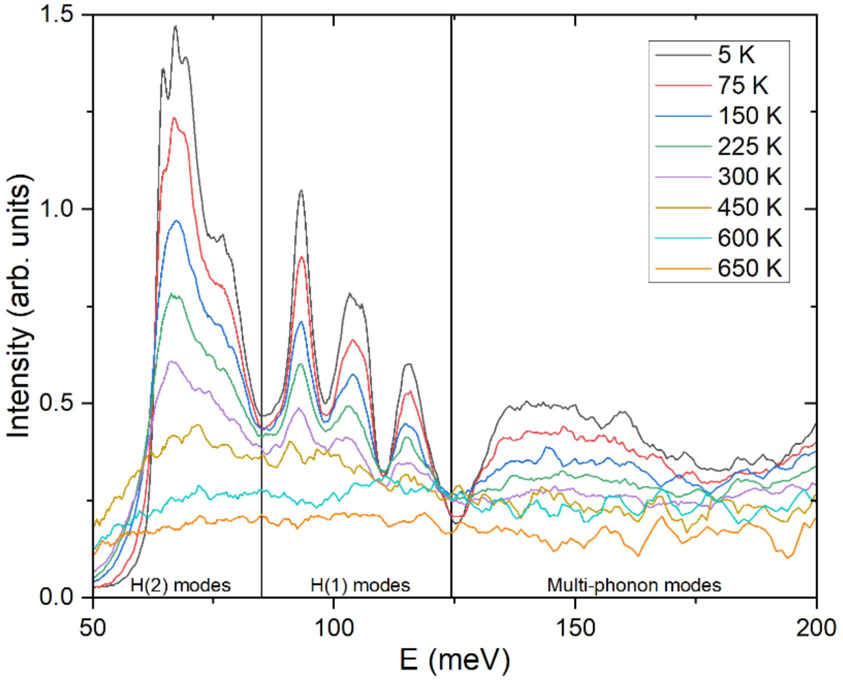

Figure 29: INS spectra from 5 K to 650 K for BaH_2 measured at VISION. The optical phonon modes corresponding to H(1) and H(2) sites, as well as multi-phonon modes, are labeled. Intensities is translated for clarity.

6.3 Pressure Dependence

The temperature dependent properties of barium hydride are now rather well understood, but knowledge about the pressure dependence remains incomplete. Previously, BaH_2 has been studied at high pressures previously using XRD,[49, 87] EIS,[16] and *ab-initio* computational methods.[16, 48] These investigations have discovered that the orthorhombic to hexagonal phase transition can be induced using pressure over a pressure range of P = 1.6 – 4.0 GPa at room temperature.[16, 48, 49, 87] The EIS measurements showed that the high pressure hexagonal phase also exhibits high ionic conduction and that it increases with pressure.[16] In addition, a second phase transition has been observed in BaH_2 around P = 50 GPa which forms the AlB_2 structure (space group *P6/mmm* (191)).[87] Since XRD is unable to observe hydrogen in the presence of heavier atoms, i.e. Ba, we used high pressure NPD to characterize the pressure dependent structure with the goal of determining the deuterium positions. Secondly, we investigated the hydrogen dynamics in the hexagonal phase using high pressure QENS. Details of the experimental and data analysis methods for the high pressure experiments can be found in Chapters 3 and 4 (and Appendix), while the pressure determination methods are described in Section 4.3.

6.3.1 Diffraction

Refined parameters for the BaD_2 phases consisted of phase fractions, lattice parameters, atomic coordinates, anisotropic atomic displacement parameters (U), and pseudo-Voigt profile parameters. The fractional occupancies were determined to be 0.85 and 0.88 for the D(1) and D(2) sites respectively and kept fixed for all pressures. Approximately 8 mol% of BaO has been observed as an impurity phase in the sample. The pressure dependent structure of BaO has been reported previously.[88, 89]

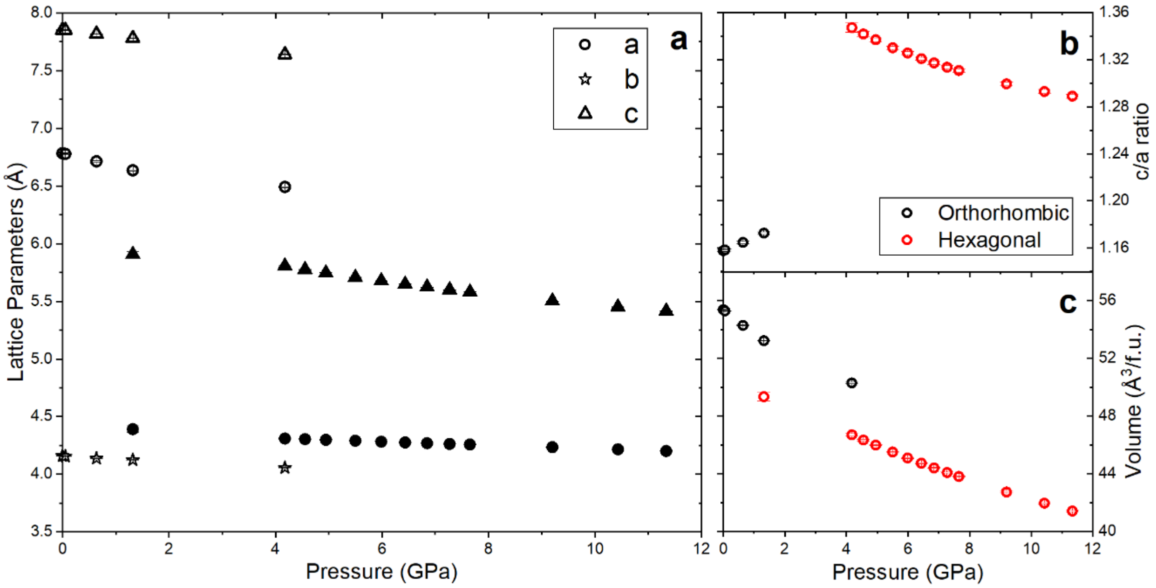

Figure 30: (a) Pressure dependence of the lattice parameters for the orthorhombic and hexagonal phases of BaD_2. (b) c/a lattice parameter ratio. (c) Volume of a formula unit of BaD_2 as a function of pressure.[90]

With no applied pressure, the lattice parameters for BaD_2 were determined to be a = 6.782(2) Å, b = 4.159(1) Å, and c = 7.851(2) Å, which agrees well with previous NPD measurements.[13] The pressure dependence of the unit cell volume is displayed in Figure 30. The orthorhombic phase exists up to a pressure of approximately 1.3 GPa. At this pressure, the hexagonal phase begins to form (12 mol% at 1.3 GPa) and coexists with the orthorhombic phase up to a pressure of 4.9 GPa. At 4.9 GPa, only 11 mol% of the orthorhombic phase remains and is essentially fully converted by the next pressure point (5.5 GPa). Previous reports on BaH_2 report the phase transition occurring over a wide pressure range from P = 1.6 – 4.0 GPa.[16, 48, 49, 87] Our investigation verifies these previous reports, clearly showing that both phases coexist over this wide pressure range. This is similar to our temperature dependent NPD/PDF experiment on BaD_2, where both phases coexisted over a large temperature range (Figure 20). The pressure-load curve, previously displayed in Figure 13, shows that the phase transition actually occurred across a narrow applied load. The large increase in the observed sample pressure is due to the sample transitioning from a lower to higher density phase. The volume contraction allows the gasket to compress more easily for the same applied load.

For the hexagonal phase at 4.2 GPa, the lattice parameters were determined to be *a* = *b* = 4.309(8) Å and *c* = 5.805(6) Å. The pressure dependence of the lattice parameters is displayed in Figure 30a. A gradual decrease is observed for all the cell parameters in both phases. Consistent with previous studies on BaH_2, the *a*-axis in the orthorhombic phase, which converts to the *c*-axis in the hexagonal phase, shows the most compressibility.[87] For the orthorhombic phase, compressibilities (β) were determined to be 0.112(1) GPa^{-1}, 0.026(2) GPa^{-1}, and 0.0549(6) GPa^{-1} along the *a*-, *b*-, and *c*-axes, respectively. Likewise, values for the hexagonal phase are 0.01505(4) GPa^{-1} and 0.054(1) GPa^{-1} for the *a*- and *c*-axes.

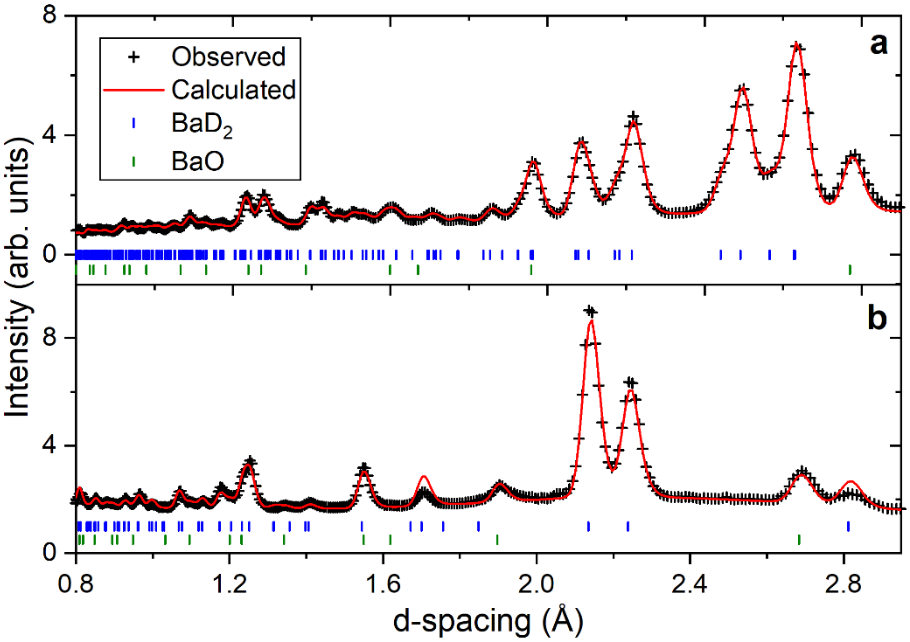

Figure 31: SNAP neutron diffraction pattern for BaD_2 at (a) ambient pressure (orthorhombic phase) and (b) P = 6.9 GPa (hexagonal phase).

The observed and calculated NPD patterns for both phases of BaD_2 are displayed in Figure 31. At ambient pressure, the refinement yielded R_{wp} = 4.12%, R_{exp} = 0.49%, and the reduced χ^2 = 77.3. At P = 6.9 GPa, the values are R_{wp} = 5.08%, R_{exp} = 0.5%, and χ^2 = 104.6. While the residual values are rather large, visually there is an excellent agreement with the experimental data for both phases. The large residual values can be attributed to multiple factors. First, the background varies significantly across the entire diffraction pattern and changes as a function of pressure. Therefore, the background was fit manually using Chebyshev polynomials with 8 to 15 coefficients for an adequate fit. Second, there is a slight intensity mismatch observed in some of the hexagonal BaD_2 peaks which becomes more prominent at higher pressures (Figure 31b). This is likely due to preferred orientation, a very common feature in non-hydrostatic high-pressure experiments, i.e. those conducted without a pressure transmitting medium. Preferred orientation corrections were not applied in order to minimize the number of free parameters in the refinements. Third, noticeable deviations are observed in the peak profile associated with the BaO impurity phase. This is expected since only lattice parameters and phase fractions were refined for this phase to reduce the number of parameters. Many investigations would use a Lebail fit for the BaO phase, which can greatly underestimate the residual values. Despite the large residual values, the cotunnite and Ni_2In-type phases successfully describe the experimental data across the entire pressure range and the extracted parameters are reliable.

One of the goals of this investigation was to confirm the hydrogen positions suggested from the previous XRD and NPD experiments.[13, 49] All of the atoms in the orthorhombic phase are located on special 4c (x, 0.25, z) positions. At ambient conditions, x = 0.350(1) and z = 0.425(2) for the D(1) atoms, x = 0.961(2) and z = 0.6896(9) for D(2), and x = 0.250(2) and z =0.104(1) for Ba. All of these values agree with a previous NPD study of BaD_2.[13] The pressure evolution of the atomic coordinates in the orthorhombic phase is displayed in Figure 32. No drastic changes occur leading up to the phase transition. The x-coordinates remain mostly constant as pressure increases but the z-coordinates increase slightly in both deuterium sites. For the hexagonal phase, the Ba is located on 2b sites (0.33, 0.66, 0.25), D(1) on 2d sites (0.33, 0.66, 0.75), and D(2) on 2a sites (0, 0, 0) for the entire pressure range up to 11.3 GPa. Note, the non-split D(1) site model was used because the results did not indicate site splitting with pressure. It is possible that these dynamic fluctuations require significant thermal activation to occur.

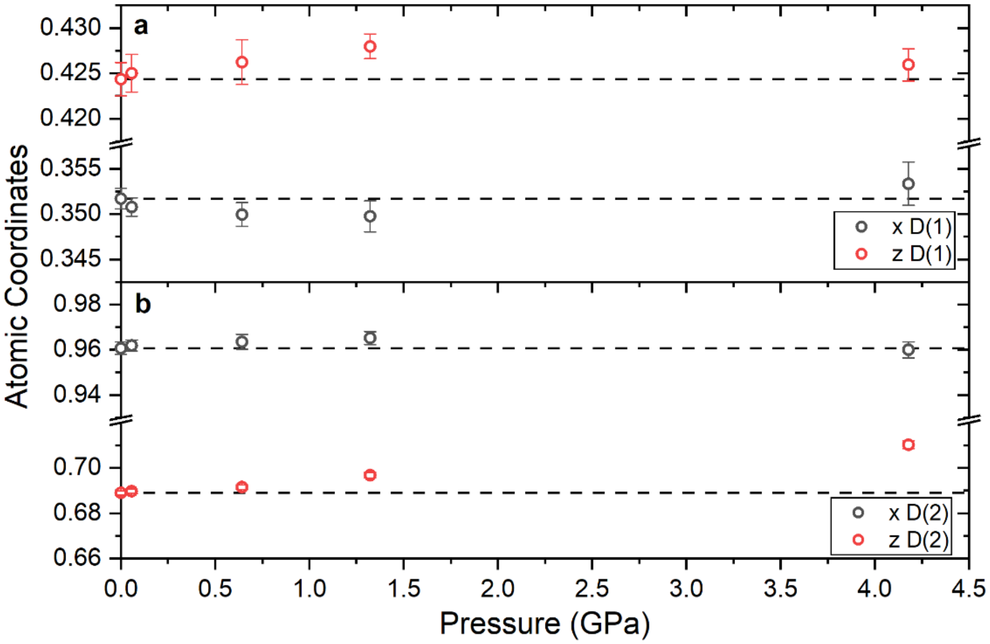

Figure 32: Pressure dependence of the special atomic coordinates for (a) D(1) and (b) D(2) atoms. Horizontal lines are positioned at the value for no applied pressure.

Many ionic AX_2-type compounds (A = metal), including the HAEH group, crystallize in the cotunnite structure at ambient conditions and transition into the Ni_2In-type structure at higher pressures. These compounds possess similar properties and an interesting trend has been observed in the lattice parameter ratios for both phases: for the cotunnite phase, values for c/a and $(c + a)/b$ are around 1.15 and 3.5, respectively. In addition, the c/a ratio in the Ni_2In-type structure is approximately 1.34 just following the phase transition.[48, 49, 87] In agreement with the trend, the values for BaD_2 were determined to be 1.158 (c/a) and 3.518 ($(c + a)/b$) for the orthorhombic phase and 1.347 (c/a) for the hexagonal phase. Similarly to BaH_2, the (c/a) ratio in the hexagonal phase reduces with increasing pressure to a value of 1.289 at 11.3 GPa.[49] Interestingly, this is in contrast with the Ni_2In-type structure of BaF_2, where the c/a ratio increases slightly with pressure.[79] This is noteworthy since BaF_2 has been a popular compound in the past for isostructural comparisons to the HAEHs.[49, 79]

6.3.2 Hydrogen Dynamics: Quasielastic Neutron Scattering

Now that the pressure dependence of the crystal structure is well-characterized, the nature of the pressure induced hydrogen dynamics can be investigated. We conducted high pressure QENS measurements to probe the hydrogen diffusion process under applied pressure. We report here high pressure QENS measurements on BaH_2 up to a maximum pressure of 7.1 GPa. For these experiments, we adapted the Klotz and Bove set-up.[36, 37] Further details can be found in those reports. QENS spectra ranging from ambient conditions (instrument resolution function) up to 7.1 GPa are displayed in Figure 33. Quasielastic broadening is observed compared to the resolution function and it increases with pressure. Previous electrochemical impedance spectroscopy measurements have shown that the ionic conductivity increases in the hexagonal phase with increasing pressure.[16] Our results also indicate faster hydrogen dynamics with pressure. The QENS data is averaged over the entire measured angular range because the statistics were not suitable for a detailed Q-dependent study. By fitting the quasielastic broadening with a Lorentzian function, the Q-averaged HWHM is determined to be 27 ± 5 μeV and 39 ± 8 μeV for the pressures of 6.2 GPa and 7.1 GPa, respectively. This corresponds to timescales of 24.4 ps (6.2 GPa) and 16.9 ps (7.1 GPa). All three measurements shown here are in the hexagonal phase of BaH_2. However, the P = 4.9 GPa signal has too little intensity to accurately determine the HWHM and there may still be some remaining orthorhombic phase in this measurement. A more detailed QENS analysis unveiling the atomic scale origins of hydrogen diffusion in BaH_2 at elevated pressure will follow in a subsequent report pending additional measurements.

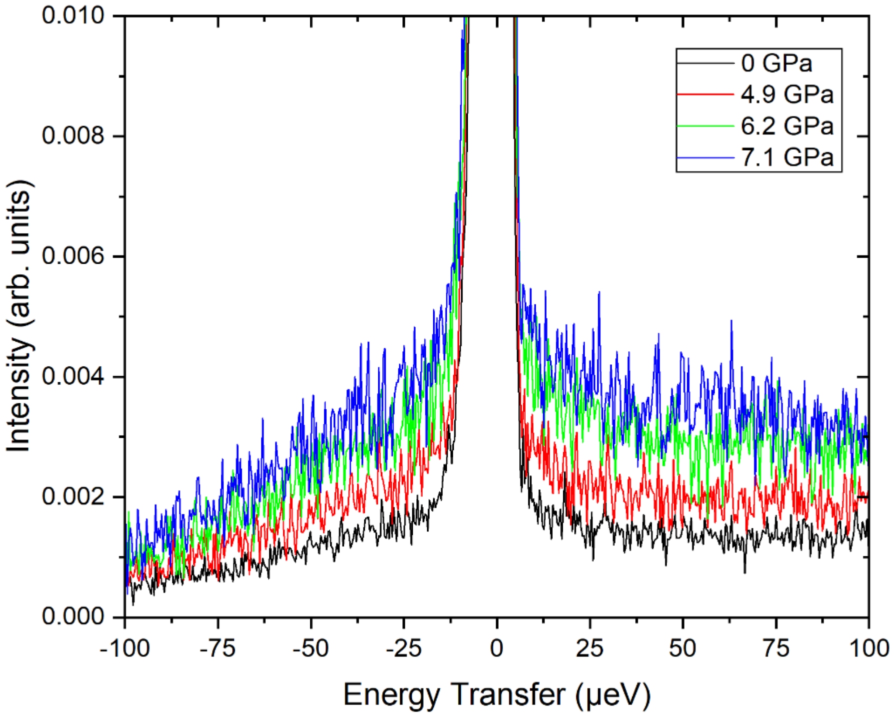

Figure 33: QENS spectra measured at BASIS for BaH_2 up to pressures of 7.1 GPa. All data is averaged into a single Q-bin and the intensities are normalized with respect to the elastic peak.

High pressure QENS in the GPa range is a relatively new field of study that is still being actively developed. Understanding single particle dynamics in materials under pressure is an excellent way to expand our knowledge about the behavior of materials in extreme environments. While high pressure QENS experiments in the MPa range are rather common, only a limited amount of investigations have achieved pressures in the GPa range.[36, 37, 91] To our knowledge, the highest sample pressure achieved in a QENS experiment was an investigation of water dynamics up to 3.3 GPa by Klotz, Bove *et al*.[36, 37] Therefore, our investigation has greatly improved on the current high pressure QENS capabilities by achieving a new maximum pressure of 7.1 GPa. Despite the lack of a proper Q-dependent study of BaH_2 with high pressure QENS, these results demonstrate the exciting new capabilities that are being developed as we push the current boundaries in the field of high pressure QENS.

6.4 BaH_2 Summary of Results

The temperature and pressure dependence of the local and global crystal structure of BaD_2 using NPD and total neutron scattering. The orthorhombic cotunnite structure correctly describes the PDFs up to the phase transition at 775 K. Changes in the atomic coordinates are observed for the Ba, D(1), and D(2) sites preceding the phase transition. At 775 K, the hexagonal phase begins to form and coexists with the orthorhombic phase until the transition is completed around 850 K – 900 K. The phase transition resembles a first-order transition with respect to the significant decrease in cell volume vs. temperature. However, the gradual structural change involving small modifications of the lattice parameters and atomic coordinates over a large temperature range suggests a possible second-order nature. The hexagonal phase is well described by the Ni_2In-type structure. Large atomic displacement factors associated with displacement of D(1) atoms along the *c*-axis suggests that the D(1) site is split and resides on the lower symmetry 4f sites. The PDF showed that the local structure remains mostly unchanged following the phase transition while the global structure transitions into a higher symmetry phase. However, there is an intermediate transition region bridging the gap between the local and global structures (r = 6 Å – 13 Å) that is highly disordered in the hexagonal phase. This can be attributed to rotational degrees of freedom with respect to the anionic polyhedra in the structure. These dynamic fluctuations can greatly assist the hydrogen diffusion process. In addition to temperature, pressure has been found to also induce the orthorhombic to hexagonal phase transition. Similar to the temperature dependent study, the phase transition occurred over a wide pressure range (P = 1.3 – 4.9 GPa). Both the low pressure orthorhombic and high pressure hexagonal phases are well described by the cotunnite and Ni_2In-type models, respectively.

The temperature and pressure dependence of the hydrogen dynamics was investigated in barium hydride using QENS. The temperature dependent study showed that the hydride ions undergo jump diffusion between various hydrogen lattice sites, as explained by the Chudley-Elliott jump diffusion model. We have determined the preferred jumps in the lattice for both the orthorhombic and hexagonal phases, with each phase showing very different dynamics. In the orthorhombic phase, two distinct jump lengths of approximately 3.6 Å and 4.2 Å were found. The first one (3.6 Å) corresponds to a distance between H(2)-H(2) sites. The second one (4.2 Å) corresponds to distances between both H(2)-H(2) and H(1)-H(1) sites. Despite the shorter distance (3.1 Å) between H(1)-H(2) sites, we do not observe such jumps in the QENS measurements. Following the phase transition, jump lengths were found to be around 3.1 Å in the hexagonal phase, which corresponds to jumps between H(1)-H(2) sites. The phase transition enables the previously restricted H(1)-H(2) jumps in the orthorhombic phase. This change allows the hydrogen to diffuse efficiently through 3.1 Å jumps with an activation energy of 418 meV, which is significantly lower than in the orthorhombic phase, 512 meV. Furthermore, the jump rate increases by an order of magnitude upon the phase transition promoting the faster diffusion. The dynamic fluctuations observed in our structural study cause the D(1) site to be split, a feature that is key for unlocking the fast hydrogen diffusion in the hexagonal phase. As mentioned before, the same phase transition that occurs in BaH_2 at high temperature can be induced at high pressures. Recent reports suggest that ionic conduction in BaH_2 increases with pressure in the hexagonal phase. We performed high pressure QENS measurements on BaH_2 up to a maximum pressure of 7.1 GPa. Our preliminary results show that there is a quasielastic signal that increases with pressure with a HWHM broadening of approximately 39 ± 8 μeV at 7.1 GPa. To our knowledge, this is the highest pressure currently achieved in a QENS experiment. We plan to expand this study in future experiments to obtain better statistics for a proper Q-dependent investigation to unveil the diffusive pathways in this high-pressure phase. In addition to the QENS measurements, the lattice dynamics and vibrational density of states was probed over a temperature range of 5 K to 650 K using INS. The weakening of the hydrogen bonds was observed as a gradual decrease in the intensity and a softening of the vibrational modes. The modes associated with the H(1) and H(2) sites had a similar temperature dependence, which suggests that both sites contribute equally to the ionic conduction in the cotunnite phase. A similar trend was observed in the atomic displacement parameters extracted from the PDF measurements. Lastly, hydrogen release was observed around 600 K, which is the temperature that diffusion begins to be observable in the QENS measurements.

7 CALCIUM HYDRIDE

Calcium hydride is a HAEH that crystallizes in the same cotunnite crystal structure as BaH_2. As a result, these materials share similar materials properties, such as a high decomposition temperature of $T_{dec} \approx 940$ K. CaH_2 is intriguing for applications due to ability to store larger densities of hydrogen (4.75 wt%) compared to BaH_2 (1.44 wt%).[15] However, the hydrogen transport becomes increasingly slower in the HAEH group as the size of the cation decreases, i.e. BaH_2 > SrH_2 > CaH_2. The fast-ionic conduction in BaH_2 is unlocked following a structural phase transition. However, a similar phase transition has not been observed with temperature in CaH_2 and hence the hydrogen transport remains modest. Our goal is to investigate the temperature dependent structure of CaD_2 using total neutron scattering to observe how the local and global structures change in this material. Despite the lack of a first-order phase transition, there may be subtle rearrangements of the atomic positions that can be exploited in the future to induce the phase transition in this material, with the ultimate goal of increasing the hydrogen transport properties. Second, we will use QENS to investigate the hydrogen diffusion mechanism and INS to probe the lattice dynamics.

7.1 Crystal Structure

The crystal structure of calcium hydride has been studied previously.[17, 55, 92] Again, this material crystallizes in the cotunnite structure (orthorhombic, space group *Pnma* (62)), which makes it isomorphic to BaD_2 (cotunnite crystal structure displayed in Figure 17a for BaD_2). The lattice parameters of CaD_2 at ambient conditions are a = 5.9455(1) Å, b = 3.5917(1) Å, and c = 6.7997(1) Å.[17] This is a significantly smaller unit cell than BaD_2 (a = 6.782 Å, b = 4.159 Å, and c = 7.851 Å). The Ca, D(1), and D(2) sites are all positioned on *4c* sites (x, 0.25, z). The values for x and z are 0.2407(3) and 0.1094(2) for Ca, 0.3553(2) and 0.4265(2) for D(1), and 0.9749(2) and 0.6756(2) for D(2).[17] Similar to BaD_2, CaD_x has been reported to have significant deuterium sub-stoichiometries with $x \sim 1.91$.

The decomposition temperature has been determined to be approximately 940 K, which means that the thermal stability is similar to BaD_2.[13, 17] Unlike BaD_2, no first-order phase transitions occur in CaD_2 upon heating from room temperature. However, previous differential thermal analysis (DTA) and EIS measurements have indicated a second-order phase transition occurring in CaH_2 above 700 K.[93] They attributed this to an order-disorder transformation, potentially with respect to the hydrogen sites. At low temperatures, the hydrogen is ordered and a gradual disordering occurs as the sample is heated. There is a noticeable discrepancy between the EIS and DTA measurements in that work: the EIS measurements suggests the transition occurs around 733 K (value is not reported for CaD_2), while the DTA results suggest it begins around 808 K for CaH_2 and 832 K for CaD_2. The EIS measurements show a decrease in the activation energy corresponding to the bulk conductivity beginning at 733 K, which indicates a structural (order-disorder) transition. The DTA measurements show an exothermic process beginning around 808 K that is observed as a gradual change in the slope of the DTA measurement over a large temperature range. This behavior is typically indicative of a second-order phase transition. The EIS and DTA measurements show that there are clearly some structural and dynamical changes occurring around 733 K and again above 800 K in this material.

7.1.1 Total Neutron Scattering

A temperature dependent total neutron scattering investigation was conducted on CaD_2 over a temperature range of 300 K to 920 K. The experimental and calculated PDFs are shown in Figure 34. Overall, there is an excellent agreement between the experimental data and the theoretical model using the cotunnite structure. It can be observed that this model correctly describes both the local and global atomic structures over the distance range of r = 1.5 – 35 Å. An interesting feature is observed around the length scales of 15 Å – 23 Å as the sample is heated. The modes in this region seem to broaden and increase in intensity more than the rest of the pattern, which could be a sign of a disordered structure. This looks very similar to the disordered transition region observed in BaH_2 (see Section 6.1.2). This would also agree with the order-disorder transition that has been suggested to occur roughly around 832 K in CaD_2.

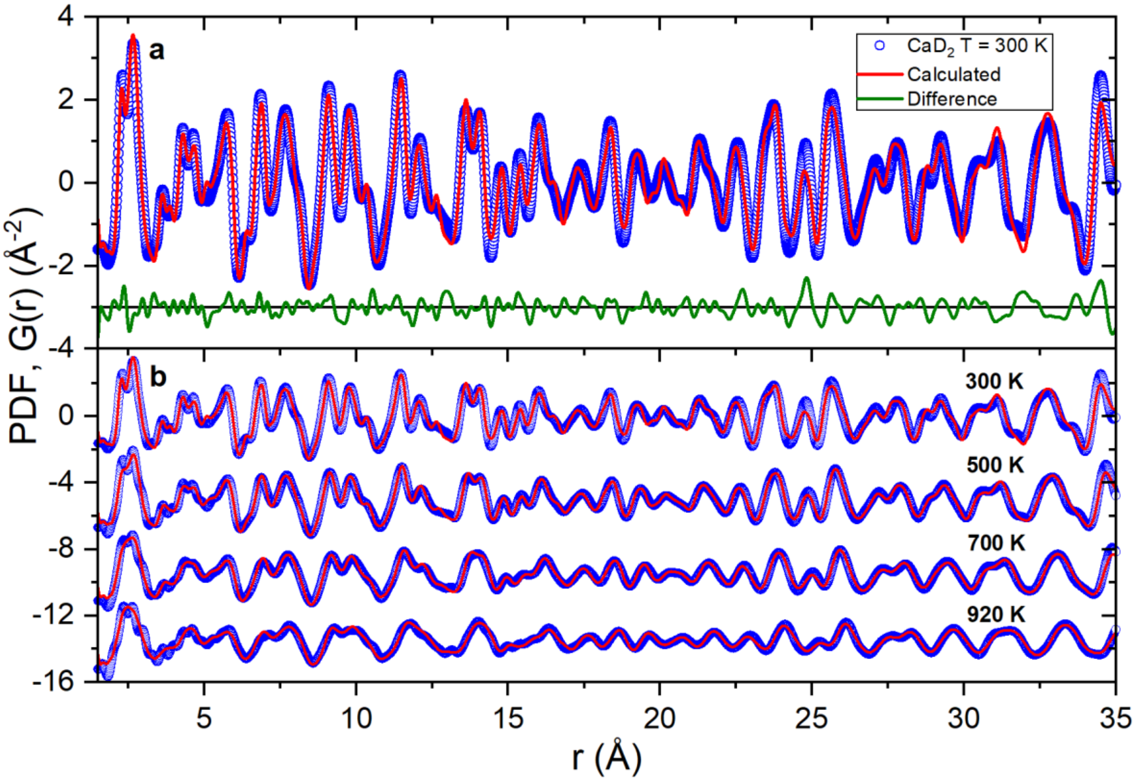

Figure 34: PDF G(r) vs. r showing the local and global structure for CaD_2 at (a) 300 K and (b) 300K – 920 K (*G(r)* are translated).

The local structure is shown in greater detail in Figure 35 for the same temperature range. Apart from a few minor deviations from the experimental data, the model clearly describes the data. Some interesting changes begin to appear with temperature, such as the emergence of extra peaks. For example, there is a double peak in the lowest *r* region (approx. 2 – 3 angstroms) in the 300 K data. We will refer to this as a doublet for clarity, but it is actually a superposition of many atomic distances. As the sample is heated, two additional peaks begin to emerge on the shoulders of this doublet: one around 2.1 Å and a second around 3 Å. The theoretical model struggles to capture these distinct peaks in the lowest *r* region as the temperature is increased. The other peaks in this pattern, i.e. 4 – 11 Å, have the general trend of broadening and decreasing in intensity upon heating. This is expected since the atomic displacement parameters also increase with temperature. As the atoms become increasingly mobile and the bonding weakens, the bond distances are less defined, and the peaks are smeared out.

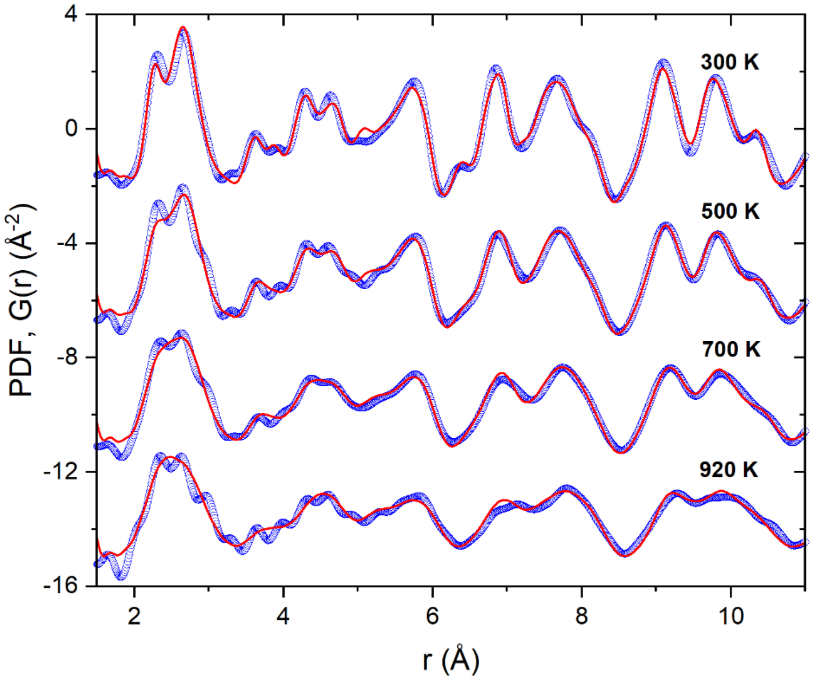

Figure 35: PDF G(r) vs. r showing the temperture dependence of the local structure in CaD_2 for a temparture range of 300 K – 920 K. PDF values are translated for clarity. Blue circles represent the experimental data and the solid red lines is the calculated model.

Refined parameters including lattice parameters, deuterium site occupancies, and anisotropic atomic displacement parameters (*U*) are displayed in Figure 36. The lattice parameters all increase with temperature with no unexpected features. The deuterium site occupancies increased slightly for D(2) but decreased significantly for the D(1) sites above 800 K. This suggests that the

D(1) atoms release from the site at a lower temperature compared to the D(2) sites, indicating it may be the more important hydrogen site for ionic conduction. Interestingly, this temperature corresponds to the thermal process observed in the DTA measurements.[93] There is no sign of a release occurring in the D(2) sites up to 920 K, which means it likely releases at the decomposition temperature of 940 K. Interestingly, the atomic displacement parameters for the D(1) sites are smaller by about half when compared to the D(2) sites. Previous NPD measurements at ambient conditions also reported larger displacement parameters for D(2) compared to D(1).[17] Interestingly, a sharp increase is observed in some of the atomic displacement parameters beginning around 850 K, which corresponds with the order-disorder temperature from DTA. This change is most prominent in the directions along the *a* and *b*-axes (U_{11} and U_{22}).

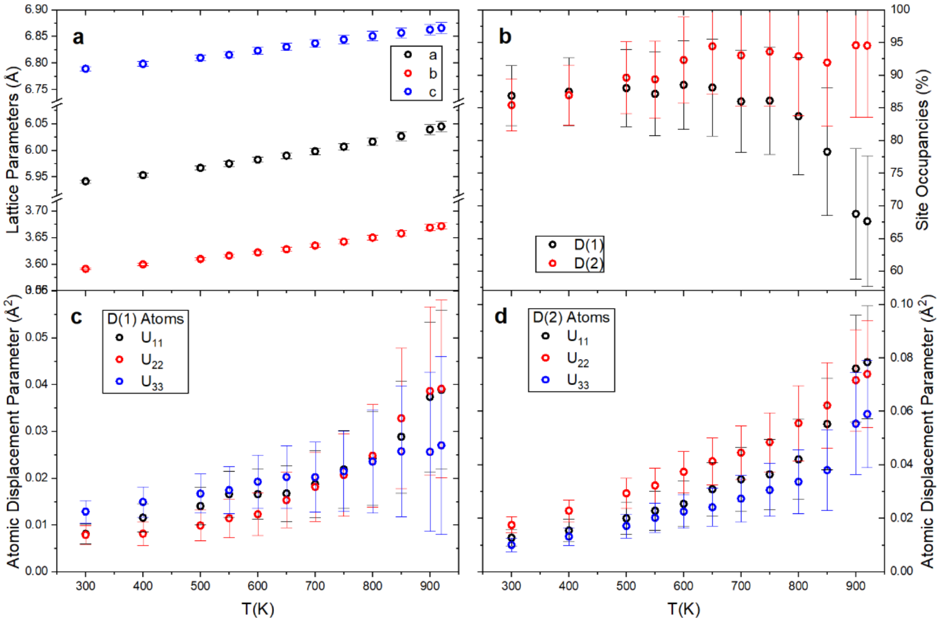

Figure 36: Refined parameters from PDF analysis for CaH_2. (a) Lattice parameters, (b) deuterium site occupancies, and atomic displacement parameters (U) for (c) D(1) and (d) D(2) sites.

The refined special atomic coordinates for all of the atomic positions (4c sites (*x*, 0.25, *z*)) are displayed in Figure 37. Again, previous EIS and DTA measurements indicate that structural/dynamical changes occur in the sample around 733 K (EIS for CaH_2) and at 832 K (DTA for CaD_2, 808 K for CaH_2).[93] Upon heating from room temperature, there is a noticeable decrease in the *z*-coordinates with temperature for both the Ca and D(1) sites while the other positions remain relatively constant. Around 600 – 700 K, the *x*-coordinate for Ca and the *z*-coordinate for D(1) begins to decrease more rapidly. This closely corresponds to the 733 K temperature from the EIS measurements. The EIS measurements were conducted in large $\Delta T = 50$ K steps, meaning there may be a large variation in the exact transition temperature. Also, an isotopic shift in the transition temperature is possible since only EIS values were reported for CaH_2. Upon additional heating, changes occur in all the atomic sites beginning around 800 K – 850 K, with the Ca and D(2) sites appearing to be most affected by this structural change. The additional peaks appearing in the PDF patterns as temperature increases suggests that there may be a more complex structure following this order-disorder transition that isn't fully captured with the cotunnite structure.

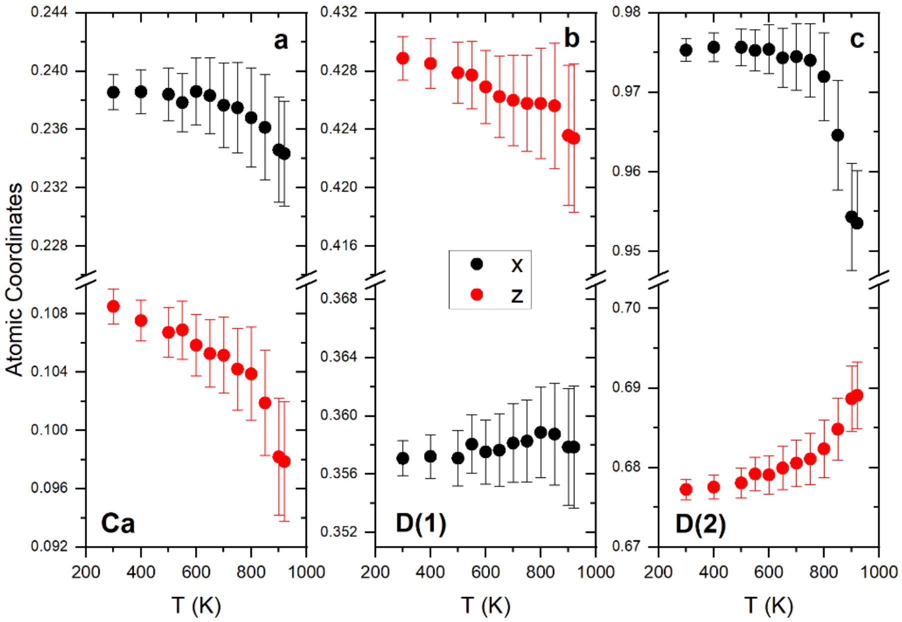

Figure 37: Atomic coordinates *x* and *z* for the (a) Ca, (b) D(1), and (c) D(2) sites for CaD_2.

7.2 Hydrogen Dynamics

7.2.1 Quasielastic Neutron Scattering

An elastic scan was conducted on CaH_2 over a temperature range of 270 K – 800 K at HFBS, as shown in Figure 38. A gradual decrease associated with Debye-Waller behavior is observed up to 680 K. At this temperature, a sudden increase in the elastic intensity is observed. Above 680 K, the elastic intensity continues to decrease and appears to do so more rapidly beginning around 780 K.

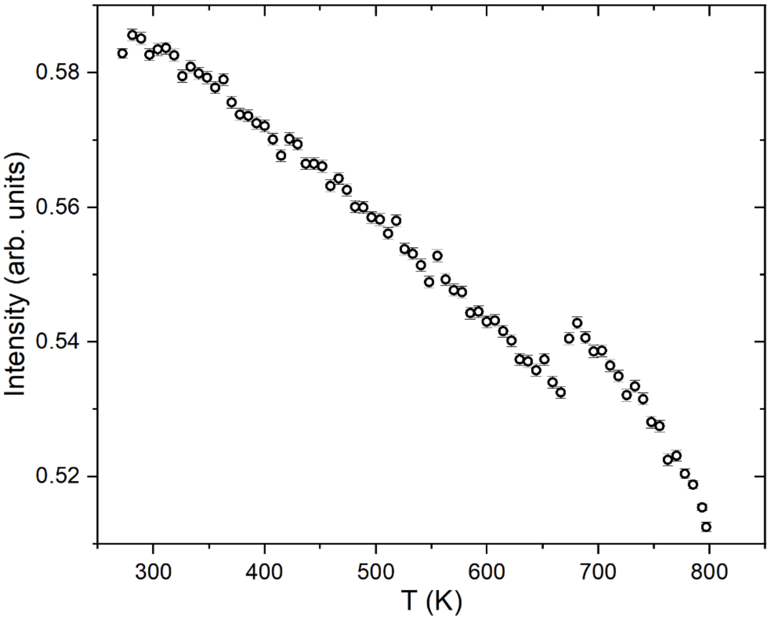

Figure 38: Elastic scan measured at HFBS for CaH_2 from T = 270 K – 800 K.

A sudden discontinuity in an elastic scan typically indicates a structural phase transition, where the hydrogen dynamics are different in the two phases. With no first-order phase transitions observed in this material, this might be due to a second-order phase transition.[93] As shown in the PDF results, the atomic coordinates for the Ca and D(1) sites begin to change around this temperature.

This slight modification could be significant enough to influence the hydrogen dynamics. The EIS measurements show a decrease in the activation energy corresponding to the bulk conductivity beginning at 733 K, which indicates a structural modification may have occurred. The increase in the elastic intensity in the elastic scan suggests that the motion initially slows down following this transition. This occurs at a lower temperature (680 K) compared to the EIS measurements (733 K). As mentioned previously, the EIS measurements were conducted in large temperature step sizes (~ 50 K steps) which means that the real transition temperature may be closer to 680 K. Heating rates and measurement times can also affect the reported transition temperatures.

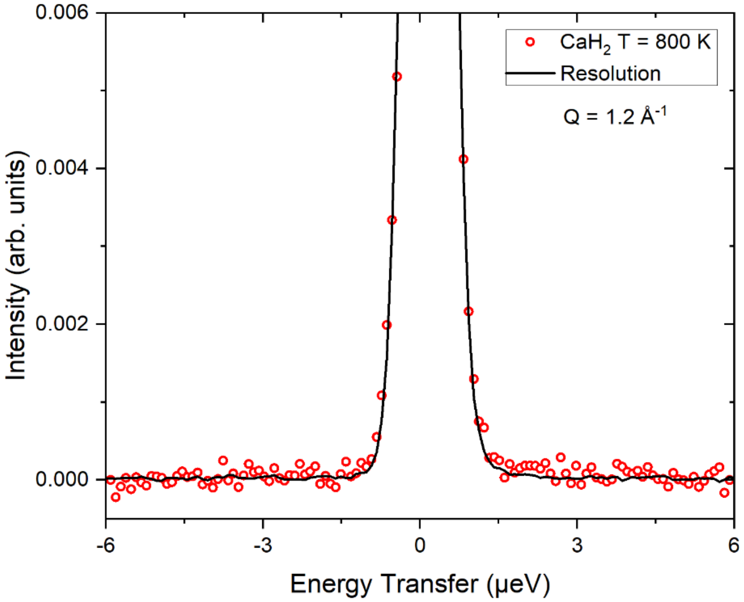

Figure 39: QENS spectra and resolution function measured at HFBS for CaH_2 at T = 800 K and Q = 1.2 $Å^{-1}$.

A longer QENS measurement was conducted at *T* = 800 K for CaH_2, with the spectra shown in Figure 39. As can be observed, there is no appreciable quasielastic broadening to the elastic peak. This indicates that the hydrogen is not diffusing on the timescale of the instrument (HFBS) at 800 K. The conductivity values from EIS suggest that the motion should become observable just above this temperature.[17, 93] However, measurements were limited to a maximum temperature of 800 K due to the sample environment used at the time. Studying the dynamics above 800 K would be an interesting future work considering the DTA measurements suggest a change in the sample occurs beginning around 832 K. In addition, the PDF results show that the D(1) site occupancy begins to decrease around this temperature as well. Likewise, the elastic scan shows a more pronounced decrease approaching 800 K.

7.2.2 Vibrational Density of States (INS)

INS spectra for CaH_2 were measured over a temperature range from T = 5 K to 750 K CaH_2, as shown in Figure 40. The 5K measurement was conducted in a CCR while the higher temperatures were measured in a furnace. A detailed account of the vibrational DOS for CaH_2 has been discussed elsewhere.[53-57] Since the structure of CaH_2 is isomorphic to the cotunnite structure of BaH_2, the vibrational DOS are practically identical, but with the modes in CaH_2 shifted to higher energies by ~15 – 20 meV (INS spectra for BaH_2 is shown in Figure 29). The H(2) modes are located in the energy region between 65 meV – 105 meV, the H(1) modes between 105 meV – 145 meV, and multi-phonon modes above 145 meV. This suggests that the Ca-H bonds in CaH_2 is notably stronger than those in BaH_2. Further evidence of this is the temperature evolution of the modes. In BaH_2, the modes were smeared out and almost completely merged with the background by the measurement at 450 K. Likewise, the 600 K measurement for CaH_2 shows this similar feature. In addition, the modes in CaH_2 are much more pronounced at room temperature when compared to BaH_2. Figure 40 shows that the modes merge with the background completely by the 700 K measurement. Therefore, the temperature dependence of the vibrational modes behaves in a similar manner to BaH_2, but is shifted to higher temperatures by roughly 100 – 150 K. This gives us a hint as to why no diffusive signal was observed in the QENS measurements up to 800 K. It is likely that the observable hydrogen diffusion would soon become observable at BASIS and HFBS above 800 K. In addition, the PDF results suggested that the H(2) site may release before the H(1) sites. Both sites seem to behave similarly with temperature in the INS spectra. However, the intensity reduction in the H(2) modes seems to be more pronounced than the H(1) modes between the 450 K and 600 K measurements, which could support the reasoning that this site releases at a lower temperature.

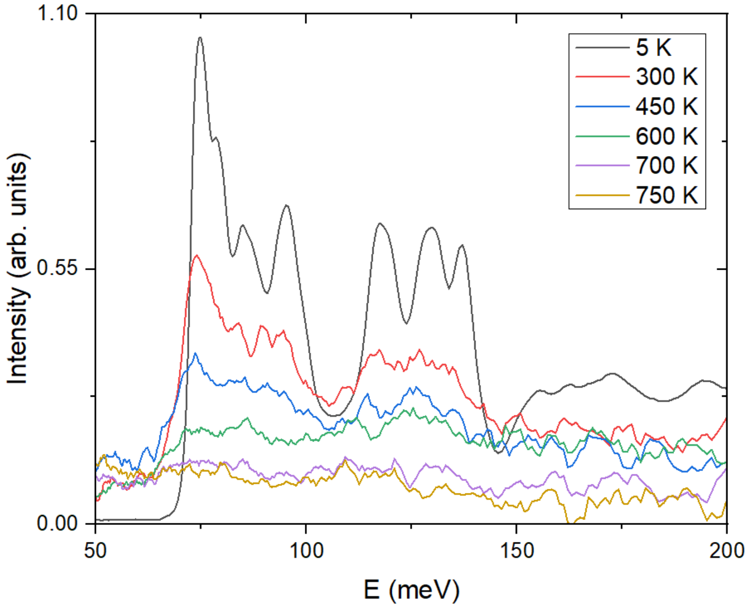

Figure 40: INS spectra from 5 K to 750 K for CaH_2 measured at VISION. Intensities are translated for clarity.

7.3 CaH_2 Summary of Results

The structure of CaD_2 was investigated with total neutron scattering over a large temperature range of 300 K – 920 K. While no first-order structural phase transitions were observed, an indication of a second-order phase transition was detected. There is a noticeable change in the atomic positions with temperature for both the Ca and D(1) sites between 600 – 700 K. This roughly corresponds to the temperature range in which a change in the activation energy was previously observed using EIS.[93] Upon additional heating, changes occur in the positions of all the atomic sites beginning around 800 K, which agrees with previous DTA measurements for a second order transition. The Ca and D(2) sites appear to be most affected by this structural change. These results suggest that there may be two distinct structural changes occurring in this material: the first between 600 K – 700 K and the second beginning above 800 K. QENS measurements were performed on CaH_2 to investigate the hydrogen dynamics. An elastic scan showed a sharp discontinuity around 680 K. This is typically indicative of a phase transition and occurs in a similar temperature range to the changes observed in the PDF and EIS measurements. The elastic intensity increased which suggests that the hydrogen dynamics initially slow down following this transition. Longer QENS measurements at T = 800 K did not show appreciable quasielastic broadening. However, our results suggest that a QENS signal would likely be observable above 800 K. The INS spectra also indicates that the hydrogen should be sufficiently mobile above 700 K and that the H(2) site may release at a lower temperature than the H(1) sites.

8 MAGNESIUM HYDRIDE

Up to this point, we have focused on the HAEHs of BaH_2 and CaH_2, which both possess similar materials properties. MgH_2 is a light-weight alkaline earth hydride that behaves quite differently than the HAEHs. For example, MgH_2 crystallizes in the rutile structure at ambient conditions, rather than adopting the cotunnite crystal structure of the HAEHs. The difference in the materials behavior is largely due to the nature of the metal-hydrogen bonds in these materials: the HAEHs are ionicly bonded while MgH_2 has covalent-like bonds. The strong covalent-like bonding leads to poor kinetic reversibility and causes the hydrogen transport to be extremely sluggish. This is unfortunate because the high hydrogen storage density (7.6 wt%) and the intermediate decomposition temperature ($T_{dec} \approx 600$ K) makes magnesium hydride very appealing for various applications.[14, 15] We employ here high temperature total neutron scattering, QENS, and INS measurements to characterize the local and global structures and to investigate the hydrogen dynamics.

8.1 Crystal Structure

The crystal structure of magnesium hydride has been previously determined through XRD and NPD.[94-96] MgD_2 crystallizes with tetragonal symmetry in the rutile-type structure with $a = b = 4.5010(1)$ Å and $c = 3.0100(1)$ Å at 260 K.[96] The space group is $P4_2/mnm$ (136), where Mg is located on the 2b sites at (0,0,0) and D is positioned on the 4f sites at (x, x, 0) with $x = 0.3040(2)$. Unlike BaD_2 and CaD_2, there is only one distinct hydrogen site in this structure. The Mg atoms are centered inside deuterium octahedra which run straight along the c-axis, as seen in the crystal structure shown in Figure 41. The rutile phase is stable until decomposition around 600 K. With pressure, MgH_2 undergoes a series of phase transitions that ultimately transforms the rutile structure into the cotunnite structure around 17 GPa. The cotunnite phase is stable up to 57

GPa.[97] Therefore, magnesium hydride may behave similar to the HAEHs at elevated pressures in the cotunnite phase.

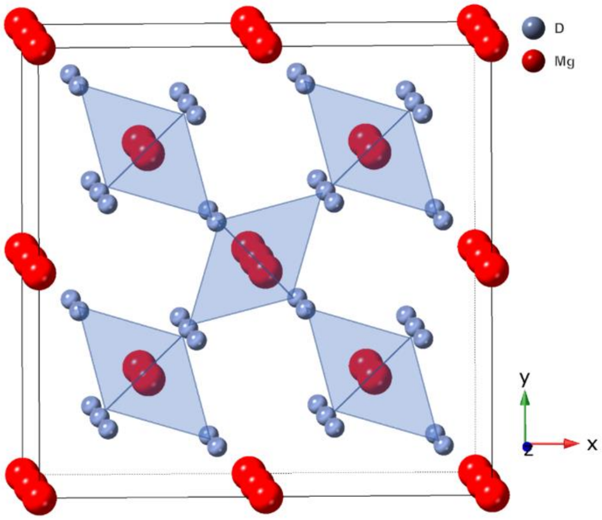

Figure 41: Rutile crystal struture of MgD_2.

8.1.1 Total Neutron Scattering and Diffraction

The local and global crystal structure of MgD_2 was investigated with total neutron scattering measurements over a temperature range of 100 K – 400 K, with the PDFs shown in Figure 42. The calculated pattern using the rutile structure well describes both the local and global structures. Most of the observed deviations are in the local region, which is largely due to differences in intensity. The peak positions are well reproduced by the rutile structure. The PDFs show almost no changes as the material is heated from 100 K to 400 K, as shown in Figure 42b. Likewise, the lattice parameters and atomic coordinates displayed in Figure 43 show only slight modifications with temperature. The lattice parameters at T = 300 K were determined to be $a = b = 4.509(3)$ Å and $c = 3.004(3)$ Å, which agree well with previous reports.[96] In addition, the atomic displacement parameters assume the modest values of U_{11} = 0.033 Å^2 and U_{33} = 0.017 Å^2 at T = 400 K, indicating that the covalent-like bonds in MgD_2 are strong and the deuterium atoms remain tightly bound. Therefore, the structure of MgD_2 is not changing significantly across the measured temperature range. There is a noticeable deviation in the lattice parameters and atomic coordinates at T = 100 K when compared to the trend established in the higher temperature measurements. It is unclear why this occurs, but it is possible that there is a small structural modification at low temperatures in this material. Since the atomic coordinates for the deuterium sites also display this change, it is possible that there is a redistribution of the deuterium sites. In addition, the fractional deuterium occupancies could not be properly determined and were fixed at 1.0. The refined occupancies were yielding a value around 1.06 which is not realistic. In addition, our study was limited to 400 K due to the sealed sample containers used at the time. Future studies could expand this structural study up to the decomposition temperature at 600 K to understand what changes occur proceeding the decomposition.

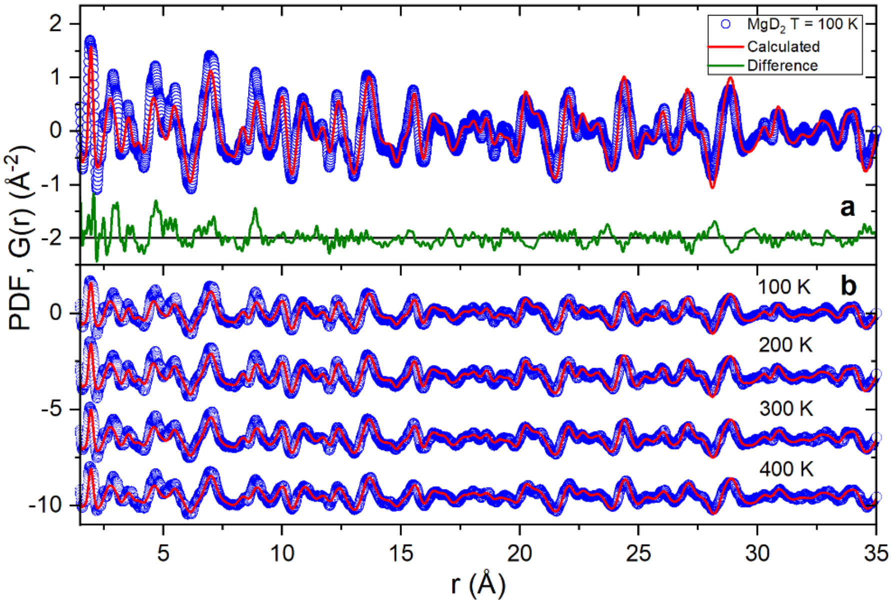

Figure 42: PDF G(r) vs. r for MgD_2 at (a) 100 K and (b) 100K – 400 K (*G(r)* are translated).

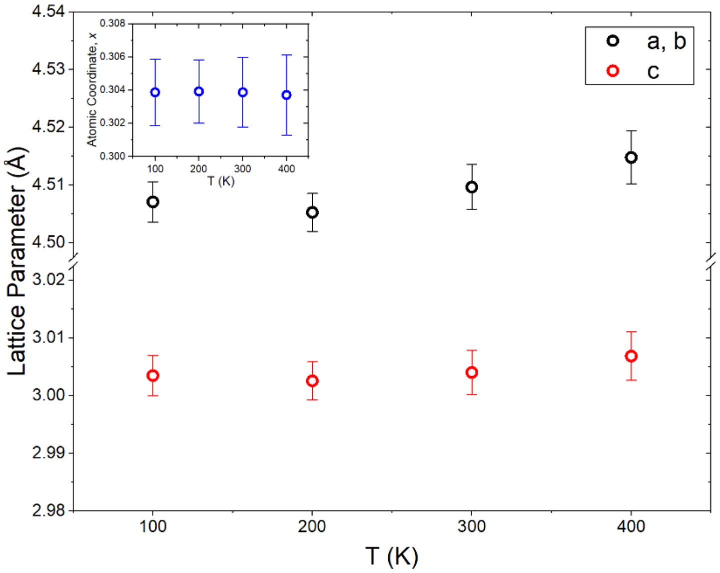

Figure 43: Temperature dependence of the lattice parameters for MgD_2 from total neutron scattering measurements. The atomic coordinates relating to the *x*-coordinate for the deuterium sites is shown in the inset.

While the PDF measurements shown in Figure 42 for MgD_2 are sufficient for a structural investigation, a signal was observed in the measurements arising from the presence of protium (not deuterium) in the sample, as described in Section 5.2.1. The presence of protium created large incoherent backgrounds in the diffraction patterns. This could be a reason why there are intensity mismatches in the low-*r* region of the pattern. The source of the hydrogen is most likely leftover precursor chemicals used to synthesize the MgD_2, i.e. anthracene and protonated solvents. Attempts were made to remove the remaining impurities by heating the sample under vacuum. FTIR measurements showed a decrease in the signal arising from the solvents following the heat treatment. However, this process appears to have drastically changed the sample. The PDF for MgD_2 at T = 100 K is shown in Figure 44. Clearly, there are major disagreements with the calculated model, especially in the low-*r* region. However, the global structure above approximately 20 Å is still relatively well described. The NPD pattern before and after the heat treatment at T = 100 K is shown in Figure 44b. The Bragg peaks appear to be exceptionally broadened following this heat treatment. In addition, there appears to be extra peaks that emerge, most notably at d = 2.1 Å. The heat treatment under vacuum likely decomposed parts of the sample in a non-uniform manner. This would cause a distribution of lattice parameters across the sample which broadens the peaks. A purer sample for neutron diffraction investigations would need to be synthesized in a different manner, or by using the same process used here with completely deuterated reactants, which may be cost prohibitive.

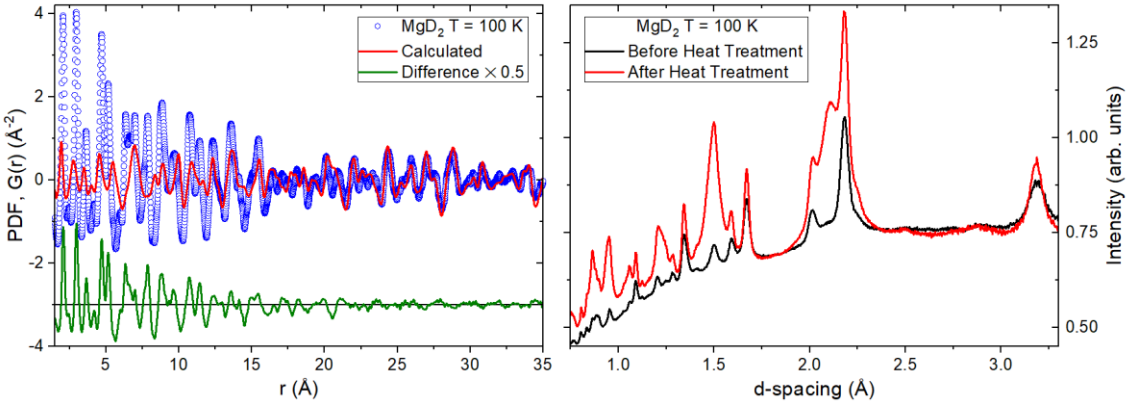

Figure 44: (a) PDF G(r) measured at NOMAD for the heat treated MgD_2 sample at T = 100 K. (b) NPD patterns at T = 100 K for the MgD_2 sample before and after the heat treatment. Patterns were scaled for clarity.

8.2 Hydrogen Dynamics

8.2.1 Quasielastic Neutron Scattering

An elastic scan was measured at HFBS for MgH_2 over a temperature range from T = 70 K – 525 K. Typical Debye-Waller behavior is observed over the entire temperature range, as indicted as a gradual decrease in the elastic intensity. There is no indication of the onset of observable hydrogen dynamics on the timescale of the instrument (HFBS) up to 525 K. The sample was measured in a closed sample container, which limited measurements to 525 K, since higher temperatures would risk sample decomposition and over-pressurizing the sample container. A longer QENS measurement at 525 K showed no quasielastic broadening.

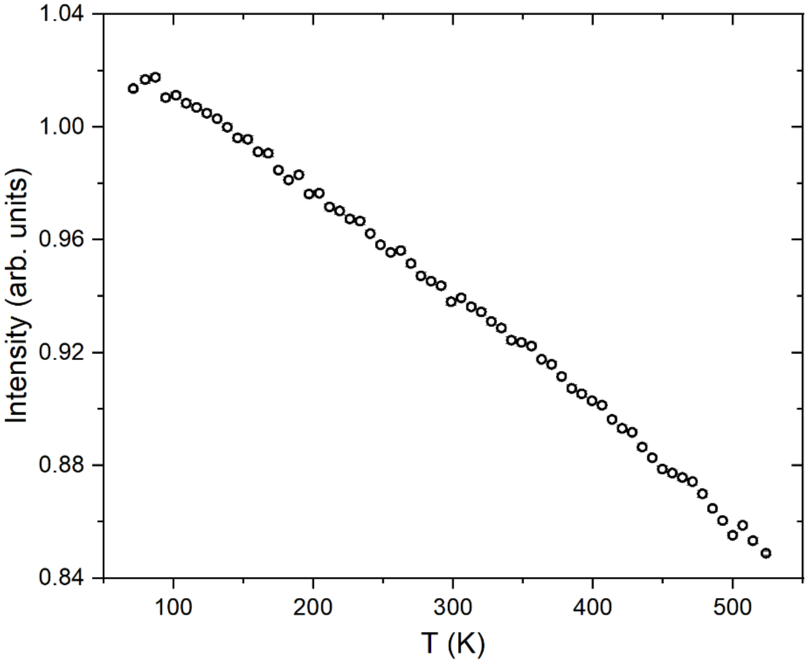

Figure 45: Elastic scan for MgH_2 from 70 K – 525 K.

Longer QENS measurements were performed at BASIS for T = 553 K, 573 K, 593 K, 613 K, and 633 K. The QENS spectra at T = 593 K and the resolution function measured at room temperature are displayed in Figure 46 for Q = 1.3 $Å^{-1}$. No appreciable quasielastic broadening was observed at any of the measured temperatures. Sample decomposition began during the 613 K measurement, as detected by a strong decrease in the neutron count rate and spectral intensity. The fact that we do not observe a quasielastic signal demonstrates that hydrogen transport in MgH_2 is notoriously sluggish, which significantly hinders its potential for many applications. These results indicate that no appreciable diffusion occurs leading up to the sudden decomposition above 600 K. Any diffusion that occurs is likely too slow to be observed at a current QENS instrument, but may be observable using other techniques, such as EIS. This also highlights the strength of the covalent Mg-H bonds in MgH_2.

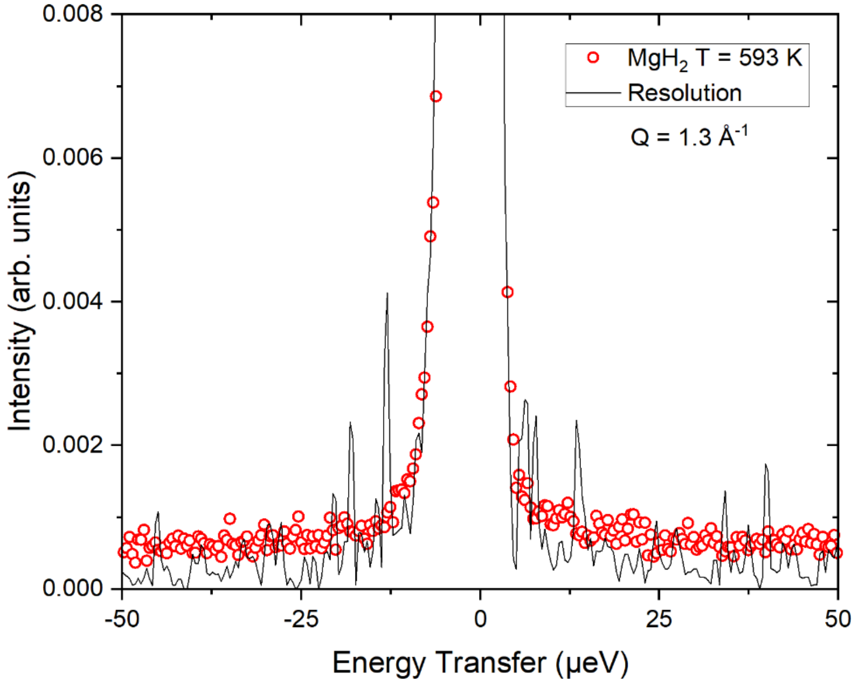

Figure 46: QENS spectra measured at BASIS for MgH_2 at T = 593 K and Q = 1.3 $Å^{-1}$.

8.2.2 Vibrational Density of States (INS)

INS spectra for CaH_2 were measured over a temperature range from T = 5 K to 620 K in MgH_2, as displayed in Figure 47. As expected, the INS spectra modes are different compared to BaH_2 and CaH_2 due to the different crystal structure. The vibrational DOS has been investigated with INS and *ab-initio* modeling previously.[50-52] Again, the INS spectra is heavily weighted towards hydrogen vibrations. At 5 K, the spectra consists of acoustic modes below 40 meV and optical modes between 40 meV – 190 meV. The first feature is a double peak with strong intensity followed by a shoulder at higher energies. The double peak is at 70 meV and 78 meV while the shoulder is at roughly 92 meV. This is followed by a band of peaks between 105 meV – 190 meV. The first peak is located at 124 meV and has a shoulder located around 134 meV. This is followed by two more broad peaks at 148 meV and 175 meV. All the optical modes described here, except for the last one centered at 175 meV, are due to single phonon mode contributions. The peak at 175 meV is a combination of both one- and two-phonon modes. Above this, notably the peak centered at 250 meV, are due to multi-phonon contributions. The grouping of modes centered around 70 meV are due to the H-Mg-H wagging motion while the higher energy peaks between 100 meV – 200 meV are mainly due to bending and stretching modes.[98] The lower end of this band corresponds to the bending modes while the higher end relates to the stretching modes. Modes in the center of the band correspond to a hybrid of the bending-stretching modes.

The temperature dependence of the vibrational modes shows the expected behavior of a gradual broadening and reduction in intensity from 5 K to 580 K. However, there clearly are excess intensities still visible in the 580 K measurement, a feature which disappears by the next measurement at 600 K. Therefore, the hydrogen is released from the sample (decomposed) suddenly around 580 – 600 K. This generally agrees with the decomposition temperatures from other investigations.[9, 50, 99] The decomposition temperatures in metal hydrides are known to vary significantly due to many factors including phase purity, hydrogen concentration, particle size, etc. For example, the reported decomposition temperatures for MgH_2 can be found to range from roughly 550 K to 623 K.[9, 50, 99] After the sample decomposed, the detected scattered neutron count rate at VISION decreased significantly due to the hydrogen release and the INS spectra did not recover upon cooling to room temperature, verifying that the sample decomposed.

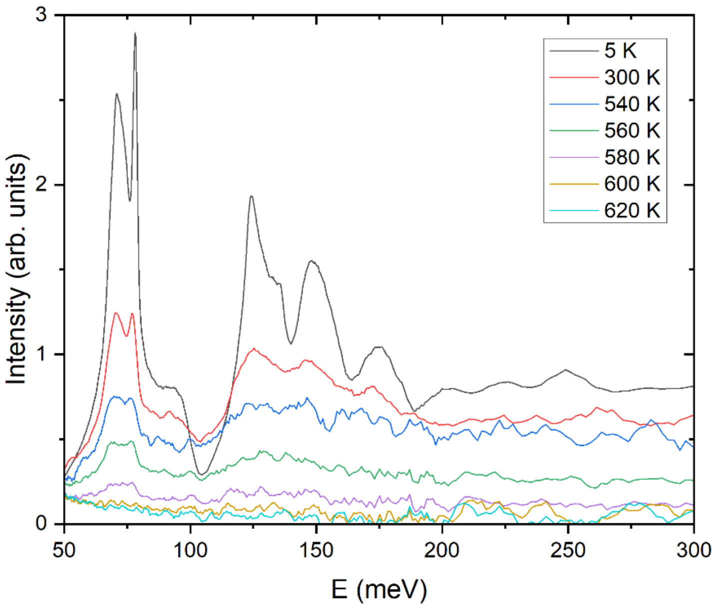

Figure 47: INS spectra from 5 K to 620 K for MgH_2 measured at VISION. Intensities are translated for clarity.

8.3 MgH_2 Summary of Results

The structure of MgD_2 was investigated using NPD and total neutron scattering. The experimental data is well described using the tetragonal rutile structure for both the local and global structures. No phase transitions were observed and only minor changes in the lattice parameters and atomic coordinates occurred. The atomic displacement parameters assumed modest values of U_{11} = 0.033 Å^2 and U_{33} = 0.017 Å^2 at T = 400 K, indicating that the deuterium atoms are tightly bound up to 400 K. The diffusion of hydrogen was probed using QENS at elevated temperatures. An elastic window scan and longer QENS measurements did not reveal any appreciable diffusive motions on the timescale of the instrument. This is not completely surprising considering the notorious reputation for sluggish hydrogen transport in MgH_2. The hydrogen does not appear to diffuse significantly preceding the sudden decomposition around 600 K. Lastly, the vibrational DOS were investigated using INS from 5 K to 620 K. The energies of the modes at 5 K agree with previous reports and the vibrational modes were found to gradually broaden and decrease in intensity until sample decomposition at 600 K.

9 CONCLUSIONS AND FUTURE OUTLOOK

This work used neutron scattering techniques to investigate the structure and dynamics of three different alkaline earth metal hydrides: BaH_2, CaH_2, and MgH_2. These materials were studied in extreme environments, including low- and high-temperatures and under high-pressures. The diffraction and total neutron scattering studies focused on characterizing the temperature and pressure evolution of the crystal structure, both globally and locally. Structural phase transitions of first and second order nature were observed and deuterium positions were determined. Quasielastic neutron scattering was used to investigate the diffusive motions of hydride ions through the crystal structures. Atomic scale details regarding the diffusion pathways and energy landscape were uncovered, leading to a greater understanding of hydrogen transport in these materials. The temperature dependence of the vibrational density of states and its relation to the hydrogen release and bonding was determined using inelastic powder neutron scattering.

9.1 Structure Summary

Both BaD_2 and CaD_2 crystallize in the orthorhombic cotunnite structure at ambient conditions. This structure resembles a hexagonal close packed lattice (hcp), but the cation positions deviate slightly from the proper hcp positions. This causes the neighboring anionic polyhedra surrounding the cations to be tilted 25° with respect to each other.

At T = 775 K, the cotunnite phase of BaD_2 begins transitioning into a higher symmetry hexagonal phase with the Ni_2In-type structure. NPD measurements showed that both the orthorhombic and hexagonal phases exist simultaneously until the transition is completed around 850 K – 900 K. Changes in the atomic coordinates are observed for the Ba, D(1), and D(2) sites preceding the phase transition. In the hexagonal phase, the cations are now positioned on the proper hcp positions and the tilt is removed. The total neutron scattering results in our investigation showed that the local structure largely remains the same in this structure following the transition, but that there is disorder introduced in the intermediate region bridging the gap between the local and global structure. This disordered intermediate transition region corresponds to PDF length scales of roughly 6 Å – 13 Å. We attribute this disorder to a degree of reorientational freedom with respect to the anionic polyhedra. While the global structure suggests the tilt is removed, it is possible that these domains can dynamically assume various tilt configurations. This correlated motion is averaged out over the length of 2 – 3 unit cells to yield the highly ordered, global hexagonal structure. These dynamic fluctuations cause the D(1) site to be split in the structure, where the deuterium atoms deviate from the high symmetry 2d site and instead reside on the lower symmetry 4f sites. Dynamic fluctuations of this type can be beneficial to the hydrogen diffusion process by decreasing the hydrogen jump lengths and reducing the energy barriers by increasing the free volume for the hydrogen to diffuse through.

The orthorhombic to hexagonal phase transition observed in BaD_2 does not occur with temperature in CaD_2. Rather, we detected the existence of second order transitions occurring in this structure with PDF analysis. There is a noticeable change in the atomic positions with temperature for both the Ca and D(1) sites between 600 – 700 K. This minor structural modification roughly corresponds to the temperature range in which a change in the activation energy observed in previous EIS measurements.[93] Upon additional heating, changes are observed in all the atomic sites beginning around 800 K, which agrees with previous DTA measurements for a second order transition. The Ca and D(2) sites appear to be most affected by this structural change.

The final metal hydride investigated in this work is MgD_2, which does not crystallize in the cotunnite structure at ambient conditions and instead assumes the tetragonal rutile structure. The bonding in this material is covalent-like, which causes the hydrogen to be bound tighter to the metal atoms when compared to the ionic nature of the HAEH bonds. The observed PDF patterns over the temperature range of 100 K – 400 K are well described using the tetragonal rutile structure for both the local and global structures. No phase transitions were observed and only minor changes in the lattice parameters and atomic coordinates occurred. The atomic displacement parameters assumed the modest values of U_{11} = 0.033 Å^2 and U_{33} = 0.017 Å^2 at T = 400 K, supporting the reasoning that the deuterium atoms are tightly bound in this structure up to 400 K.

9.2 Dynamics Summary

Quasielastic neutron scattering was used to investigate the atomic scale hydrogen diffusion mechanism in these materials. The three hydrides chosen for this investigation possess distinct hydrogen transport properties: BaH_2 exhibits fast ionic conduction, CaH_2 has intermediate hydrogen kinetics, and the transport in MgH_2 is extremely sluggish.

The temperature dependent study of BaH_2 showed that the hydride ions undergo jump diffusion between various hydrogen lattice sites, as explained by the Chudley-Elliott jump diffusion model. We have determined the preferred jumps in the lattice for both the orthorhombic and hexagonal phases, with each phase showing distinct dynamics. In the orthorhombic phase, two distinct jump lengths of approximately 3.6 Å and 4.2 Å were found. The first one (3.6 Å) corresponds to a distance between H(2)-H(2) sites. The second one (4.2 Å) corresponds to distances between both H(2)-H(2) and H(1)-H(1) sites. Despite the shorter distance (3.1 Å) between H(1)-H(2) sites, such jumps are not observed in the QENS measurements. Following the phase transition, jump lengths were found to be around 3.1 Å in the hexagonal phase, which corresponds to jumps between H(1)-H(2) sites. The phase transition unlocks the previously restricted H(1)-H(2) jumps in the orthorhombic phase. This change allows the hydrogen to diffuse efficiently through 3.1 Å jumps with an activation energy of 418 meV, which is significantly lower than 512 meV in the orthorhombic phase. The jump rate increases by an order of magnitude upon the phase transition, promoting the faster diffusion. The dynamic fluctuations observed in our structural study cause the D(1) site to be split, a feature that is key for unlocking the fast hydrogen diffusion in the hexagonal phase.

The QENS investigation on CaH_2 began with an elastic scan that showed a sharp discontinuity in the elastic intensity around 680 K. This type of feature is typically indicative of a phase transition. This feature occurs in the same temperature range as the structural changes in the Ca and D(1) sites observed in our PDF study. In addition, the feature at 680 K is close to the temperature at which a change in the activation energy was observed a previous EIS study. The elastic intensity increased at 680 K, which suggests that the hydrogen dynamics initially slow down following this transition. Longer QENS measurements at T = 800 K did not show appreciable quasielastic broadening. While EIS shows that the hydrogen is diffusing at this temperature, the motion is too slow to be seen with QENS. However, the elastic scan suggests that diffusion would likely be observable above 800 K because the elastic intensity begins to decrease more rapidly approaching this temperature.

For the QENS investigation of MgH_2, an elastic scan was measured from T = 70 K – 525 K. Typical Debye-Waller behavior was observed over the entire temperature range, as indicted as a gradual decrease in the elastic intensity. There is no indication of the onset of observable hydrogen dynamics on the timescale of the instrument (HFBS) up to 525 K. Longer QENS measurements were performed at BASIS between T = 553 K – 633 K. No quasielastic broadening was observed and the sample began decomposing during the 613 K measurement. The hydrogen in MgH_2 does not appear to diffuse significantly preceding the sudden decomposition around 600 K. This is not surprising considering the notorious reputation for sluggish hydrogen transport in MgH_2.

Inelastic powder neutron scattering was employed to measure the vibrational density of states, which yields information about the bonding, hydrogen release mechanism, and the vibrational energies. While most INS investigations in metal hydrides are conducted at low temperatures, our measurements covered a wide range from 5 K to 850 K. In all three hydrides, the weakening of the hydrogen bonds was observed as a gradual decrease in the intensity and a softening of the vibrational modes.

Due to the existence of two distinct hydrogen sites in the cotunnite structure of BaH_2 and CaH_2, the vibrational contributions of these two sites can be separated since they occur at different energies. The modes associated with the H(1) and H(2) sites had a similar temperature dependence, which suggests that both sites behave similarly and contribute equally to the ionic conduction. An argument could be made that the H(2) site releases at a slightly lower temperature than the H(1) sites in CaH_2. The INS spectra of both materials are similar, but the modes in CaH_2 are shifted to higher energies by ~15 – 20 meV. This suggests that the bonds in CaH_2 are notably stronger than those in BaH_2. Further evidence of this is the temperature evolution of the modes. In BaH_2, the modes are smeared out and almost completely merged with the background by the measurement at 450 K. Likewise, the 600 K measurement for CaH_2 shows this similar feature. The hydrogen release is ultimately observed around 600 K for BaH_2 and 700 K for CaH_2. This is the temperature in which the hydrogen begins to readily diffuse through the system. While this motion was observed with QENS at 600 K for BaH_2, it was not observed up to 800 K for CaH_2. In summary, the lattice dynamics in these two materials behave in a similar manner with temperature, but the behavior is shifted to higher temperatures by roughly 100 – 150 K in CaH_2 when compared to BaH_2.

On the other hand, the lattice dynamics are notably different in MgH_2. The modes remain rather sharp and distinct up to 580 K, indicating that the hydrogen remains tightly bound to the Mg atoms up to this temperature. The modes disappear completely at 600 K and the resulting decrease in the neutron count rate detected at VISION indicated the evolution of hydrogen from the sample (sample decomposed). This shows that the hydrogen does not release and diffuse significantly before sample decomposition occurs, which is the opposite of what is observed in the HAEHs.

9.3 High Pressure Summary

In addition to the temperature dependent studies described above, the structure and dynamics of barium hydride was investigated under high pressure. The same phase transition (orthorhombic to hexagonal) was observed over a wide pressure range (P = 1.3 – 4.9 GPa). Both the low pressure orthorhombic and high pressure hexagonal phases are well described by the cotunnite and Ni_2In-type models, respectively. Recent reports suggest that ionic conduction in BaH_2 increases with pressure in the hexagonal phase.[16] We performed high pressure QENS measurements on BaH_2 up to a maximum pressure of 7.1 GPa. Our preliminary results show that there is a quasielastic signal that increases with pressure. This signal has a HWHM broadening of approximately 39 ± 8 μeV at 7.1 GPa. To our knowledge, this is the highest pressure currently achieved in a QENS experiment. We plan to expand this study in future experiments to obtain better statistics for a proper Q-dependent investigation to unveil the diffusive pathways in this high-pressure phase. It would be interesting to observe how the pressure dependent diffusion process compares to the temperature dependent dynamics.

9.4 Concluding Remarks and Future Suggestions

These results have interesting implications for the lighter weight hydrides, especially ones that crystallize in the cotunnite structure at ambient conditions, such as CaH_2 and SrH_2. The calcium hydride system is an ideal candidate for future work in which attempts should be focused on inducing a structural phase transition from the cotunnite phase into the Ni_2In-type phase with temperature, perhaps through doping techniques. These results suggest that even small modifications of the structure in CaH_2 can have an impact on the hydrogen dynamics, as observed in the discontinuity in the elastic scan and the previous EIS results. This phase transition has already been observed to occur under pressure in this material around 15 GPa.[84, 85] If successful, this could greatly improve the hydrogen transport properties in calcium hydride, making it better suited for energy related applications. The same outlook is applicable to the MgH_2 system, where an induced phase transition could have the potential to improve the hydrogen transport properties. With pressure, MgH_2 transforms into the cotunnite structure around 17 GPa.[97] Therefore, MgH_2 may behave similar to the HAEHs at elevated pressures in the cotunnite phase. However, it is still likely that the hydrogen transport would remain too slow for most applications.

This work improves the current understanding of how the crystal structure affects the solid-state diffusion of hydride ions in alkaline earth-based metal hydride systems. These results serve to demystify the role that a structural phase transition plays in transforming a solid-state material with modest kinetics into a fast-ionic conductor of hydrogen. Even small modifications of the lattice parameters and atomic coordinates were found to influence the hydrogen dynamics. The knowledge gained here sheds light on the intricate relationship between the atomic structure and the corresponding diffusion mechanism in alkaline earth hydrides, which can be applied to understand and further advance the hydrogen transport properties in other metal hydride systems.

LIST OF REFERENCES

1. Energy Consumption by Sector. U.S. Energy Information Administration: 2018.
2. Schlapbach, L.; Zuttel, A., Hydrogen-storage materials for mobile applications. *Nature* **2001,** *414* (6861), 353-358.
3. FreedomCAR and Fuel Partnership 2010 Highlights of Technical Accomplishments. https://www.energy.gov/sites/prod/files/2014/02/f8/2010_fcfp_accomplishments_rpt.pdf.
4. 2018 Toyota Mirai. https://www.toyota.com/content/ebrochure/2018/mirai_FuelCellTech.pdf.
5. Klebanoff, L. E.; Pratt, J. W.; Leffers, C. M.; Sonerholm, K. T.; Escher, T.; Burgard, J.; Ghosh, S., Comparison of the greenhouse gas and criteria pollutant emissions from the SF-BREEZE high-speed fuel-cell ferry with a diesel ferry. *Transportation Research Part D: Transport and Environment* **2017,** *54*, 250-268.
6. Reilly, J. J.; Sandrock, G. D., Hydrogen Storage in Metal Hydrides. *Scientific American* **1980,** *242* (2), 118-131.
7. Lototskyy, M. V.; Tolj, I.; Pickering, L.; Sita, C.; Barbir, F.; Yartys, V., The use of metal hydrides in fuel cell applications. *Progress in Natural Science: Materials International* **2017,** *27* (1), 3-20.
8. Sakintuna, B.; Lamari-Darkrim, F.; Hirscher, M., Metal hydride materials for solid hydrogen storage: A review. *International Journal of Hydrogen Energy* **2007,** *32* (9), 1121-1140.
9. Webb, C. J., A review of catalyst-enhanced magnesium hydride as a hydrogen storage material. *Journal of Physics and Chemistry of Solids* **2015,** *84*, 96-106.
10. Van Houten, R.; Bartram, S., The preparation and crystallographic characterization of two new types of ternary metal hydrides. *Metallurgical Transactions* **1971,** *2* (2), 527-530.
11. Nicholson, K. M.; Sholl, D. S., First-Principles Screening of Complex Transition Metal Hydrides for High Temperature Applications. *Inorganic Chemistry* **2014,** *53* (22), 11833-11848.
12. Gil, A.; Medrano, M.; Martorell, I.; Lázaro, A.; Dolado, P.; Zalba, B.; Cabeza, L. F., State of the art on high temperature thermal energy storage for power generation. Part 1—Concepts, materials and modellization. *Renewable and Sustainable Energy Reviews* **2010,** *14* (1), 31-55.
13. Verbraeken, M. C.; Cheung, C.; Suard, E.; Irvine, J. T. S., High H^- ionic conductivity in barium hydride. *Nature Materials* **2014,** *14*, 95.
14. Holtz, R. L.; Imam, M. A., Hydrogen storage characteristics of ball-milled magnesium-nickel and magnesium-iron alloys. *Journal of Materials Science* **1999,** *34* (11), 2655-2663.
15. George, L.; Saxena, S. K., Structural stability of metal hydrides, alanates and borohydrides of alkali and alkali- earth elements: A review. *International Journal of Hydrogen Energy* **2010,** *35* (11), 5454-5470.

16. Zhang, X.; Wang, X.; Wang, Q.; Ma, X.; Liu, C.; Li, P.; Liu, C.; Han, Y.; Ma, Y.; Gao, C., Hydride ion (H-) transport behavior in barium hydride under high pressure. *Physical Chemistry Chemical Physics* **2018,** *20* (13), 8917-8923.
17. Verbraeken, M. C.; Suard, E.; Irvine, J. T. S., Structural and electrical properties of calcium and strontium hydrides. *Journal of Materials Chemistry* **2009,** *19* (18), 2766-2770.
18. M. Ramzan, T. H., and R. Ahuja, Hydrogen diffusion in bulk and nanoclusters of MgH2 and the role of catalysts on the basis of ab initio molecular dynamics. *Applied Physics Letters* **2009,** *94* (22), 221910.
19. Kadir, K.; Noréus, D., Synthesis and Structural Determination of a New Ternary Hydride Ba2MgH6*. In *Zeitschrift für Physikalische Chemie*, 1993; Vol. 179, p 243.
20. Gingl, F.; Bonhomme, F.; Yvon, K.; Fischer, P., Tetracalcium trimagnesium tetradecahydride, Ca4Mg3H14: the first ternary alkaline earth hydride. *Journal of Alloys and Compounds* **1992,** *185* (2), 273-278.
21. Lovesey, S. W., *Theory of neutron scattering from condensed matter*. Clarendon Press: United Kingdom, 1984.
22. Squires, G. L., *Introduction to the Theory of Thermal Neutron Scattering*. 3 ed.; Cambridge University Press: Cambridge, 2012.
23. Sears, V. F., Neutron scattering lengths and cross sections. *Neutron News* **1992,** *3* (3), 26-37.
24. Hempelmann, R., *Quasielastic Neutron Scattering and Solid State Diffusion*. Oxford University Press: Oxford, 2000.
25. Egami, T.; Billinge, S. J. L., *Underneath the Bragg Peaks : Structural Analysis of Complex Materials*. Elsevier Science & Technology: London, UNITED KINGDOM, 2012.
26. Farrow, C. L.; Juhas, P.; Liu, J. W.; Bryndin, D.; Božin, E. S.; Bloch, J.; Proffen, T.; Billinge, S. J. L., PDFfit2 and PDFgui: computer programs for studying nanostructure in crystals. *Journal of Physics: Condensed Matter* **2007,** *19* (33), 335219.
27. Mamontov, E.; Herwig, K. W., A time-of-flight backscattering spectrometer at the Spallation Neutron Source, BASIS. *Review of Scientific Instruments* **2011,** *82* (8), 085109.
28. Seeger, P. A.; Daemen, L. L.; Larese, J. Z., Resolution of VISION, a crystal-analyzer spectrometer. *Nuclear Instruments and Methods in Physics Research Section A: Accelerators, Spectrometers, Detectors and Associated Equipment* **2009,** *604* (3), 719-728.
29. Calder, S.; An, K.; Boehler, R.; Cruz, C. R. D.; Frontzek, M. D.; Guthrie, M.; Haberl, B.; Huq, A.; Kimber, S. A. J.; Liu, J.; Molaison, J. J.; Neuefeind, J.; Page, K.; Santos, A. M. d.; Taddei, K. M.; Tulk, C.; Tucker, M. G., A suite-level review of the neutron powder diffraction instruments at Oak Ridge National Laboratory. *Review of Scientific Instruments* **2018,** *89* (9), 092701.
30. Neuefeind, J.; Feygenson, M.; Carruth, J.; Hoffmann, R.; Chipley, K. K., The Nanoscale Ordered MAterials Diffractometer NOMAD at the Spallation

Neutron Source SNS. *Nuclear Instruments and Methods in Physics Research Section B: Beam Interactions with Materials and Atoms* **2012,** *287*, 68-75.
31. Meyer, A.; Dimeo, R. M.; Gehring, P. M.; Neumann, D. A., The high-flux backscattering spectrometer at the NIST Center for Neutron Research. *Review of Scientific Instruments* **2003,** *74* (5), 2759-2777.
32. Novak, E.; Jalarvo, N.; Gupta, S.; Hong, K.; Förster, S.; Egami, T.; Ohl, M., Dynamics in the Plastic Crystalline Phases of Cyclohexanol and Cyclooctanol Studied by Quasielastic Neutron Scattering. *The Journal of Physical Chemistry B* **2018,** *122* (23), 6296-6304.
33. Arnold, O.; Bilheux, J. C.; Borreguero, J. M.; Buts, A.; Campbell, S. I.; Chapon, L.; Doucet, M.; Draper, N.; Ferraz Leal, R.; Gigg, M. A.; Lynch, V. E.; Markvardsen, A.; Mikkelson, D. J.; Mikkelson, R. L.; Miller, R.; Palmen, K.; Parker, P.; Passos, G.; Perring, T. G.; Peterson, P. F.; Ren, S.; Reuter, M. A.; Savici, A. T.; Taylor, J. W.; Taylor, R. J.; Tolchenov, R.; Zhou, W.; Zikovsky, J., Mantid—Data analysis and visualization package for neutron scattering and μ SR experiments. *Nuclear Instruments and Methods in Physics Research Section A: Accelerators, Spectrometers, Detectors and Associated Equipment* **2014,** *764*, 156-166.
34. Marshall, W. G.; Francis, D. J., Attainment of near-hydrostatic compression conditions using the Paris–Edinburgh cell. *Journal of Applied Crystallography* **2002,** *35* (1), 122-125.
35. Klotz, S.; Strässle, T.; Rousse, G.; Hamel, G.; Pomjakushin, V., Angle-dispersive neutron diffraction under high pressure to 10GPa. *Applied Physics Letters* **2005,** *86* (3), 031917.
36. Bove, L. E.; Klotz, S.; Strässle, T.; Koza, M.; Teixeira, J.; Saitta, A. M., Translational and Rotational Diffusion in Water in the Gigapascal Range. *Physical Review Letters* **2013,** *111* (18), 185901.
37. Klotz, S.; Strässle, T.; Bove, L. E., Quasi-elastic neutron scattering in the multi-GPa range and its application to liquid water. *Applied Physics Letters* **2013,** *103* (19), 193504.
38. Toby, B. H.; Von Dreele, R. B., GSAS-II: the genesis of a modern open-source all purpose crystallography software package. *Journal of Applied Crystallography* **2013,** *46* (2), 544-549.
39. *ICE-MAN, the Integrated Computational Environment-Modeling & Analysis for Neutrons*, Laboratory Director Research and Development funds (LDRD 8237): Oak Ridge National Laboratory.
40. R.T. Azuah, L. R. K., Y. Qiu, P.L.W. Tregenna-Piggott, C.M. Brown, J.R.D. Copley, and R.M. Dimeo, DAVE: A comprehensive software suite for the reduction, visualization, and analysis of low energy neutron spectroscopic data. *J. Res. Natl. Inst. Stan. Technol.* **2009,** *114* (341).
41. Chudley, C. T.; Elliott, R. J., Neutron Scattering from a Liquid on a Jump Diffusion Model. *Proceedings of the Physical Society* **1961,** *77* (2), 353.
42. Bée, M., *Quasielastic Neutron Scattering*. Hilger: Bristol, UK, 1988.

43. Singwi, K. S.; Sjölander, A., Diffusive Motions in Water and Cold Neutron Scattering. *Physical Review* **1960,** *119* (3), 863-871.

44. Hall, P. L.; Ross, D. K., Incoherent neutron scattering functions for random jump diffusion in bounded and infinite media. *Molecular Physics* **1981,** *42* (3), 673-682.

45. Novak, E.; Daemen, L.; Ramirez-Cuesta, A. J.; Cheng, Y. Q.; Smith, R.; Egami, T.; Jalarvo, N., Hydride Ion Diffusion in Barium Hydride Measured with Quasielastic Neutron Scattering. *Submitted* **2020**.

46. McCusker, L. B.; Von Dreele, R. B.; Cox, D. E.; Louer, D.; Scardi, P., Rietveld refinement guidelines. *Journal of Applied Crystallography* **1999,** *32* (1), 36-50.

47. Birch, F., Finite Elastic Strain of Cubic Crystals. *Physical Review* **1947,** *71* (11), 809-824.

48. Luo, W.; Ahuja, R., Ab initio prediction of high-pressure structural phase transition in BaH2. *Journal of Alloys and Compounds* **2007,** *446-447*, 405-408.

49. Smith, J. S.; Desgreniers, S.; Tse, J. S.; Klug, D. D., High-pressure phase transition observed in barium hydride. *Journal of Applied Physics* **2007,** *102* (4), 043520.

50. Kolesnikov, A. I.; Antonov, V. E.; Efimchenko, V. S.; Granroth, G.; Klyamkin, S. N.; Levchenko, A. V.; Sakharov, M. K.; Ren, Y., Neutron spectroscopy of magnesium dihydride. *Journal of Alloys and Compounds* **2011,** *509*, S599-S603.

51. Schimmel, H. G.; Johnson, M. R.; Kearley, G. J.; Ramirez-Cuesta, A. J.; Huot, J.; Mulder, F. M., The vibrational spectrum of magnesium hydride from inelastic neutron scattering and density functional theory. *Materials Science and Engineering: B* **2004,** *108* (1), 38-41.

52. Schimmel, H. G.; Johnson, M. R.; Kearley, G. J.; Ramirez-Cuesta, A. J.; Huot, J.; Mulder, F. M., Structural information on ball milled magnesium hydride from vibrational spectroscopy and ab-initio calculations. *Journal of Alloys and Compounds* **2005,** *393* (1), 1-4.

53. Colognesi, D.; Barrera, G.; Ramirez-Cuesta, A. J.; Zoppi, M., Hydrogen self-dynamics in orthorhombic alkaline earth hydrides through incoherent inelastic neutron scattering. *Journal of Alloys and Compounds* **2007,** *427* (1), 18-24.

54. Colognesi, D.; Zoppi, M., Hydrogen vibrational dynamics in ionic metal hydrides revealed through inelastic neutron scattering. *Notiziario Neutroni E Luce Di Sincrotrone* **2006,** *11* (2).

55. Wu, H.; Zhou, W.; Udovic, T. J.; Rush, J. J.; Yildirim, T., Structure and vibrational spectra of calcium hydride and deuteride. *Journal of Alloys and Compounds* **2007,** *436* (1), 51-55.

56. Morris, P.; Ross, D. K.; Ivanov, S.; Weaver, D. R.; Serot, O., Inelastic neutron scattering study of the vibration frequencies of hydrogen in calcium dihydride. *Journal of Alloys and Compounds* **2004,** *363* (1), 88-92.

57. Maeland, A. J., Vibration Spectra of the Orthorhombic Alkaline ‐ Earth Hydrides by the Inelastic Scattering of Cold Neutrons and by Infrared Transmission Measurements. *The Journal of Chemical Physics* **1970,** *52* (8), 3952-3956.
58. Kofu, M.; Hashimoto, N.; Akiba, H.; Kobayashi, H.; Kitagawa, H.; Tyagi, M.; Faraone, A.; Copley, J. R. D.; Lohstroh, W.; Yamamuro, O., Hydrogen diffusion in bulk and nanocrystalline palladium: A quasielastic neutron scattering study. *Physical Review B* **2016,** *94* (6), 064303.
59. Dhawan, L. L.; Prakash, S., Optical-phonon-assisted hydrogen diffusion in metal hydrides. *Physical Review B* **1983,** *28* (12), 7294-7307.
60. Dhawan, L. L.; Prakash, S., Acoustic-phonon-assisted hydrogen diffusion in metal hydrides. *Physical Review B* **1984,** *29* (6), 3661-3670.
61. Teichler, H.; Seeger, A., One-phonon processes in phonon-assisted tunnelling jumps at low temperatures. *Physics Letters A* **1981,** *82* (2), 91-94.
62. Itskovich, I. F.; Sorbello, R. S., Phonon-assisted diffusion and electromigration of light interstitials in metals. *Physical Review B* **1992,** *45* (2), 718-727.
63. Sato, T.; Ramirez-Cuesta, A. J.; Daemen, L.; Cheng, Y. Q.; Tomiyasu, K.; Takagi, S.; Orimo, S., Hydrogen release reactions of Al-based complex hydrides enhanced by vibrational dynamics and valences of metal cations. *Chemical Communications* **2016,** *52* (79), 11807-11810.
64. Pyle, D. S.; Gray, E. M.; Webb, C. J., A sieverts apparatus for measuring high-pressure hydrogen isotherms on porous materials. *International Journal of Hydrogen Energy* **2017,** *42* (31), 20111-20119.
65. Ekkehard, B.; Borislav, B.; Nikolaus, J.; Klaus, S.; Bernd, S.; Joachim, T.; Uwe, W.; Ursula, W.; Shijan, L., Active Magnesium from Catalytically Prepared Magnesium Hydride or from Magnesium Anthracene and its Uses in the Synthesis. *Chemische Berichte* **1990,** *123* (7), 1517-1528.
66. Wiberg, E.; Bauer, R., Der Magnesiumwasserstoff MgH2. *Chemische Berichte* **1952,** *85* (6), 593-605.
67. Bogdanović, B.; Liao, S.-t.; Schwickardi, M.; Sikorsky, P.; Spliethoff, B., Catalytic Synthesis of Magnesium Hydride under Mild Conditions. *Angewandte Chemie International Edition in English* **1980,** *19* (10), 818-819.
68. Gingl, F.; Hewat, A.; Yvon, K., Orthorhombic Ba6Mg7H26: a new fluoride-related ternary alkaline earth hydride. *Journal of Alloys and Compounds* **1997,** *253-254*, 17-20.
69. Gingl, F.; Yvon, K.; Fischer, P., Strontium magnesium tetrahydride (SrMgH4): a new ternary alkaline earth hydride. *Journal of Alloys and Compounds* **1992,** *187* (1), 105-111.
70. Gingl, F.; Yvon, K.; Fischer, P., Monoclinic Sr2Mg3H10 with Ba2Ni3F10-type structure. *Journal of Alloys and Compounds* **1994,** *206* (1), 73-75.
71. Gingl, F.; Yvon, K.; Vogt, T., Synthesis and crystal structure of BaMgH4: A centrosymmetric variant of SrMgH4. *Journal of Alloys and Compounds* **1997,** *256* (1), 155-158.

72. Gingl, F.; Yvon, K.; Zolliker, M., The Ba analogue of Sr2Mg3H10. *Journal of Alloys and Compounds* **1994,** *216* (1), L1-L3.
73. Predel, B., Ba-Mg (Barium-Magnesium). In *B-Ba – C-Zr*, Madelung, O., Ed. Springer Berlin Heidelberg: Berlin, Heidelberg, 1992; pp 1-3.
74. Predel, B., Ca - Mg (Calcium - Magnesium). In *B - Ba … Cu - Zr: Supplement to Subvolumes IV/5B, IV/5C and IV/5D*, Predel, B., Ed. Springer Berlin Heidelberg: Berlin, Heidelberg, 2012; pp 164-165.
75. Peterson, D. T.; Indig, M., The Barium-Barium Hydride Phase System. *Journal of the American Chemical Society* **1960,** *82* (21), 5645-5646.
76. Bronger, W.; Chi-Chien, S.; Müller, P., Die Kristallstruktur von Bariumhydrid, ermittelt über Neutronenbeugungsexperimente an BaD2. *Zeitschrift für anorganische und allgemeine Chemie* **1987,** *545* (2), 69-74.
77. G. Snyder, H. B., A. Simon, Crystal structure of barium dihydride, BaH2. In *Zeitschrift für Kristallographie - Crystalline Materials*, 1994; Vol. 209, p 458.
78. Vegas, A.; Grzechnik, A.; Syassen, K.; Loa, I.; Hanfland, M.; Jansen, M., Reversible phase transitions in Na2S under pressure: a comparison with the cation array in Na2SO4. *Acta Crystallographica Section B* **2001,** *57* (2), 151-156.
79. Leger, J. M.; Haines, J.; Atouf, A.; Schulte, O.; Hull, S., High-pressure x-ray- and neutron-diffraction studies of BaF2: An example of a coordination number of 11 in AX2 compounds. *Physical Review B* **1995,** *52* (18), 13247-13256.
80. Sau, K.; Ikeshoji, T.; Kim, S.; Takagi, S.; Akagi, K.; Orimo, S.-i., Reorientational motion and Li+-ion transport in Li2B12H12 system: Molecular dynamics study. *Physical Review Materials* **2019,** *3* (7), 075402.
81. Skripov, A. V.; Soloninin, A. V.; Babanova, O. A.; Skoryunov, R. V., Nuclear magnetic resonance studies of atomic motion in borohydride-based materials: Fast anion reorientations and cation diffusion. *Journal of Alloys and Compounds* **2015,** *645*, S428-S433.
82. Verdal, N.; Udovic, T. J.; Stavila, V.; Tang, W. S.; Rush, J. J.; Skripov, A. V., Anion Reorientations in the Superionic Conducting Phase of Na2B12H12. *The Journal of Physical Chemistry C* **2014,** *118* (31), 17483-17489.
83. Peterson, D. T.; Colburn, R. P., The Strontium-Strontium Hydride Phase System1. *The Journal of Physical Chemistry* **1966,** *70* (2), 468-471.
84. Tse, J. S.; Klug, D. D.; Desgreniers, S.; Smith, J. S.; Flacau, R.; Liu, Z.; Hu, J.; Chen, N.; Jiang, D. T., Structural phase transition in CaH2 at high pressures. *Physical Review B* **2007,** *75* (13), 134108.
85. Li, B.; Li, Y.; Yang, K.; Cui, Q.; Ma, Y.; Zou, G., Raman evidence of a new high-pressure phase in calcium hydride. *Journal of Physics: Condensed Matter* **2007,** *19* (22), 226205.
86. Smith, J. S.; Desgreniers, S.; Klug, D. D.; Tse, J. S., High-density strontium hydride: An experimental and theoretical study. *Solid State Communications* **2009,** *149* (21), 830-834.

87. Kinoshita, K.; Nishimura, M.; Akahama, Y.; Kawamura, H., Pressure-induced phase transition of BaH2 : Post Ni2In phase. *Solid State Communications* **2007,** *141* (2), 69-72.
88. Weir, S. T.; Vohra, Y. K.; Ruoff, A. L., High-pressure phase transitions and the equations of state of BaS and BaO. *Physical Review B* **1986,** *33* (6), 4221-4226.
89. Liu, L.-g.; Bassett, W. A., Effect of pressure on the crystal structure and the lattice parameters of BaO. *Journal of Geophysical Research (1896-1977)* **1972,** *77* (26), 4934-4937.
90. Novak, E.; Haberl, B.; Daemen, L.; Molaison, J.; Egami, T.; Jalarvo, N., Pressure-Induced Structural Phase Transition in Barium Hydride Studied by Neutron Scattering. *Submitted* **2020**.
91. Osti, N. C.; Haberl, B.; Jalarvo, N.; Boehler, R.; Molaison, J. J.; Goyette, R. J.; Mamontov, E., Dynamics of a room temperature ionic liquid under applied pressure. *Chemical Physics* **2020,** *530*, 110628.
92. Bergsma, J.; Loopstra, B. O., The crystal structure of calcium hydride. *Acta Crystallographica* **1962,** *15* (1), 92-93.
93. Verbraeken, M. C. Doped Alkaline Earth (Nitride) Hydrides. University of St. Andrews, 2009.
94. Zachariasen, W. H.; Holley, C. E.; Stamper, J. F., Jnr, Neutron diffraction study of magnesium deuteride. *Acta Crystallographica* **1963,** *16* (5), 352-353.
95. Huot, J.; Liang, G.; Boily, S.; Van Neste, A.; Schulz, R., Structural study and hydrogen sorption kinetics of ball-milled magnesium hydride. *Journal of Alloys and Compounds* **1999,** *293-295*, 495-500.
96. Bortz, M.; Bertheville, B.; Böttger, G.; Yvon, K., Structure of the high pressure phase γ-MgH2 by neutron powder diffraction. *Journal of Alloys and Compounds* **1999,** *287* (1), L4-L6.
97. Moriwaki, T.; Akahama, Y.; Kawamura, H.; Nakano, S.; Takemura, K., Structural Phase Transition of Rutile-Type MgH2 at High Pressures. *Journal of the Physical Society of Japan* **2006,** *75* (7), 074603.
98. Cheng, Y., Personal Communication. 2020.
99. Stander, C. M., Kinetics of decomposition of magnesium hydride. *Journal of Inorganic and Nuclear Chemistry* **1977,** *39* (2), 221-223.
100. Molaison, J. J.; Haberl, B.; Frontzek, M.; Novak, E.; Goldsby, D.; Anderson, D. C.; Elliott, A., 3D-printed B_4C Collimation for Neutron Pressure Cells. *In Preparation for Review of Scientific Instruments* **2020**.

APPENDIX

A.1 Quasielastic Neutron Scattering Experimental Details

The QENS experiments consisted of five different beam times (excluding SPHERES): four at BASIS (CCR, furnace, two in high pressure PE cell) and one at HFBS (CCR). Technical details for each experiment are included in this section.

A.1.1 BASIS Experiments

The first BASIS experiment occurred in Sept. 2016 using a CCR. This experiment was performed before I joined the group and some technical details are unknown. Samples were loaded into aluminum foil and formed into a packet of annular geometry to reduce multiple scattering effects. Annular aluminum foil packets are a common practice in neutron scattering measurements of hydrogenated materials. These samples were then loaded into cylindrical aluminum cans with aluminum foil seals. Two samples were measured: BaH_2 (0.46 g) and CaH_2 (unknown mass). Vanadium was measured for detector normalization. Resolution functions were measured at 30 K. All measurements were performed using the Si(111) analyzers. Elastic scans were performed between 30 K to 690 K. Longer QENS measurements (approx. 3 hours) were conducted between 300 K – 690 K for higher statistics suitable for QENS data fitting.

The second BASIS experiment occurred in March 2019 using a *MICAS* furnace that was modified for pyrophoric samples, as explained in detail in Section 3.1.1. Samples were loaded into 5 mm diameter quartz NRM tubes. Vanadium, BaH_2 (0.97 g for long QENS measurements, 1.11 g for elastic scan), MgH_2 (0.42 g) samples were measured. Resolution functions were measured at 300 K. Long scans of approximately 3 hours were taken between 300 K and 920 K for BaH_2 and 300 K to 630 K for MgH_2. An elastic scan was performed for BaH_2 from 300 K to 920 K. All sample cans were evacuated in the furnace and backfilled to atmospheric pressure using helium. A 5 liter expansion volume was hooked up to the sample stick to allow the pressure to remain constant throughout the entire experiment, i.e. during heating and gas evolution.

The third and fourth BASIS experiments were conducted in November 2019 and January 2020. These were both high-pressure experiments that used the same measurement configurations and sample environments. The experiments were conducted in a single-toroidal VX5 Paris-Edinburgh (PE) press. The sample environment is described in detail in Section 3.1.2. Samples of approximately 300 mg of BaH_2 were loaded into CuBe gaskets. This was sealed in the PE cell at a pressure of approximately 5 tons. Due to the reactive nature of the sample, a pressure transmitting medium was not used. All measurements were conducted at room temperature. An elastic scan was performed during the first experiment up to a maximum pressure of approximately 5 GPa. Measurements were approximately 50 minutes for each pressure and pressure steps conducted in 5 ton steps. The second experiment were for longer QENS measurements of approximately 22 hours at each pressure up to a maximum pressure of 6 GPa. The resolution function was measured at ambient conditions. Pressures were estimated from previous diffraction experiments at SNAP, as described in Section 4.3.

A.1.2 HFBS Experiment

A QENS experiment was conducted at HFBS in December 2018. A bottom-loading CCR was used for BaH_2 and CaH_2 while a top-loading CCR was used for MgH_2. Titanium sample cans were used with gold O-ring seals (lead seal for MgH_2). Samples were loaded into aluminum foil packets in annular geometry. Sample masses were 1.5 g for BaH_2, 0.62 g for CaH_2, and 0.43 g for MgH_2. Elastic scans were performed for each sample: T = 250 K to 800 K for BaH_2, 300 K to 800 K for CaH_2, and 60 K to 525 K for MgH_2. Longer QENS measurements were taken from T = 600 K to 800 K for BaH_2, 800 K for CaH_2, and 500 K to 525 K for MgH_2. This experiment used the ± 15 μeV energy range configuration for all measurements.

An instrumental issue would not allow for measurements with ± 36 µeV energy range to be conducted reliably.

A.2 Inelastic Neutron Scattering Experimental Details

INS measurements were conducted in a series of experiments at the VISION beamline using a CCR and a stick furnace.

A.2.1 VISION Experiments

The first experiment was conducted in June 2018 using a CCR. BaH_2 and MgH_2 were measured in annular aluminum foil packets in cylindrical aluminum sample holders. However, sample environment problems were encountered regarding temperature sensors and heating capabilities, which made the data unreliable. BaH_2, CaH_2, and MgH_2 were measured at a later time in the CCR for 5 K measurements. Sample masses were approximately 0.9 g for BaH_2, 0.6 g for CaH_2, and 0.4 g for MgH_2.

The next experiment was conducted using a custom designed stick furnace that is described in Section 3.1.1. Samples were loaded into copper foil annular packets and measured inside stainless steel sample holders. The samples were empty cells, BaH_2 (1.4 g), CaH_2 (0.495 g), and MgH_2 (0.215 g). Measurements were typically around 1 hour at each temperature. Temperature ranges were 300 K to 850 K for BaH_2, 300 K to 780 K for CaH_2, and 300 K to 620 K for MgH_2. Empty cells were measured at various temperatures.

The last experiment was conducted in February 2020 with a 0.53 g BaH_2 sample in an 8mm diameter vanadium PAC can in the CCR. Measurements were performed between 5 K and 300 K for 1 hour at each temperature.

A.3 Neutron Diffraction Experimental Details

Neutron diffraction experiments were conducted at two SNS beamlines: SNAP and NOMAD. The SNAP measurements were conducted in two different experiments at high pressure with two different types gaskets. The NOMAD measurements were at low and high temperatures over the course of five different beam times.

A.3.1 SNAP Experiments

Two high pressure neutron diffraction experiments were performed at SNAP. The experiments can be divided into two main categories depending on the type of gasket used: (1) a standard encapsulated TiZr gasket (February 2019) and (2) a special split gasket made from CuBe that allows for sample loading into the toroidal chamber (November 2019). No pressure transmitting medium was used in these experiments. Sample loading was performed in a helium glove box using a specifically designed PE clamp system that surrounds the gasket-anvil assembly, as shown in Figure 7. A load of approximately 5 tons is applied to the assembly using a hydraulic press and sealed under pressure in the glovebox. The entire clamp system can then be removed and inserted into the PE press at the beamline.

A detailed description with illustrations of the TiZr encapsulated gasket design for single toroidal anvils and the PE cell assembly is presented in the reports by Marshall and Francis[34] and by Klotz et al.[35] As for the vast majority of gaskets, the sample sits in the center opening of the gasket. Encapsulation is ensured through two cups of TiZr that cover the sample at bottom and top. The powder samples are first pressed into a pellet (m = 180 mg) before being transferred inside the TiZr gaskets and sealed.

The other type of gasket is made from CuBe. For these experiments, we again adapted a specialized setup that was designed for QENS experiments by Klotz and Bove et al.[36, 37] Here we use a split gasket where the sample space is located inside the toroid to form a fully encapsulated annulus. One of the CuBe gasket halves is shown in Figure 7. However, the sample space in our experiment was increased compared to the original design by Klotz and Bove et al.[36, 37] The dimensions of our CuBe gasket is 13.2 mm outer diameter, 10.4 mm inner diameter, and a groove of 0.79 mm depth, which forms a toroidal pressure chamber volume of 81.6 mm^3 once the two parts are put together. This geometry was chosen to minimize multiple scattering effects for the high pressure QENS experiments. The PE cell assembly with the CuBe gaskets are displayed in Figure 7. The sample mass was approximately 300 mg.

SNAP is equipped with two detector banks with each bank divided into three columns. For the TiZr gasket experiments, the low-angle detector bank was centered at 65° while the high-angle detector bank was centered at 105° to optimize Q-coverage. For the experiment with the CuBe gasket, the low- and high-angle detector banks were centered at 50° and 105°, respectively. A center wavelength of 2.1 Å at standard 60 Hz were used and SNAP was operated with its guide in place. The VX3 PE cell was placed in the standard geometry into SNAP, i.e. standing upright for a beam-through-gasket geometry. To optimize the sample signal and reduce background, an incident beam collimator 3D-printed from B_4C powder was placed between the anvils. This collimator reduced the beam-size to 1.5 mm wide and 0.75 mm tall. Details of these collimators will be provided elsewhere.[100]

All measurements were conducted at room temperature. Instrument specific parameters for the refinements were determined by measuring a nickel sample in the same position and sample configuration as BaD_2. Empty sample containers and vanadium samples were also measured for data reduction and normalization. Measurements times ranged from 2 – 6 hours at each pressure for the TiZr gasket measurements and approximately 1 – 2 hours for the CuBe gasket measurements. Details about pressure determination methods can be found in Section 4.3. Data reduction was performed using *Mantid*[33] and Rietveld refinements were conducted using *GSAS-II*.[38]

A.3.2 NOMAD Experiments

The NOMAD experiments were conducted over the series of five experiments from March to November 2019. Some of the experiments ended prematurely due to unexpected facility outages and sample environment issues. BaD_2, CaD_2, and MgD_2 were measured in two different sample environments: cryostream sample shifter and a *MICAS* furnace.

The cryostream sample shifter measures higher quality (lower instrument background) data. Samples were measured in vanadium PAC cans (6 mm diameter) with a copper seal over a temperature range of 100 K to 500 K. Sample masses were 2.53 g for BaD_2, 1.09 g for CaD_2, and 1.1 g MgD_2. Empty sample holders, silicon, diamond, and vanadium were used for data normalization and generating instrument parameter files.

The MICAS furnace measurements were performed using the modified furnace and stick described in Section 3.1.1. Samples were loaded into 5mm diameter quartz NMR tubes with sample masses of 0.925 g for BaD_2, 0.56 g for CaD_2, and 0.420 g MgD_2. Measurements were performed from 300 K to 900 K for BaD_2, 300 K to 920 K for CaD_2, and 300 K to 650 K for MgD_2. Again, empty sample holders, silicon, diamond, and vanadium were used for data normalization and generating instrument parameter files. Measurements were approximately 1.5 hours at each temperature.

VITA

Eric Christopher Novak was born in Bethlehem, PA in 1992. He graduated from Southern Lehigh High School in Center Valley, PA in 2010. In 2011, he began undergraduate studies in the Physics Department at Shippensburg University in Shippensburg, PA. During the summer of 2013, he attended the Nanofabrication Manufacturing Technologies Capstone semester at Pennsylvania State University. In the summer of 2014, he completed a Research Experience for Undergraduates at the University of Arkansas in the Microelectronics-Photonics graduate program. His research project was titled *Computational Electromagnetic Modeling of Gap Enhancement in Plasmonic Nanostructures* under the supervision of Dr. Joseph Herzog. He graduated from Shippensburg University in 2015 with a Bachelor of Science degree in Physics, minor in Mathematics, and a concentration in Nanotechnology. In 2015, Eric began his Ph.D. studies in the Materials Science and Engineering Department at the University of Tennessee in Knoxville, TN. During this time, he worked as a graduate research assistant at the Research Centre of Jülich Outstation at the Spallation Neutron Source (SNS) at Oak Ridge National Laboratory in Oak Ridge, TN. His research specialized in studying metal hydride systems using neutron scattering techniques under the guidance of Dr. Niina Jalarvo and Dr. Takeshi Egami. In March 2020, he began working as a Scientific Associate at the VISION beamline at SNS, where he assumed multiple duties in assisting the user program with planning and conducting successful neutron scattering experiments at VISION.